ALMA MATER STUDIORUM
UNIVERSITA' DI BOLOGNA

Dottorato di Ricerca in:

Meccanica e scienze avanzate dell'ingegneria
IXXX Ciclo

Settore Concorsuale di afferenza: 09/A1
Settore Scientifico disciplinare: ING-IND/06

Turbulent Pipe Flow - High Resolution Measurements in CICLoPE

Tommaso Fiorini

COORDINATORE:	RELATORE:
Nicoló Cavina	Alessandro Talamelli

Esame finale anno 2017

Tommaso Fiorini 2017, **Turbulent Pipe Flow - High Resolution Measurements in CICLoPE**

Universitá di Bologna, Scuola di Ingeneria e Architettura, 47121 Forlí, Italy

Abstract

The thesis deals with the experimental investigation of turbulent pipe flow at high Reynolds number. Wall-bounded turbulence is an extremely relevant topic for engineering and natural science applications and yet many aspects of the physics are not clear. In particular at high Reynolds numbers, that are close to many real-life scenarios, the true nature of the flow is masked by the inability to properly resolve all the scales of turbulence. To overcome these difficulties the CICLoPE Laboratory was developed, the main element of which is the *Long Pipe* wind tunnel. The facility is unique in its kind, as thanks to its large scale it delivers a flow quality and resolution that can not be achieved elsewhere at these Reynolds number. Reported here are the results from the first experimental campaign performed in the facility. A first part of the results presented concerns the characterization of this new facility. Flow quality and stability are assessed, particular attention is given to the characterization of pressure drop. Single and x-wire measurements have been performed in a Reynolds number range $6500 < Re_\tau < 38000$ for a fully developed pipe flow, up to a wall normal location of $y/R = 0.3$. First, the scaling of Reynolds stresses is analysed. The magnitude of the inner peak of the streamwise normal stress shows an increasing trend up to the highest Reynolds number examined, while no outer peak was clearly distinguishable from present measurements, in disagreement with Superpipe results at similar Reynolds number. The variance profile also shows a region of logarithmic behaviour in outer scaling, as expected from the attached eddy model. Measurements of the spanwise and wall normal stresses, as well as the shear stress are also included and qualitatively confirm trends predicted by the attached eddy model. Scaling of coherent motions is investigated via spectral analysis. An inner and outer spectral peaks are identified on the (y^+, k) plane, with the former scaling in inner units while the latter neither following inner nor outer scaling, and increasing in magnitude with Re_τ. Analysis of the spectra at $y^+ \approx 15$ shows how the increase of Reynolds normal stress u^{2+} is related to the influence of large scales in the inner wall region. Quadrant analysis was carried out on streamwise and wall-normal velocity fluctuations to gain information on the Reynolds shear stress production. The results show the important role in contribution to Reynolds shear stress $\overline{uv}$ of highly intermittent and strong events like ejections, that assume an even more intermittent and dominant role with the increase of Reynolds number.

Key-words: Wall turbulence, pipe flow, high Reynolds number, hot-wire, x-wire, statistics, spectra, quadrant analysis.

Contents

Introduction

Many phenomena commonly observed in everyday life are turbulent flows: the wake behind a boat, the motion of clouds on a windy day and the smoke rising from a fire. Turbulence appears as an unstable and irregular system of differently sized eddies, constantly evolving and interacting with each other. Given particular conditions, the motion of a fluid can transition from the more regular and predictable laminar regime to the turbulent one. At first glance the process appears chaotic, so much that in-fact a reliable prediction of its behaviour may seem downright impossible. And indeed, despite undeniable progress in our understanding over the last century, turbulence remains one of the last unresolved problems of classical physics, owning to its sheer complexity. The interest in turbulence investigation is not only motivated by the desire to gain a deeper physical understanding on the nature of such a complex phenomenon; turbulence is present in an vast number of fields, such as ground transportation, energy production and climate prediction. Gaining a better understanding of the phenomenon can lead to great improvements in the efficiency of these industrial and environmental applications as well as the development of better models to simulate and predict turbulent flows. Reynolds (1883) was the first to carry out a systematic study on the onset of turbulence . In his universally famous pipe flow experiment of 1883, he studied the transition to turbulence in the water flowing inside a glass pipe, using black ink as a tracer. Increasing the water flow rate, he observed the motion transitioning from a laminar flow where the ink trace would travel parallel to the pipe walls, to a turbulent motion where ink was transported in the full pipe section. He discovered that transition to turbulence is governed by a dimensionless parameter, that after some years was given the name *Reynolds number*:

$$Re = \frac{UL}{\nu} \tag{0.1}$$

Where U and L are the flow's characteristic length and velocity scales, and ν is the kinematic viscosity of the fluid. Reynolds found out that transition to turbulence started when this dimensionless parameter reached a certain value, which is generally referred to as the *critical Reynolds number*. But Reynolds number is not only the fundamental parameter for stability, it is also used to

establish a dynamic similitude between different turbulent flow cases; in-fact it can be interpreted as a ratio between inertial and viscous forces acting on the fluid particle. While inertial forces tend to maintain and produce turbulent fluctuations, viscous forces dampen and dissipate turbulent kinetic energy into heat. The scientific interest in high Re flows stems not only from the desire to get closer to real-life applications such as the flow over an aircraft or in the atmosphere, but also from the fact that a lot of the theory we have on turbulence is valid in the infinite Reynolds number limit. Therefore studying high Re flows can lead to relevant conclusion about the nature of turbulence and its behaviour. A better understanding of the underlying principles governing turbulent flows would, in turn, favour the development of more accurate prediction and models with great benefits in a vast number of applications.

High Reynolds number wall-turbulence is characterized by the presence of a wide range of different scales, from the big eddies whose dimensions are associated with the external flow geometry to the smallest ones that are dominated by viscosity. According to the classical theory of turbulence, turbulent kinetic energy is introduced in the flow in the form of large coherent structures, or eddies, that depend on the external flow geometry and are dominated by inertial forces. From the larger eddies kinetic energy is transferred down to the smaller ones in a process that is known as *energy cascade*. This continues until eddies reach their minimum dimension, on a scale where viscosity dominates over inertial forces, and dissipation of the turbulent kinetic energy into heat takes place. These small structures are called *Kolmogorov scales*, from the name of the mathematician that first theorized them in 1941. Unlike large scale eddies, they are believed to be independent on the flow geometry and to have universal and isotropic properties. The variety of turbulent scales and their difference in dimensions grows with increasing Reynolds number. In other words the higher the Reynolds number, the smaller the dissipation scales become compared to the large ones. This phenomenon is called 'separation of scales' and is a defining characteristic of high Reynolds number turbulence.

Turbulence becomes even more complicated when the flow is confined by one or more solid surface, these introduce anisotropy and new scales of motion in an already complex problem. Turbulence is then produced in a thin layer close to the wall where velocity quickly goes to zero as an effect of the fluid viscosity. However, it must be stressed how important this small region of the flow is; because it's here that friction between the fluid and the wall develops, one of the main cause of energy loss in many applications. And friction is an essential parameter for the scaling of wall-bounded turbulence, as these kind of flows are dominated and driven by friction.

In recent years the increase in the available computing power has allowed the use of direct numerical simulations (DNS) in the study of turbulence for increasing Reynolds number, but despite this , the attainable Re remains moderate and an order of magnitude lower than what can be reached in experiments.

In fully resolved DNS the Navier-Stokes equations governing fluid motion are numerically solved up to their finest spatial and temporal scales, without the use of any model. This requires that with increasing Reynolds number, more and more grid points are needed to simulate the flow, making the simulations extremely cumbersome. Therefore at present, and for many years to come, the experimental approach remains the only option for investigating high Reynolds number turbulence. But just like simulations also this approach is affected by scale separation at high Reynolds numbers. In particular, given a fixed size experiment, as the Reynolds number is increased the smallest turbulent scales become smaller and smaller, while the large-scale eddies remain fixed by the external geometry. This can result in an insufficient spatial resolution of the instruments used to measure the smaller turbulent scales. What happens with an experimental technique such as hot-wire anemometry is called *spatial filtering* and is an artificial attenuation of small-scale turbulent fluctuations.

As expressed in the comprehensive reviews by Kim (2012), Smits *et al.* (2011*a*) and Marusic *et al.* (2010*b*); despite being studied for a long time, there are still many open questions in wall turbulence. In last decades experimental results from the Princeton Univesity/ONR Superpipe facility (see Zagarola & Smits (1998); McKeon *et al.* (2005); Hultmark *et al.* (2012)) became available at previously unprecedented Reynolds number. The data had a great impact on the scientific community and has produced a renewed interest in these flows. However, the inability to reproduce similar high Reynolds number experiments and the problem of spatial resolution has made any effort to draw definitive conclusion on the matter fruitless.

In order to overcome these difficulties and provide high quality and high Reynolds number data that the CICLoPE (Center for International Cooperation in Long Pipe Experiments) initiative was started. At the heart of the project is the construction of a new large scale wind tunnel, the Long Pipe facility. As detailed in Talamelli *et al.* (2009), the fundamental idea behind it is that instead of achieving high Reynolds through an increase of flow speed U or fluid density ρ, the approach taken is to have a large scale experiment, increasing L in expression (0.1), in order to attain simultaneously high Reynolds number and high spatial resolution. The facility specification were decided by an international group of scientist in the field of turbulence research, around the requirement of having a sufficiently high Reynolds number to observe scale separation while being able to use well-established measuring techniques without incurring in spatial resolution problems. This is possible thanks to the large scale of the facility, whose ideal installation site was found in Predappio, Italy. Two underground tunnels that were excavated during the 1930s were donated to the University of Bologna. The tunnels provide a stable, noise and vibration free environment to host the Long Pipe facility.

The need for spatial resolution in experiments has made progress in research very slow and has so far masked the true behaviour of wall-bounded

turbulence. The aim of this thesis is to use the opportunity offered by this unique facility, and measure wall-bounded turbulence in a detailed and accurate way, up to the smallest scales of the flow. In particular, the objective of the investigation is to characterize turbulent fluctuations and explore their scaling at high Reynolds numbers. The presence of velocity fluctuations in a turbulent flow has a deep impact on the dynamics of the mean flow, and a description of terms describing fluctuations are required for the problem's solution. The large scale of the facility allows to easily use multi-component measuring techniques, which is generally more difficult and cumbersome in a traditional experiment, as well as having worse spatial resolution. This allows the full characterization of an intrinsically three-dimensional problem. An additional aim is to study the flow structures and dynamics associated with those fluctuations, to gain a more complete description of the phenomenon. Fluctuations can be associated with eddies and the occurrence of particular events in the flow field, in order to study the topology and dynamics of high Reynolds number wall turbulence. The experimental campaign is carried out with traditional hot-wire sensors, that provide an established and well-known method for measuring turbulence while having a very high spatial and temporal resolution.

The thesis is structured as follows: the first chapter defines the mathematical tools and symbols used, gives a theoretical basis for wall-bounded turbulence in general and pipe flow (which is the object of investigation here) in particular, and finally gives a quick review of the historically more relevant investigations and their results, outlining the 'open questions' in the framework of the thesis' objectives. In chapter 2 the motivations for the CICLoPE Laboratory are expressed, and a detailed description of the Long Pipe facility as well as the experimental set-up used is given. Chapter 3 deals with the results concerning the general characterization of the facility and its flow-quality. Chapters 4 deals with the statistical characterization of turbulent fluctuations, while chapter 5 analyses the coherent structures and events in the flow. In chapter 6 the main conclusions of the investigation are summarized.

CHAPTER 1

Theoretical Background

In this chapter, the mathematical instruments and definitions used throughout the thesis will be given, along with some theoretical basis on wall-bounded turbulent flows. A brief review of the active fields of research in wall-turbulence will be given, as well as a summary of relevant experiments at high Reynolds number. Finally a detailed description of the thesis objectives is outlined.

1.1. Statistical tools for turbulence

In order to study such a chaotic process as turbulence, a statistical approach is taken, as the complexity of the phenomenon makes it suitable to be described as a purely random process. In this section a brief explanation of the statistical notions used later in the thesis will be provided.

1.1.1. *The probability density function*

The *probability density function* (PDF), of a random variable $U(t)$ is a function that describes the relative likelihood for this random variable to assume a certain value. If the PDF of a random variable is known, then all the statistical moments of any order are known. We first introduce the *cumulative distribution function* (CDF) of a random variable $U(t)$, $F_U(k)$. It is defined as the probability that $U(t)$ has to take on a value that is smaller or equal to k:

$$F_U(k) = P(U(t) \leq k) \tag{1.1}$$

Every cumulative distribution function is a monotone non-decreasing function. Given the definition it follows that, for every $U(t)$, $F_U(-\infty) = 0$ and $F_U(+\infty) = 1$. The probability that the random variable assumes a value that is between two values U_1 and U_2, with $U_1 \leq U_2$ can be expressed with cumulative distribution functions:

$$P(U_1 \leq U(t) \leq U_2) = F_U(U_2) - F_U(U_1) \tag{1.2}$$

The probability density function $f(U)$ is then defined as:

$$f(U) \equiv \lim_{\Delta U \to 0} \left(\frac{F_U(U + \Delta U) - F_U(U)}{\Delta U} \right) \tag{1.3}$$

or, in other words:

$$f(U) = \frac{dF_U(U)}{dU} \tag{1.4}$$

and has the following properties:

$$f(U) \geq 0, \tag{1.5}$$

$$\int_{-\infty}^{+\infty} f(U)dU = 1, \tag{1.6}$$

$$F_u(U) = \int_{-\infty}^{U} f(\chi)d\chi \tag{1.7}$$

1.1.2. *Statistical moments*

The *mean* is the first order statistical moment:

$$<U>= \int_{-\infty}^{+\infty} U f(U)dU \tag{1.8}$$

from the mean, the *fluctuations* can be defined:

$$u \equiv U - <U> \tag{1.9}$$

Since the mean value of fluctuations is always null, to further describe the statistics of the process, higher order moments are introduced. The second order moment is the *variance*:

$$<u^2>= \int_{-\infty}^{+\infty} u^2 f(U)dU \tag{1.10}$$

The square root of the variance is known as the *standard deviation* or *root mean square*, that gives a measure of the typical fluctuations' magnitude:

$$\sigma_u = \sqrt{<u^2>} \tag{1.11}$$

likewise, other statistical moments can be introduced; the nth centred statistical moment of the random variable $u(t)$ is defined as:

$$<u^n>= \int_{-\infty}^{+\infty} u^n f(U)dU \tag{1.12}$$

of particular interest to turbulence study, are the third and fourth order moments, the *skewness* and *flatness*. They are usually normalized with the root mean square of appropriate order, giving the skewness and flatness factors:

$$S_u = \frac{<u^3>}{\sigma_u^3} \tag{1.13}$$

$$F_u = \frac{<u^4>}{\sigma_u^4} \tag{1.14}$$

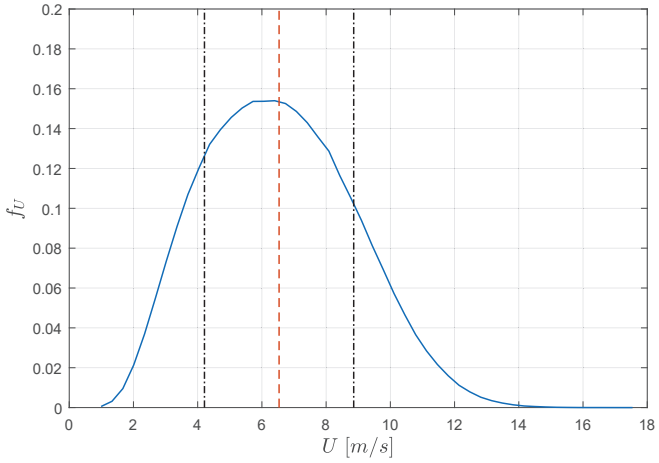

Figure 1.1: Example of PDF uf velocity signal $U(x,t)$ from current measurements. $--$; mean value of the velocity $\overline{U}$. $\cdot-$; $\overline{U} \pm \sqrt{\overline{u^2}}$.

The skewness and flatness factors are used to describe particular properties of the probability density function. The skewness is a measure of the symmetry of the PDF, and is equal to zero when the distribution is symmetrical (see figure 1.1). The flatness on the other hand indicates the relative flatness or peakedness of the distribution function. A gaussian distribution has $S_u = 0$ and $F_u = 3$.

1.1.3. *Velocity averaging in turbulent flows*

In turbulence study, the instantaneous velocity components, U_i are usually divided into their mean and fluctuating part, in what is known as *Reynolds decomposition*.

$$U_i = <U_i> + u_i \tag{1.15}$$

where U_i is the ith component of the instantaneous velocity vector $\mathbf{U}$, in general a function of time t and position $\mathbf{x} = (x, y, z)$, $<U_i>$ is its mean part and u_i is its fluctuating part. The rigorous way to obtain the averaged value would

be with an *ensemble average*. Let's suppose we can conduct the same exact experiment n times, each time measuring the velocity in the point $\mathbf{x}$ at the time t, with $U_{i,j}(\mathbf{x},t)$ being the jth realization of the experiment. Then the velocity ensemble average in the point $\mathbf{x}$ and at the time t is given by:

$$<U_i>(\mathbf{x},t) \equiv \frac{\sum_{j=1}^{n} U_{i,j}(\mathbf{x},t)}{n} \tag{1.16}$$

Where $U_{i,j}(\vec{x},t)$ denotes the ith component of velocity measured in the jth experiment, at time t and in the position $\vec{x}$. However, this is not how averages are taken in experimental fluid dynamics. The assumption that is usualy made is that the flows studied are *statistically stationary*. This means that their statistical properties are not dependent on the time t, and have the same value averaged over time as averaged over different experiments. So the mean part of velocity, for a turbulent but statistically stationary flow is defined as a temporal mean $\overline{U_i}$:

$$<U_i>(\mathbf{x}) = \overline{U_i}(\mathbf{x}) \equiv \frac{1}{T}\int_0^T U_i(\mathbf{x},t)dt \tag{1.17}$$

When a process satisfies this relationship is said to be *ergodic*. All the mean values that will be used when carrying out the experimental part, will be taken averaging over time.

1.1.4. *Correlation*

When the random variable is a function of time, the phenomenon is called *random process* and will be indicated as $U(t)$. Even if the PDF is known in a certain place in the flow field, this does not give any informations about existing statistical relations between two different points in the flow; indeed very different statistical processes might have the same PDF. For this purpose multi-time and multi-space statistical properties are used. The *auto-covariance* at the point $\mathbf{x}$ is defined as:

$$R(\mathbf{x},\tau) \equiv <u(\mathbf{x},t)u(\mathbf{x},t+\tau)> \tag{1.18}$$

Where τ is called *lag time*. If the process is statistically stationary, the auto covariance does not depend on t but only on τ. Auto-covariance gives an idea of the time that it takes for the process (the turbulent flow in our case) to "forget" its past history at a particular point. From the auto-covariance the *correlation function* can be defined:

$$\rho(\mathbf{x},\tau) \equiv \frac{<u(\mathbf{x},t)u(\mathbf{x},t+\tau)>}{<u(\mathbf{x},t)^2>} \tag{1.19}$$

it has the following properties:

$$\rho(0) = 1, \tag{1.20}$$

$$|\rho(\tau)| \leq 1 \tag{1.21}$$

In figure 1.2 is shown an example of autocorrelation function for the streamwise velocity, $\rho_{uu}(\tau)$ plotted against the lag time τ.

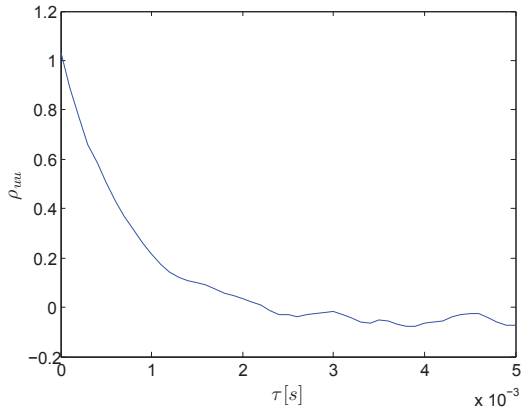

Figure 1.2: Example of autocorrelation function of streamwise component of velocity obtained from current measurements, as a function of the lag time τ.

As can be seen, the correlation diminishes rapidly as τ increases. When its value reach zero it means that the fluctuations at time $t + \tau$ are no longer correlated to the ones at time t. A time scale called *integral time scale* can be defined:

$$\Lambda_t \equiv \int_0^\infty \rho(\tau) d\tau \tag{1.22}$$

The same considerations on correlation can be made using space instead of time as the parameter. Covariance can be defined using fluctuations from different points in space but at the same time, instead of the same point but different times. If this is the case the *covariance* becomes a multi-space and single-time statistical property:

$$R_u(\mathbf{x}, \mathbf{r}) \equiv <u(\mathbf{x}, t)u(\mathbf{x} + \mathbf{r}, t)> \tag{1.23}$$

from this, in the same manner as before, the *spatial correlation function* is defined:

$$\rho_u \equiv \frac{<u(\mathbf{x},t)u(\mathbf{x}+\mathbf{r},t)>}{<u(\mathbf{x},t)^2>} \tag{1.24}$$

$\mathbf{r}$ is the distance vector between the point $\mathbf{x}$ and the other point where fluctuations are taken. If the process is statistically stationary, both the covariance and the spatial correlation function are independent on the time t. Spatial correlation functions can be calculated in a multitude of different ways, for example considering the spatial correlation of a velocity component u_i with itself (which is called *spatial autocorrelation*) or two different velocity components, which is reffered to as *cross-correlation*. The autocorrelation can be *longitudinal* if $\mathbf{r}$ is parallel to u_i or *transverse* if it is perpendicular. Just like the temporal correlation an integral scale can be defined. The *integral length scale* is:

$$\Lambda_l \equiv \int_0^\infty \rho_u(r)dr \tag{1.25}$$

As can be seen in 1.25, integration should be applied over an infinite domain. That's obviously not possible, both in the experimental and in the numerical field. To overcome this problem the spatial correlation function is usually integrated up to its first zero value or, if there is one, to its minimum negative value.

1.1.5. *Taylor's hypotesis*

Although temporal and spatial correlations of a variable are both theoretically and experimentally two distinct things (the first can be carried out with single point measurements, while the second requires multiple points), it can be asked if there is a connection between the two, or if when we obtain one of this correlations, we can infer anything on the other. In most circumstances, it is much simpler to perform measurements at a single point and different times rather than simultaneously at several points. Taylor (1938) proposed a simple hypothesis where time and space behaviours (along the mean direction of motion) of a fluid-mechanics variable k are simply related by the convection velocity U_c on the mean velocity direction x_1.

$$\frac{\partial k}{\partial t} \approx -U_c \frac{\partial k}{\partial x_1} \tag{1.26}$$

in other words, the diffusion of the quantity k and its transport in directions orthogonal to the mean flow are ignored. This seems like a very coarse approximation but experimental studies have confirmed that it works fairly well in most conditions, one crucial parameter is the value of the convection velocity U_c. The hypothesis is also known as *frozen turbulence* because, in Taylor's original formulation $U_c = \overline{U}$ for every scales, meaning that the flow structures are supposed 'frozen' and only convected by the mean local velocity field. When

measuring spectral functions, Taylor's hypothesis allows the replacement of the frequency along the mean flow direction with the wavenumber. Experiments have demonstrated that this simplified approach is not always effective and in order to apply the hypothesis with a good degree of approximation, convection velocities different than the mean velocity have to be used; Romano (1995) and Del Álamo & Jiménez (2009) proved it in wall turbulence, where for a correct estimate a lower convection velocity than the local mean has to be used, when in proximity of the wall. It is generally believed that while large scales are convected by the mean flow velocity, small scales are convected with a much lower velocity which depends on the Reynolds number and the particular flow considered.

1.1.6. *Power spectral density*

The complete description of a random process cant be deduced solely from its PDF. While correlations give additional information on the time and space evolution of the process, the spectra describes how the energy of the random process is distributed among frequencies. By providing a description of turbulence in the frequency domain, it is possible to see how the energy of turbulent fluctuations is distributed among different frequency and, using Taylor's hypothesis, scales. In order to do so, the Fourier transform $\mathcal{F}$ can be used. The Fourier transform converts a mathematical function of time, $f(t)$ into a new function, denoted by $\mathcal{F}(\omega)$ whose argument is angular frequency ($\omega = 2\pi f$). $f(t)$ and $\mathcal{F}(\omega)$ are also respectively known as time domain and frequency domain representations of the same 'event'.

$$\mathcal{F}(\omega) \equiv \frac{1}{2\pi} \int_{-\infty}^{+\infty} e^{-i\omega t} f(t) dt \tag{1.27}$$

For continued signals, the typical signal for experimental measurements, it makes more sense to define a *power spectral density* (PSD), which describes how the power of a signal or time series is distributed over the different frequencies. The power P of a signal $u(t)$ can be defined as:

$$P = \lim_{T \to \infty} \frac{1}{T} \int_{0}^{+\infty} u(t) dt \tag{1.28}$$

for many signals of interest this Fourier transform does not exist. Because of this, it is advantageous to work with a *truncated Fourier transform* $\mathcal{F}_T(\omega)$, where the signal is integrated only over a finite interval:

$$\mathcal{F}_T(\omega) = \frac{1}{\sqrt{T}} \int_{0}^{+\infty} u(t) e^{-i\omega t} dt \tag{1.29}$$

The power spectral density can then be defined:

$$S_{uu}(\omega) = \lim_{T\to\infty} <\mathcal{F}_T(\omega)> \tag{1.30}$$

One extremely important attribute of the PSD is that for a statistically stationary process, it constitutes a Fourier transform pair with the auto-covariance function $R(\tau)$:

$$S_{uu}(\omega) = \frac{1}{2\pi}\int_{-\infty}^{+\infty} e^{-i\omega\tau} R(\tau) d\tau \tag{1.31}$$

The *inverse transform* is:

$$R(\tau) = \int_{-\infty}^{+\infty} e^{i\omega\tau} S_{uu}(\omega) d\omega \tag{1.32}$$

for $\tau = 0$, (1.32) becomes:

$$\overline{u^2} = \int_{-\infty}^{+\infty} S_{uu}(\omega) d\omega \tag{1.33}$$

So $S_{uu}(\omega)$ can be interpreted as the variance (or turbulent energy) present in the band of length $d\omega$ centered at ω. It is important to note that the power spectral density is an even function i.e. $S_{uu}(\omega) = S_{uu}(-\omega)$ but for our application we will only deal with positive frequencies, hence we will use the following expedient:

$$P_{uu}(\omega) = 2S_{uu}(\omega) \tag{1.34}$$

if ω is positive, otherwise $P_{uu}(\omega) = 0$. Usually the frequency f is used instead of the angular frequency ω when representing PSD in frequency domain.

1.1.7. *Spectral density estimation*

When carrying out spectral analysis on experimental data, we want to estimate the spectral density of a random signal $u(t)$ from a finite sequence of time samples. The most obvious way to proceed would be to apply a discrete Fourier transform (DFT) to the entire data set, also known as the periodogram method. This however introduces many problems: first the spectral bias that is caused by the abrupt truncation of the data, a finite data set can in fact be seen as a signal multiplied by a rectangular window function. Furthermore this method would give a very scattered and noisy result. In order to reduce this effect, a window function that provides a more gradual truncation of the data set is needed. The side effect is that when using a window, a loss factor is introduced because part of the data is artificially damped. Then in order to reduce the random error and obtain a converging spectral density with sampling time, the signal can be divided in multiple segment where the DFT is computed separately, then the results are averaged. This method gives a

smoother and more accurate PSD estimation at the expense of a reduced frequency range; the lower frequency corresponds to the length of each individual window. For current measurements, the method proposed by Welch (1967) was used. This method has the advantage of obtaining a smoother PSD estimate by computing the DFT for different data segments and then averaging them, but it also reduces the loss of information related to windowing by overlapping these segments. The method can be summarized in these steps:

- the sampled data $u(t)$ of n points is divided into N segments of length D, overlapping each other by a number of points equal to $D/2$ (50% overlap in this case)
- The individual N data segments have a window $w(t)$ applied to them (a simple Hanning window in this case) in the time domain to reduce bias.
- DFT is calculated for $u(t)w(t)$ separately for every segment, then the square magnitude is computed, obtaining N spectral estimates.
- Averaging is applied across the N PSD estimates to obtain the final result.

Using this method, the PSD estimate $P_{uu}(f)$ is obtained. When performing spectral analysis, sometimes the wavenumber spectrum is used instead of the frequency. To convert from one to the other, Taylor's hypothesis is used:

$$k = \frac{2\pi f}{\overline{U}} \tag{1.35}$$

where $\overline{U}$ is the local mean velocity. The wavenumber spectrum $\Phi_{uu}(k)$ can then be obtain from $P_{uu}(f)$ with:

$$\Phi_{uu}(k) = \frac{P_{uu}(f)\,\overline{U}}{2\pi} \tag{1.36}$$

so that by integrating the wavenumber spectrum over all wavenumbers, the variance of the signal is obtained:

$$\overline{u^2} = \int_0^\infty \Phi_{uu}\, dk \tag{1.37}$$

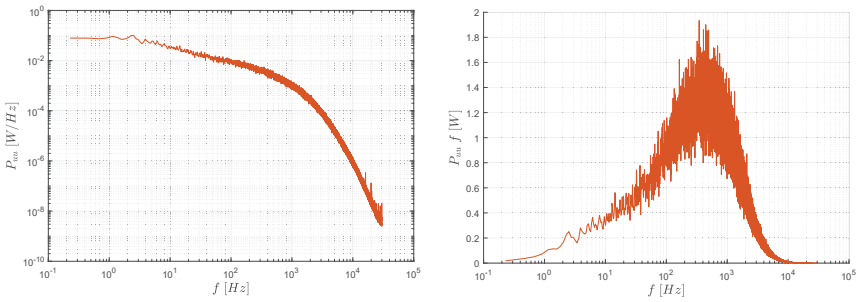

Figure 1.3: Power spectral density P_{uu} from current measurements. On the left in double logarithmic scaling and on the right in pre-multiplied form. Velocity was acquired at $y^+ = 10$ and $Re_\tau = 2.2 \times 10^3$.

1.2. Pipe flow equations

To describe a pipe flow we can start from the Navier-Stokes equations for an incompressible fluid, written in Eulerian form and neglecting body forces:

$$\frac{\partial \mathbf{U}}{\partial t} + (\mathbf{U} \cdot \nabla)\mathbf{U} = -\frac{1}{\rho}\nabla p + \nu \nabla^2 \mathbf{U} \tag{1.38}$$

$$\nabla \cdot \mathbf{U} = 0 \tag{1.39}$$

Equation (1.38) is the momentum balance, while (1.39) is the conservation of mass (or continuity) equation. $\mathbf{U} = (U, V, W)$ is the velocity vector, p is the pressure, $\rho = const$ is the fluid density and $\nu = \mu/\rho$ is the kinematic viscosity. Considering the fact that we are dealing with a turbulent flow, and the velocity $\mathbf{U}(\mathbf{x}, t)$ can be related to a random variable, we use the Reynolds's decomposition technique to divide the random quantities into their mean and fluctuations about the mean:

$$U(\mathbf{x}, t) = \overline{U}(\mathbf{x}, t) + u(\mathbf{x}, t) \tag{1.40}$$

Where the over-bar indicates averaged quantities and lower case letters indicate fluctuations. Applying the Reynolds decomposition to the Navier-Stokes equations, the so-called Reynolds averaged Navier-Stokes equations (RANS) can be obtained. The equations can be specialized for the case of a circular pipe. Given the axial-symmetry of the problem, it is convenient to define a cylindrical coordinate system (x, r, θ). The axial coordinate is denoted by x, the radial coordinate by r, originating from the pipe centreline and normal to the wall; and the angular coordinate is θ. The components of the velocity vector $\mathbf{U}$ in the coordinate system are (U, V, W), respectively the streamwise,

wall-normal and spanwise components. In the Reynolds decomposition, the mean part is $(\overline{U}, \overline{V}, \overline{W})$, and the fluctuating part is (u, v, w). R is the pipe radius. A turbulent pipe flow is statistically axial-symmetric, so that:

$$\overline{W} = \overline{uw} = \overline{vw} = \frac{\partial}{\partial \theta} = 0 \tag{1.41}$$

Considering 1.41, and substituting into the RANS equations, the continuity equation and momentum balance in the x and r directions become:

$$\frac{\partial \overline{U}}{\partial x} + \frac{1}{r}\frac{\partial}{\partial r}(r\overline{V}) = 0 \tag{1.42}$$

$$\frac{\partial \overline{U}}{\partial t} + \overline{U}\frac{\partial \overline{U}}{\partial x} + \overline{V}\frac{\partial \overline{U}}{\partial r} = -\frac{1}{\rho}\frac{\bar{p}}{\partial x} - \frac{\partial}{\partial x}\overline{u^2} - \frac{1}{r}\frac{\partial}{\partial r}(r\ \overline{uv}) + \nu\nabla^2\overline{U} \tag{1.43}$$

$$\frac{\partial \overline{V}}{\partial t} + \overline{U}\frac{\partial \overline{V}}{\partial x} + \overline{V}\frac{\partial \overline{V}}{\partial r} = -\frac{1}{\rho}\frac{\bar{p}}{\partial r} - \frac{\partial}{\partial x}\overline{uv} - \frac{1}{r}\frac{\partial}{\partial r}(r\ \overline{v^2}) + \frac{\overline{w^2}}{r} + \nu\left(\nabla^2\overline{V} - \frac{\overline{V}}{r^2}\right) \tag{1.44}$$

Adding the addition hypothesis that the flow is statistically stationary and we consider a fully developed flow (not any more dependent on the axial coordinate x), we get the additional relations:

$$\frac{\partial}{\partial t} = 0 \tag{1.45}$$

$$\frac{\partial \overline{U}}{\partial x} = \frac{\partial \overline{u^2}}{\partial x} = \frac{\partial \overline{v^2}}{\partial x} = 0 \tag{1.46}$$

Taking into account that for the no-slip condition and axial-symmetry, $\overline{V}|_{r=R} = \overline{V}|_{r=0} = 0$, and considering the continuity equation (1.42), we get that the mean wall-normal velocity must be zero over all the profile:

$$\overline{V} = 0 \tag{1.47}$$

Substituting (1.45),(1.46) and (1.47) in the r component of the momentum equation we obtain:

$$\frac{1}{\rho}\frac{\bar{p}}{\partial r} + \frac{\partial \overline{v^2}}{\partial r} = \frac{\overline{w^2}}{r} - \frac{\overline{v^2}}{r} \tag{1.48}$$

integrating (1.48) between a generic radial coordinate r and R we obtain:

$$\frac{1}{\rho}(\overline{p_w} - \bar{p}) - \overline{v^2} = \int_r^R \left(\frac{\overline{w^2}}{r} - \frac{\overline{v^2}}{r}\right)\ dr \tag{1.49}$$

where the subscript "w" indicates the wall, at $r = R$. Taking the x derivative of (1.49) and using the hypothesis of fully developed flow (1.46), we obtain the following result:

$$\frac{\partial \overline{p}}{\partial x} = \frac{\partial \overline{p_w}}{\partial x} \tag{1.50}$$

This states that the axial pressure gradient is uniform on the pipe radius. Substituting (1.45),(1.46), (1.47) and (1.50) in the x component of the momentum equation we obtain:

$$\frac{1}{\rho}\frac{d\overline{p_w}}{dx} = -\frac{1}{r}\frac{d}{dr}(r\ \overline{uv}) + \frac{\nu}{r}\frac{d}{dr}\left(r\frac{d\overline{U}}{dr}\right) \tag{1.51}$$

adding the definition of total shear stress $\tau(r)$ as:

$$\tau = \mu\frac{d\overline{U}}{dr} - \rho\overline{uv} \tag{1.52}$$

equation (1.51) can be re-written as:

$$\frac{d\overline{p_w}}{dx} = \frac{1}{r}\frac{d(r\tau)}{dr} \tag{1.53}$$

which can the be integrated from 0 to R:

$$\tau_w = \frac{R}{2}\frac{d\overline{p_w}}{dx} \tag{1.54}$$

(1.54) is the relation that analytically links the axial pressure gradient at the wall with the wall friction τ_w, and from a practical point of view is extremely important in experimental investigation of pipe flows. If we integrate up to a generic r instead of R, and we add the variable $y = R - r$ (wall-normal distance), we get the general relation:

$$\tau(y) = \tau_w\left(1 - \frac{y}{R}\right) \tag{1.55}$$

which corresponds to a linear relationship, decreasing from the wall where $\tau = \tau_w$, to the centerline where $\tau = 0$.

1.3. Wall bounded turbulence scaling

Classically turbulence can divided into *free-shear flows* such as jets or wakes and *wall-bounded flows* as the channel, boundary layer or pipe flow. While in free shear flows, turbulence arises from a difference between velocities in the flow field, in wall turbulence the presence of a solid surface, the viscosity of the fluid and the resulting no-slip condition (velocity of the fluid at the

wall is zero) triggers the onset of turbulence. This thesis focuses on wall-bounded turbulence and in particular on pipe flow. The presence of the wall introduces unique features and turbulent scales that need to be elaborated upon. The following considerations are valid for wall-bounded turbulent flows in general; for a more in-depth background the reader is directed to Pope (2001). According to the classical analysis, wall bounded turbulent flows can be divided into two regions: an *inner region* close to the wall, and an *outer region* far away from it. The assumption made is that in the inner region of the flow viscosity plays an major role, while the external geometry does not influence the flow behaviour; according to this hypothesis all turbulent flows should display a similar near-wall behaviour even if their external conditions are different. The inner region is where the dynamics of the flow are heavily influenced by viscosity. The variables affecting the mean velocity $\overline{U}$ are the wall friction τ_w, the wall-normal distance y, and the fluid kinematic viscosity ν. Therefore we define characteristic velocity scale in this region as the *friction velocity* u_τ:

$$u_\tau = \sqrt{\frac{\tau_w}{\rho}} \tag{1.56}$$

where ρ is the fluid density; and the characteristic length scale is the viscous length l_*.

$$l_* = \frac{\nu}{u_\tau} \tag{1.57}$$

And from these a *viscous time-scale* can be defined as well:

$$t_* = \frac{l_*}{u_\tau} = \frac{\nu}{u_\tau^2} \tag{1.58}$$

A characteristic Reynolds number can also be defined for wall flows, as the *friction Reynolds number* which, in the case of a pipe flow, is equal to the pipe radius normalized in inner variables:

$$Re_\tau = \frac{Ru_\tau}{\nu} = \frac{R}{l_*} = R^+ \tag{1.59}$$

From dimensional analysis, in the inner region:

$$\frac{\overline{U}}{u_\tau} = f\left(\frac{yu_\tau}{\nu}\right) = f\left(\frac{y}{l_*}\right) \tag{1.60}$$

If we define U^+ and y^+ as the mean velocity and the wall-normal distance normalized with the inner variables u_τ and l_*, equation 1.60 can be re-written as:

$$U^+ = f(y^+) \tag{1.61}$$

Equation (1.61) is also known as *Prandtl's law of the wall* and is attributed to Prandtl (1926). On the contrary, when we consider the mean velocity behaviour in the outer region of the flow (also called *core region* for internal flows, such as the pipe) the viscosity no longer plays an important role. The relevant length-scale becomes the one that defines the external flow geometry, depending on the particular type of flow; the channel half-height h, the boundary layer thickness δ or the pipe diameter R. The external velocity-scale is still the friction velocity u_τ, while U_{cl} is the centreline velocity. If we apply a dimensional analysis to the outer region and consider a pipe flow with radius R, we obtain:

$$\frac{U_{cl} - \overline{U}}{u_\tau} = g\left(\frac{y}{R}\right) \tag{1.62}$$

Expression 1.62 is known as *von Kármán velocity defect law* and was derived by von Kármán (1930). The distinction between inner and outer region is not assumed to be abrupt but there must be a region where both hold simultaneously; in other words in some conditions there can be a region of space where $l_* << y << R$. Since $l_* = \nu/u_\tau$, this is true when u_τ is big or when the friction Reynolds number Re_τ is big. The region where both (1.61) and (1.62) hold, is called *overlap region*, and there:

$$f\left(\frac{yu_\tau}{\nu}\right) = g\left(\frac{y}{R}\right) \tag{1.63}$$

Following the derivation from Millikan (1938), and deriving 1.63 we obtain:

$$\frac{\partial}{\partial y}\left(\frac{\overline{U}}{u_\tau}\right) = \frac{u_\tau}{\nu} f'\left(\frac{yu_\tau}{\nu}\right) = -\frac{1}{R} g'\left(\frac{y}{R}\right) \tag{1.64}$$

The only solution for 1.64 is when f' and g' are inversely proportional to y^+ and y/R, respectively. Integrating we obtain:

$$U^+ = \frac{1}{\kappa} ln\left(y^+\right) + B \tag{1.65}$$

$$\frac{U_{cl} - \overline{U}}{u_\tau} = -\frac{1}{\kappa} ln\left(\frac{y}{R}\right) + C \tag{1.66}$$

Where κ and B are called the von Kármán constant and additive constant. According to classical theory are universal for every wall bounded flow. Equation (1.65) is known as *logarithmic law of the wall*, or simply *log law* and was first derived with a different argument by Prandtl, using the concept of mixing length but reaching the same conclusion.

1.4. Turbulent scales and energy cascade

As already discussed in the introduction, one of the peculiarity of turbulent flows is the existence of a wide range of different scale eddies. The most obvious big scales are the ones associated to the macroscopic geometric features of the flow: for a boundary layer it is the boundary layer thickness δ, for a channel it is the half-height $h/2$ and for a pipe flow it is the radius R. The idea of an energy cascade was put forward by Richardson (1922); essentially it states that turbulent kinetic energy is introduced in the flow at big scales via a production mechanism, then it is transferred in a inviscid way to scales gradually smaller until it is dissipated into heat at small scales by viscous forces. It appears evident that the dissipation rate ϵ at small scales must then be equal to the rate at which energy is produced at large scales. According to Richardson, eddies can be characterized by a length l, a velocity $u(l)$ and a time scale $\tau(l) = l/u(l)$. The big eddies have a length l_0 comparable with L, a characteristic velocity u_0 that is of the order of the root mean square of the turbulence intensity comparable with U, hence the big eddies' Reynolds number $l_0 u_0(l)/\nu$ is large and viscous effects are negligible. Later, Kolmogorov (1941) theorized the smaller dissipative scales (which are now known with his name). He observed that as l decreased, $u(l)$ and $\tau(l)$ decreased as well. He formulated a theory which can be summarized in three hypothesis:

- At sufficiently high Reynolds number, small-scale ($l << l_0$) turbulence is statistically isotropic.

This hypothesis is also known as *local isotropy*. In other words, while large eddies are anisotropic (their statistics depend on the direction considered), for small scales, turbulent flows "forget" the information given by the mean flow field and the flow's boundary conditions. Furthermore, these statistics become universal:

- At sufficiently high Reynolds number, statistics at small scale have an universal form determined by ν and ϵ.

where ϵ is the mean dissipation rate of energy. This is due to the fact that at small scales dissipation of energy transferred from bigger scales takes place via viscous processes. The mean rate at which energy is dissipated is ϵ, while ν is the kinematic viscosity. Based on these two parameters the characteristic length, velocity and time scales of the dissipation range can be defined:

$$\eta \equiv (\nu^3/\epsilon)^{1/4} \tag{1.67}$$

$$u_\eta \equiv (\epsilon\, \nu)^{1/4} \tag{1.68}$$

$$\tau_\eta \equiv (\nu/\epsilon)^{1/2} \tag{1.69}$$

η is the Kolmogorov scale. Kolmogorov also derived the ratio between the large eddie size and the dissipative eddie size (based on the relation $\epsilon \approx u_0^3/l_0$):

$$l_0/\eta \approx Re^{3/4} \tag{1.70}$$

which means that with increasing Reynolds number, the range of scales between l_0 and η increases as well. Ultimately, at very high Reynolds number there must be a range of scales of length l that are very small compared to l_0 but still very big when compared with the Kolmogorov scale. This expresses in mathematical terms what is known as *scale separation* in high Reynolds number turbulence, as the Reynolds number increases the difference in physical dimensions between big scales and dissipative scales increases almost linearly. Of course, for a fixed external geometry (as would happen in a laboratory experiment), this means that η becomes smaller and smaller. The third and final result from Kolmogorov's theory can be summarized as follows:

- At sufficiently high Reynolds number, statistics for scales l, with $\eta << l << l_0$, have a universal form determined solely by ϵ and independent on ν.

this range of scales is called *inertial sub-range* and it is only marginally affected by viscosity, it depends almost exclusively on the energy transfer rate $\mathcal{T}_e \approx \epsilon$. Hence its statistics are only defined by the dissipation rate. In figure 1.4 is shown a scheme of the different scales and the energy cascade process.

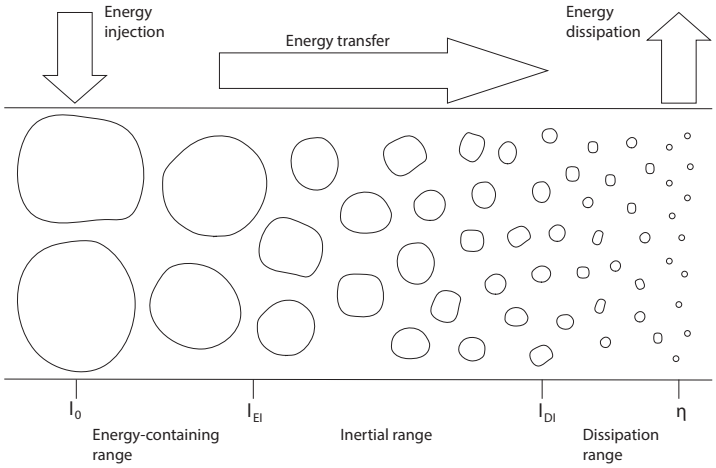

Figure 1.4: Energy cascade schematics

1.5. Hot-wire anemometry

Hot-wire anemometry (HWA) remains, many years after its first introduction by King (1914), one of the most used techniques for velocity measurements in the field of turbulent research. The main reason for its continuing success, is that it offers outstanding performance in terms of spatial and temporal resolution at a fraction of the cost of optical measurements techniques. The disadvantages in this case are the intrusive nature of the measurement, and the fact that a simple single wire sensor is limited to a point measurement of one velocity component. The basic principle of hot-wire anemometry is that the heated wire will experience a cooling effect by the flow. This effect is mainly associated to forced convection heat losses which are strongly velocity dependant. If this heat loss can be quantified, then, by means of an accurate calibration, it is possible to retrieve the flow velocity based on the wire's cooling rate. The fundamental difference with pressure-based systems like a Pitot or Prandtl tube is that the cooling effect is extremely fast due to the very small size of the sensing element, and this translates into a very high frequency response. In actual operation hot-wires nowadays are operated in constant temperature mode (CTA) which means that the anemometer keeps the wire at constant temperature and measures the electrical current needed to achieve this. This section will provide a general overview of hot-wire anemometry and its main aspects. For a more in-depth review the reader is referred to the literature on the subject, which is extremely vast and comprehensive, including Bruun (1995) or more recently Tropea *et al.* (2007).

1.5.1. *Governing equations*

An analysis on heat generation and transfer in a hot-wire will follow. In the most general case of an unsteady wire temperature T_w the following relation can be written:

$$m_w c_w \frac{dT_w}{dt} = W - Q \tag{1.71}$$

The left hand term represents the change in heat energy stored in the wire, where T_w is the wire's temperature, m_w is its mass and c_w is the specific heat of the wire's material. On the right hand side of the equation, W is the thermal power received and Q is the one lost by the wire. In hot-wire anemometry, the heating is achieved with Joule effect: a current I_w is passed through the wire with resistance R_w:

$$W = I_w^2 R_w \tag{1.72}$$

On the other hand, neglecting for the moment other forms of heat losses, the heat lost per second due to forced convection (which in most flow cases is by far the dominant one) is given by:

$$Q = (T_w - T_a) A h(U) \tag{1.73}$$

where T_a is the temperature of the fluid that is in contact with the wire, A is the surface area over which forced convection takes place, and h is the forced convection heat transfer coefficient which is dependant, amongst other things, on the fluid velocity U. If the stationary case is considered ($T_w \approx const$), as is the case for CTA operation (1.71) becomes:

$$I_w^2 R_w = (T_w - T_a) A h(U) \tag{1.74}$$

For a metal R_w can be expressed a function of T_w, using a linear approximation around a certain reference temperature T_0:

$$R_w = R_0[1 + \alpha_0(T_w - T_0)] \tag{1.75}$$

where R_0 is the wire resistance evaluated at temperature T_0 and α_0 is the resistivity coefficient of the wire material at the same temperature. For metals this value is positive, meaning that resistance increases with increasing temperature. If we take the fluid ambient temperature as our reference temperature, it's possible to derive the following expression:

$$T_w - T_a = \frac{R_w - R_a}{\alpha_a R_a} \tag{1.76}$$

In the case of a cylinder-shaped body, the forced convection coefficient h can be expressed as:

$$h = \frac{Nu\, k_f}{d_w} \tag{1.77}$$

where k_f is the thermal conductivity of the fluid, and d_w is the cilinder's diameter. Nu is the Nusselt's number, which if we consider a subsonic flow and that natural convection is negligible with respect to forced convection:

$$Nu = Nu\left(Re_w, \frac{T_w - T_a}{T_a}\right) \tag{1.78}$$

Where Re_w is the wire's Reynolds number which uses the wire diameter d_w; from now on it will be referred as Re_w to avoid confusion. Usually $2 < Re_w < 40$ for hot-wires measurements, well before the onset of vortex shedding. A correlation expressions for the Nusselt number can be used, in the form:

$$Nu = A_1 + B_1 Re_w^n \tag{1.79}$$

Where A, B and n (which is usually taken 0.5) are characteristic constants of the particular correlation function. Considering a specific wire diameter, Re_w becomes a function of only the velocity U, and the (1.79) can be rewritten as:

$$Nu = A_2 + B_2 U^n \tag{1.80}$$

Combining equations (1.74), (1.76) and (1.80) one can obtain the so called King's law:

$$\frac{I_w^2 R_w}{R_w - R_a} = A + BU^n \tag{1.81}$$

Introducing the voltage across the hot-wire, $E_w = I_w R_w$ and using relation (1.76) , equation (1.81) becomes:

$$\frac{E_w^2}{R_w} = (A + BU^n)(T_w - T_a) \tag{1.82}$$

Where the term α_0 was included in the constants A and B. Considering again the case of a CTA mode of operation, in an ambient with constant temperature T_a, both R_w and $(T_w - T_a)$ are constants and can be incorporated into A and B:

$$E_w^2 = A + BU^n \tag{1.83}$$

Expression (1.83) can be fitted on calibration data points to obtain the value of coefficients A, B and n.

1.5.2. *Spatial Resolution*

Despite the already mentioned very good spatial resolution of hot-wires, in wall-flows at higher Reynolds numbers, the smallest turbulent structures can become smaller than the size of the sensing element. This results in the sensor being unable to resolve all velocity fluctuations. This kind of situation is shown in Fig 1.5), with the wire being unable to 'see' the smaller velocity fluctuations. If we make the assumption that the cooling is the sole result of forced convection

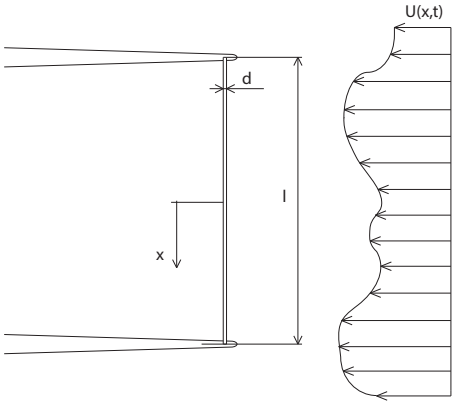

Figure 1.5: A hot-wire sensor with a non-uniform istantaneous incident velocity $U(x,t)$

caused by the normal velocity component U, thus neglecting the tangential and bi-normal velocity contribution, we get that the effective cooling velocity sensed by the wire is essentially given by the normal component, $U_{eff} \approx U$. If the

normal velocity distribution along the wire is not constant, the instantaneous velocity reading will be some kind of spatial average of the velocity distribution along the wire. It is not strictly speaking a spatial average because the heat transfer is not linearly dependent on the effective velocity, taking King's law as an example:

$$\dot{Q} \propto A + BU^n \tag{1.84}$$

So that the "filtered" instantaneous velocity reading is:

$$u_m(t) = \left(\frac{1}{L} \int_{-L/2}^{L/2} U^n(s,t) ds \right)^{1/n} \tag{1.85}$$

Where L is the wire's length and s is the coordinate along the wire with origin in the mid-point. Here n denotes the non linear relation between the heat exchange and the velocity. The effect on the measured quantities is mainly noticeable in an attenuation of the measured velocity variance. Wyngaard (1968) calculated the effect of an incomplete spatial resolution on velocity spectra, using the local isotropy hypothesis. Experimental work is mainly focused on wall flows, where spatial resolution effects are most visible. Ligrani & Bradshaw (1987) investigated the effects of wire's length on the statistics in the near-wall region of a boundary layer. They measured the attenuation on the variance of streamwise velocity, and identified the fundamental parameter characterising spatial filtering in the wire's length in viscous units, $L^+ = L/l_*$. More recently the subject was investigated by Hutchins *et al.* (2009). Segalini *et al.* (2011), Monkewitz *et al.* (2010) and Smits *et al.* (2011*b*) proposed different correction schemes to account for spatial resolution errors.

1.5.3. *End conduction effect*

From previous considerations on spatial resolution it might seem that having a very short wire brings an improvement; unfortunately this is not always the case, as there are limitations on the minimum length of the wire. Not all the heat, in fact, is transferred from the wire by forced convection. Apart from radiation heat transfer which is usually negligible, and natural convection that becomes relevant only at very low velocities, a part of the heat is transferred from the wire to its support via conduction, although this is an unwanted side-effect which should be limited. The forced convection heat transfer is proportional to the surface of the wire exposed to the flow, $Q_{fc} \propto \pi r_w^2 L$; while conduction heat transfer is proportional to the cross section area of the wire, $Q_c \propto \pi r_w^2$; the ratio between forced convection and conduction is $\propto L/d_w$. Ligrani & Bradshaw (1987) in their paper also studied the effect of wire aspect ratio on the measured turbulence intensity, and ended up with the condition $L/d > 200$ in order not to have any attenuation effects.

1.6. Literature Review

Now that the main theoretical basis for wall-bounded turbulence study have been explained, a general overview on influential past works and the ongoing topics of research will be given, to put in context the present investigation. The content will be divided into sections for a better understanding, although in a field such as turbulence research it is difficult to clearly separate topics as they are all fundamentally connected by the physics of the flow.

1.6.1. *Mean velocity scaling*

In recent times the work of Barenblatt (see Barenblatt (1993); Barenblatt *et al.* (1997)), had the effect of provoking one of the most important controversies in the recent history of wall-bounded turbulence but also had the positive effect of stimulating a lot of research on the mean velocity scaling. He proposed that for a high but finite Reynolds number no *complete similarity* is ever reached, resulting in a power law instead of a logarithmic law for the overlap region, using data from the Superpipe as support for his thesis:

$$U^+ = c(y^+)^\alpha \tag{1.86}$$

Further analysis of the Superpipe data by Zagarola *et al.* (1997) however, seemed to support a log-law scaling. Apart from the log law itself, the region of validity and universality are also object of debate (Marusic *et al.* (2013); Vincenti *et al.* (2013)). Viscosity influence is now considered to extend further away from the wall than previously thought and the lower boundary of the log-law has been pushed away from the wall. Some decades ago the overlap region was considered to start at $y^+ \approx 30 - 50$ while now the reported values are higher, although with remarkable differences between them: Monty (2005) reported a value of $y^+ \approx 100$ for channel and boundary layer experiments at $Re_\tau = 4000$. Österlund *et al.* (2000) and Nagib *et al.* (2007) had $y^+ \approx 200$ for boundary layer experiments, while McKeon *et al.* (2005) and Morrison *et al.* (2004) both reported a value of $y^+ \approx 600$ for experiments at very high Reynolds number in the Princeton Superpipe. Some authors proposed the possible addition of an intermediate layer or 'meso-layer' (George & Castillo (1997); Wosnik *et al.* (2000); Wei *et al.* (2005)), interposed between the inner and the outer one. Mckeon *et al.* (2004) proposed a power-law region before the logarithmic layer in pipe flows. The value and the universality of the coefficients (or constants) in the log-law are debated as well, with differences registered between lower Reynolds number channel and boundary layer experiments by Monty (2005) and Österlund *et al.* (2000) that seem to indicate a value of the von Kármán constant of $\kappa \approx 0.38 - 0.39$, while for experiments conducted in the Superpipe $\kappa \approx 0.42$ (Bailey *et al.* (2014)). Nagib & Chauhan (2008) propose that coefficients are actually not universal but flow dependent, and vary between pipes, channels and boundary layers. These coefficients, apart from being an

important aspect of wall turbulence theory, appear in CFD models for the law of the wall and have a big impact in predicting friction in many applications. Reaching conclusions on these aspects has proven to be incredibly challenging due to the very subtle differences in any departure from the log law and in the uncertainties affecting experiments, above all in the determination of the friction velocity u_τ and the wall distance determination, as clearly pointed out by Örlü *et al.* (2010).

1.6.2. *Turbulent fluctuations' scaling*

Although much effort and debate has gone into the scaling of the mean velocity, also the streamwise fluctuation variance $\overline{u^2}$ and to a lower extent, the other elements of the Reynolds stress tensor have been the object of numerous studies. The experimental investigation of these quantities in high Reynolds number flow has always met the problem of spatial resolution, that has undoubtedly limited the progress in our understanding.

Two main issues concern the scaling of the inner-normalized streamwise variance $\overline{u^{2+}}$: the scaling of the inner peak and the appearance of a potential outer peak in the overlap region at high Reynolds numbers. The inner peak is located at $y^+ \approx 15$, and its position appears invariant with Reynolds number. The main debate is related to the magnitude of the inner peak maximum (referred to as u_I^{2+}), in particular if there is an increase with Reynolds number. This is relevant from a theoretical point of view as it would point out that wall-scaling does not hold for turbulent fluctuations, even close to the wall. The high Reynolds number data from the Superpipe does not show an increasing trend, with values of the peak scattered around a mean value of ≈ 8 (Hultmark *et al.* (2010)). A collection of data by Mochizuki & Nieuwstadt (1996) concluded that there is no increase on the inner scaled peak, but subsequent studies by De Graaff & Eaton (2000), Hutchins & Marusic (2007) and Örlü & Alfredsson (2013) seemed to prove that, at least in low to moderate Reynolds number, the increase is real. But the behaviour at higher Reynolds number certainly remains unclear, with only the Superpipe facility being able to deliver data in that range.

Regarding the outer peak, it was reported for the first time in a Superpipe experiment by Morrison *et al.* (2004). Although the experimental study of Hutchins *et al.* (2009) has shown that an artificial outer peak can appear as a consequence of insufficient spatial resolution, subsequent measurement in pipe by Hultmark *et al.* (2010) and boundary layer by Vallikivi *et al.* (2015*b*) at Princeton, have confirmed the appearance of this feature for $Re_\tau > 20000$. This occurs even after correcting it for spatial resolution issues with the scheme proposed by Smits *et al.* (2011*b*). The issue of the rise of an outer peak in u^{2+} is extremely important for the physics of the flow, as it could potentially mean fundamental changes in the flow dynamics at high Reynolds number. The outer

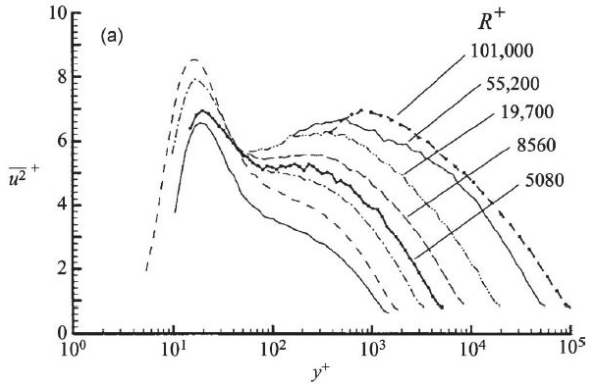

Figure 1.6: The inner-scaled streamwise velocity variance as a function of wall distance in inner units, for various Reynolds number. Reprinted from Morrison *et al.* (2004).

spectral peak has in-fact been linked to the increasing importance of large and very large scales in the logarithmic region of wall-flows.

Marusic *et al.* (2010*a*) used a scale-filtering technique to decompose turbulent fluctuations between small and big scales, and showed that the increase in streamwise normal stress, both at the inner peak and in the overlap region, can be linked to an increase of large scales' energy. Alfredsson *et al.* (2011) proposed a scaling of the streamwise velocity fluctuations based on the diagnostic plot tool, that predicts the appearance of an outer peak at high Reynolds numbers. Conversely, in the scaling proposed by Monkewitz & Nagib (2015), the increase of variance in the overlap and outer region results into a plateau for infinite Reynolds number.

Much less work was devoted to the study of the Reynolds shear stress $\overline{uv}$ and the other Reynolds normal stresses $\overline{v^2}$ and $\overline{w^2}$, mainly due to the added difficulties that determining those quantities implies, most results are derived from low Re DNS. Buschmann & Gad-el Hak (2010) gathered a collection of results from DNS and a few experiments about the scaling in $\overline{v^2}$ and $\overline{w^2}$, pointing out at different trends between confined flows and boundary layers.

The main problem in giving a definitive answer to the scaling of velocity fluctuations is, as formerly discussed, spatial resolution that tends to dampen turbulent fluctuations and artificially decrease the magnitude of u^{2+}. Although efforts have been made to develop correction schemes (Segalini *et al.* (2011), Smits *et al.* (2011*b*), Monkewitz *et al.* (2010)) and give guidelines for maximum values of L^+, the exact extent of spatial filtering close to the wall at high Reynolds number is not fully understood. For these reasons a high resolution

experiment at high Reynolds numbers could be greatly beneficial to expand the knowledge on these quantities.

1.6.3. *Turbulent structures*

Despite the seemingly random nature of wall turbulence, a lot of efforts have been made to identify and study organized motions in the flow field, as perhaps a way to find a general interpretation or explanation to such a chaotic process. The general consensus today is that organized motions can lead to a better understanding of wall-turbulence (Marusic *et al.* (2010*a*)). Although the definition of a coherent structure (or eddy, or motion) is not entirely clear and universal, in general term it can be defined as a region of the flow in time and space characterized by the transport of momentum and mass. These structures and the interactions between them can be used to explain the self-sustaining nature of turbulence. Different kinds of theories/scenarios exist, see for example the theory by Adrian (2007) that uses hairpin-like vortices as the fundamental element of wall turbulence. According to our present understanding, three main categories of coherent structures can be defined, although their exact role and nature is not entirely clear and still in much part controversial: near-wall structures, large scale motions (LSM) and very large scale motions (VLSM).

The first observations on near-wall coherent structures are attributed to Kline *et al.* (1967), that performed flow visualization study down to the viscous sub-layer of a turbulent boundary layer, some of the structures and interaction that they observed are known as *near-wall cycle*. According to current understanding, in the near-wall region ($y^+ < 70$) quasi-streamwise vortices, and wall streaks are present. Streaks are elongated regions in the streamwise direction characterized by high or low momentum, with a spanwise width of the order of $\approx 100\, l_*$, they and appear to be both Re and flow case insensitive. Various theories and scenarios exist for the development of these features. According to one view, the counter-rotating streamwise vortices transports low momentum fluid from the wall upwards and push high momentum fluid close to the wall, causing the formation of streaks. In this sense the near-wall cycle can be considered self-sustaining, and essentially non dependent on outer flow interactions as it remains confined in a small region of the flow field close to the wall. The most relevant works on the near-wall cycle have been collected in a volume by Panton (1997).

Large-scale coherent structures are a more recent discovery, they are of the order of $2-3\,\delta$ in the streamwise direction, where δ is the outer length scale of the flow. These structures are usually referred to as large-scale motions (LSMs), and are associated with the occurrence of bulges of turbulent fluid in the log layer. This motions have been experimentally observed in boundary layers by Tomkins & Adrian (2003) and Ganapathisubramani *et al.* (2005) as composed by packets of hairpin vortices, carrying a considerable part of the Reynolds

shear stress (Ganapathisubramani *et al.* (2003)) and having an important role in the near-wall burst and sweep events. However, doubts on the universality of these hairpin structures remain, particularly at high Reynolds number. While they appear abundantly in the boundary layer DNS of Wu & Moin (2009), the results of DNS of Schlatter *et al.* (2009) appears to be less-organized and much more random, so it is not sure whether a higher development length or Reynolds number would make them disappear.

Even bigger structures have been observed, of the order of $10 + \delta$, usually referred to as *very large scale motions*. VLSMs were first identified in the outer region of pipe flow by Kim & Adrian (1999), who measured structures up to $14\ R$ long, much longer than the integral length scale previously reported. Kim & Adrian made a distinction between Large scale motions (LSM) and VLSMs, with the former being only $2 - 3\ R$ long. They also proposed a mechanical explanation of such features, with LSMs deriving from the axial alignment of different hairpin vortices, that form a "packet" with a region of low momentum between the vortices legs. Likewise, they proposed VLSMs to be the result of multiple packets aligning together, (see Fig. 1.7). Their work sparked the interest in this kind of large features of the flow, that have been intensively studied in the past 15 years. Large and Very Large scale motions were further investigated by Guala *et al.* (2006), who identified the spectral peaks corresponding to them and showed how VLSMs carried roughly half of the total energy but also of the total Reynolds' shear stress, pointing out how these structures were both highly energetic and dynamically important in wall turbulence. Hutchins & Marusic (2007) used a hot-wire rake extending in the span-wise direction in boundary layer, and found structures with a characteristic length of $20\ \delta$, , naming them "superstructures" to differentiate them from internal flows. They also pointed out that it was only for their meandering nature, that their length had been previously underestimated, masked by single point statistics like spectra or auto-correlations. Monty *et al.* (2007) conducted a similar study in pipe and channel flow and managed to identify meandering VLSM structures up to $20 - 25\ R$ long in the log-layer; they also pointed out the difference in span-wise width of these structures compared with BL's superstructures. Mathis *et al.* (2009) observed how these very large features can influence velocity fluctuations of smaller scales close to the wall with an amplitude modulation effect.

Despite undeniable advances, some open questions remain. It seems that large structures depend on the external flow geometry (Monty *et al.* (2009)), but a precise degree of those differences is still unclear. Furthermore, if LSM and VLSM are indeed distinct features in confined and unconfined flows but play a very important role in near-wall turbulence cycle, it is unclear how near-wall turbulence statistics can be so remarkably similar between them. The natural tool for the investigation of coherent structures seems to be DNS and PIV data, that grants the access to multi-component dataset and can be used to study the three-dimensional time evolution of these features. However

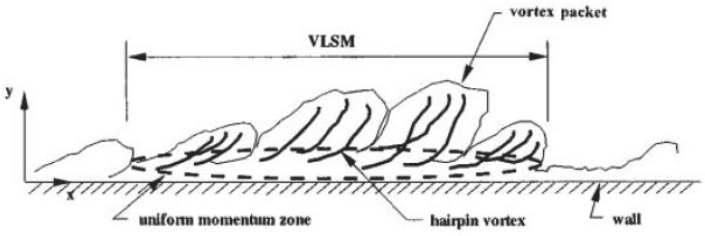

Figure 1.7: The VLSM and hairpin-packets concept. Reprinted from Kim & Adrian (1999).

also these approaches have their shortcomings, as a sufficiently long time evolution and acquisition time is needed to have statistically significant samples. For this reasons also a traditional single-point experimental technique such as hot-wire anemometry can provide very valuable information from velocity spectra (indeed the study of Kim & Adrian (1999) was carried out with hot-film sensors).

The scaling of turbulent spectra has been object of study for a long time; Perry & Abell (1977) and Perry *et al.* (1986) argued how turbulent spectra could be divided in 3 regions according to its scaling: a low-wavenumber region that scales with the characteristic outer length scale δ; an intermediate-wavenumber range that scales with the wall-normal distance y; and a high-wavenumber range that scales with the Kolmogorov length scale η_k. They then argued that at high enough Reynolds number there should be two regions of overlap, one between the low and intermediate-wavenumber regions so that $\Phi_{uu}(k_x) \propto k_x^{-1}$; and one between the intermediate and high-wavenumber regions where $\Phi_{uu}(k_x) \propto k_x^{-5/3}$, the so-called five-third's law, a result first obtained by Kolmogorov (1941) through dimensional analysis. While a $k_x^{-5/3}$ region is well established in turbulent spectra and has been observed many times, a k_x^{-1} region has been incredibly more difficult to observe, with only Nickels *et al.* (2005) reporting a limited region of the spectra showing this behaviour in boundary layer. This particular region is however of great theoretical importance because by integrating the spectra between the low wavenumber limit $k_x\delta$ and upper limit $k_x y$ where the k_x^{-1} scaling holds, for high Reynolds number one gets:

$$u^{2+} = B_1 - A_1 ln(y/\delta) \tag{1.87}$$

which is a logarithmic relation for the inner-scaled variance of the streamwise velocity fluctuations first proposed by Townsend (1976) as a part of his

attached-eddy model. This region was experimentally observed by different authors (Marusic *et al.* (2013); Hultmark *et al.* (2012)).

1.6.4. *The attached eddy model*

Here a quick review of what has become known as the attached eddy model, will be given, highlighting the main hypotheses behind it and the resulting predictions. The attached eddy model was first formulated by Townsend (1976) and then expanded upon and adapted in numerous other works (most notably Perry & Chong (1982) and Perry *et al.* (1986)). It represents one of the very few attempts at a wall-turbulence model, and has generally gained positive support from experimental data throughout the years.

In his book, Townsend (1976) developed a model based on an array of differently sized eddies whose dimensions scaled with the distance from the wall. These eddies can be considered 'attached' in the sense that, at a distance y_0 from the wall, the characteristic eddy centre is located at y_0 and its influence (the induced velocity field) extends down to the wall. The funding hypothesis of the model is that velocity fluctuations of a turbulent wall-bounded flow can be described with a random superposition of attached eddies of different sizes. Those eddies should have the same shape and induce the same velocity field that is representative of the mean energy-containing vortex structures in the flow, even if they might not be representative of real instantaneous vortices.

Townsend proceeded to derive the expression for the contributions of a random attached eddy distribution to correlations and then obtained the function of eddy size with wall distance necessary to produce constant shear stress $\overline{uv}$, as was observed. He obtained a population density of eddy with size y that was inversely proportional to y, So that population density of eddies of size y per wall area is equal to Ky where K is a constant (in other words eddies become bigger but fewer with increasing distance from the wall). With these assumptions he derived the behaviour of the normal Reynolds stresses:

$$u^{2+} = A_u - B_u \, ln(y/\delta) \tag{1.88}$$

$$v^{2+} = B_v \tag{1.89}$$

$$w^{2+} = A_w - B_w \, ln(y/\delta) \tag{1.90}$$

where u^{2+}, u^{2+} and u^{2+} denote respectively the streamwise, wall-normal and spanwise Reynolds stresses, and A_u, B_u, B_v, A_w and B_w are constants that depend on the particular type of eddy chosen for the random distribution. It is important to note that these results do not depend on the geometry or field of the attached eddy, but are derived exclusively from the hypotheses of attached eddies and a constant shear stress. Townsend also made the distinction between active and inactive motions; he recognized that at a given wall-normal distance from the wall, the stress v^2+ and the shear stress uv^+ contributions come

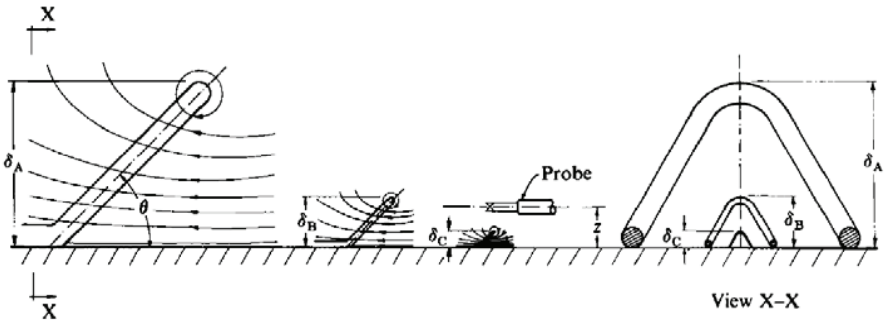

Figure 1.8: The hairpin-like eddy geometry used by Perry & Chong (1982). Figure from Perry *et al.* (1986).

essentially only from attached eddies with the centre at or close to y. In contrast, the normal streamwise and spanwise components u^{2+} and w^{2+} are due to every eddy bigger than y, and that is why these two terms grow going towards the wall (the number of eddies higher that y increases). So he called 'inactive motions' those that contribute little to the shear stress. It should be noted that the property of being inactive is only with respect to the particular point of the flow field considered and is not characteristic of a particularly sized eddy *per se*. Although the expression (1.89) is valid whatever the specific eddy might be, the value of the constants therein depends upon it. The expressions above really only apply to the main turbulent motion, which essentially relates to that region where the important length-scale is distance from the wall and the important velocity scale is the wall shear velocity, which is essentially the log-law region. Townsend adopted a description of conical vortices that seemed to produce good results. Later, Perry & Chong (1982) adopted another form of eddy which can be identified as an horseshoe or hairpin vortex (see Fig. 1.8), that were recently observed in the flow visualization by Head & Bandyopadhyay (1981). Using this eddy geometry, with a population density inversely proportional to wall distance (the same used by Townsend), they managed to reproduce the logarithmic profile of the mean streamwise velocity and they also derived the spectral energy distribution resulting from the superposition of attached eddies. This in particular, resulted in the emergence of a k^{-1} region in the streamwise velocity spectrum as an additional overlap region between outer scales ands, with k being the streamwise wavenumber, at a wall-normal location y sufficiently close to the wall.

From a physical point of view, the presence of a k^{-1} region in the spectrum can be explained in terms of the induced velocity fluctuations by attached

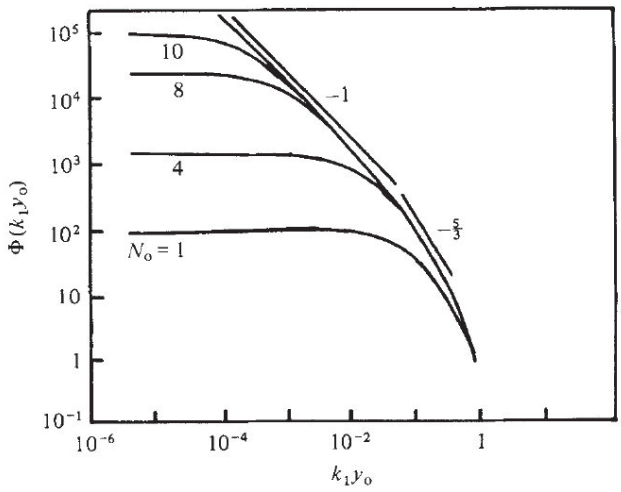

Figure 1.9: The k^{-1} region of the spectra. Figure from Perry & Chong (1982).

eddies. At a given distance from the wall y, the streamwise or spanwise fluctuations will only be influenced by contributions from eddies of height greater than y. So for a k^{-1} region to appear at a wall-normal distance of y the eddies contributing to it are the ones ranging from a height of $0.1\,\delta$ to a height of y, and in order to be able to see a sizeable region of $k^{-}1$ spectrum, sufficient scale separation should be attained.

In more recent development on the model Marusic (2001), used elongated structures simulating hairpin packets as the geometry for attached eddies. While the attached eddy model predictions regarding the Reynolds stresses have enjoyed a good degree of support from numerical and experimental results, the predicted $k^{-}1$ spectral region has been extremely elusive, apart from the experiment results reported in Nickels *et al.* (2005).

1.7. Previous high Reynolds number experiments

As previously described, high Reynolds number are extremely important in understanding the nature of wall-bounded turbulence, and the experimental approach is currently the only tool for the evaluation of such flows. To give a context for the experimental work carried out in the Long Pipe facility, here the principal wall-bounded turbulence experiments and their results will be examined.

1.7.1. *Boundary layer*

Zero pressure gradient turbulent boundary layer (ZPG TBL) is, alongside pipe and channel flow, one of the 'canonical' wall turbulence cases, and as such has been extensively investigated by experiments. One key difference with the other two flows is that, due to the absence of a pressure gradient, it requires an alternative way to estimate wall friction. This is a rather important aspect as it impacts the accuracy of wall-scaling and unlike internal flows, it lacks a reliable and accurate method for wall-friction determination. Currently the best method for an independent determination of wall-friction is oil-film interferometry that can reach uncertainty levels of the order of $1-2\,\%$ (Ruedi *et al.* (2003)). Another possible issue related to boundary layer experiments is the spatial development and the reaching of what can be considered a canonical state. Chauhan *et al.* (2009) noticing the scatter in boundary layer data tried to set criteria for their evaluation. In the last 15 years or so the main sources of boundary layer data were the KTH Minimum Turbulence Level (MTL) wind tunnel in Stockholm (Österlund *et al.* (2000)), the NDF wind tunnel at Illinois Institute of Technology in Chicago (Nagib *et al.* (2007)) and the boundary layer facility at the University of Melbourne (Nickels *et al.* (2005)).

The MTL wind tunnel has a $1.2\ m \times 0.8\ m \times 7.0\ m$ test section and can reach $Re_\tau \approx 14000$ with a free stream velocity of $\approx 70\ m/s$. It has been designed for transition and stability studies and has an excellent flow quality thanks to a contraction ratio of 9:1 and a very careful use of turning vanes, screens and honeycomb. Free stream turbulence intensity is $< 0.02\ \%$ and the temperature stability is $\pm 0.05\ ^\circ C$.

The NDF facility in Chicago has $1.52\ m \times 1.22\ m \times 10.03\ m$ test chamber, and is equipped with turning vanes, honeycomb and a 6:1 contraction. The resulting free-stream turbulence intensity is $< 0.05\ \%$ at all velocities. It can reach a friction Reynolds number up to $Re_\tau \approx 22000$. It is equipped with a modular test section and adjustable ceiling panels that allow the study of favourable or adverse pressure gradients (Nagib *et al.* (2006)).

The Melbourne BL facility, called High Reynolds Number Boundary Layer Wind Tunnel (HRNBLWT), with 27 m of development length and can reach a friction Reynolds number $Re_\tau \approx 10^4$ while still maintaining a viscous length scale $l_* \approx 25\ \mu m$. Details of the facility are given in Nickels *et al.* (2005) and Nickels *et al.* (2007).

The Flow Physics Facility (FPF) in New Hampshire (Vincenti *et al.* (2013)) became operational in 2011, and represents the large scale facility approach applied to a boundary layer. It currently consists in an open loop set-up with no contraction section but a set of screens to reduce turbulence intensity of the free stream below 0.5 %. The main feature of the facility is the test chamber that with its dimensions ($2.8\ m \times 6\ m \times 72\ m$) makes it the largest boundary

layer facility in the world. At $Re_\tau \approx 10^4$ the corresponding viscous length is $l_* \approx 70\ \mu m$.

Recently at Princeton University, a boundary-layer pressurized facility called HRTF and similar in concept to the Superpipe has been completed, described in detail by Jimenez *et al.* (2010). In consists in a 2 m long flat plate over which a boundary layer develops, reported values of the free stream turbulence intensity are $0.3 - 0.6$ %. It offers the advantage of reaching higher Reynolds numbers than all other facilities, although at the expense of viscous length scale. A detailed analysis on turbulence statistics for $2500 < Re_\tau < 72000$ was performed by Vallikivi *et al.* (2015*b*).

1.7.2. *Atmospheric surface layer*

The earth's atmospheric surface layer (ASL) can be the source of unique experimental data. The Surface Layer Turbulence and Environmental Science Test (SLTEST) site in the Great Salt Lake Desert, established by Metzger & Klewicki (2001), takes advantage of the flat and smooth geographic feature of the location to achieve extremely high Reynolds number without the spatial resolution problem that would affect a traditional laboratory experiment.

Results from the ASL seem to make it comparable to a canonical ZPG turbulent boundary layer, although doubts regarding the non stationarity, boundary conditions and thermal effects remain. Despite the benefits of the facility in terms of Re and spatial resolution, the main challenges and shortcomings are all essentially linked to the inability to control the flow. The flow stability, direction, and acquisition time necessary to obtain statistically relevant results have been carefully assessed, but of course the uncertainty levels remain an order of magnitude above those of a traditional laboratory experiment. Nonetheless, the relevance of this data should be underlined as it provides an insight into extremely high Reynolds number behaviour, albeit not very detailed, that would otherwise have been impossible to obtain.

1.7.3. *Pipe flow*

One of the most influential pipe experiment after the work of Reynolds (1883) was by Nikuradse (1933), that measured mean velocity profiles and friction coefficient in a smooth and rough pipe flow. The friction coefficients found today in engineering textbook for cases of turbulent flow in smooth and rough pipes are essentially based on his experiment. It is also by fitting his results that Prandtl came up with a value of the von Kármán constant $\kappa = 0.41$.

Many past experiment were characterized by largely different values of the development length of the pipe (Nikuradse (1933) used $L/D = 40$, while $L/D = 398$ in the case of Perry *et al.* (1986)), for this reason some effort has been spent in establishing the required development length for the achievement of a fully developed state. Doherty *et al.* (2007) conducted a study in the

Melbourne pipe facility and reported a development length of 50 diameters for the mean velocity to reach a fully developed state, while 80 diameters are needed for higher order statistics and spectra. In a similar study Zimmer *et al.* (2011) concluded that, after $L/D \approx 70$ the statistical moments up to the fourth order become invariant with the axial coordinate.

The most influential high Re pipe experiments in recent decades have probably been those performed in the Princeton Superpipe facility, for two main reasons: the results have provided data at unprecedented Reynolds number, but also sparked a debate both on mean scaling (Barenblatt *et al.* (1997)) and on turbulence intensities (Örlü & Alfredsson (2013)). It is a unique facility were the air inside the wind tunnel can be pressurized up to $230\,atm$, reducing the fluid kinematic viscosity and achieving extremely high Reynolds numbers ($Re_\tau \approx 500 \times 10^3$), although at the expense of spatial resolution ($l_* \approx 0.6\ \mu m$ at $Re_\tau \approx 10^5$), given the relatively limited pipe diameter of 129 mm. The first data, comprising mean velocity and pressure drop, has been published by Zagarola & Smits (1998). Data from the facility has since then been corrected and re-interpreted by various authors, most notably McKeon *et al.* (2005) and Bailey *et al.* (2014). Additional hot wire measurements were performed by Morrison *et al.* (2004) and Hultmark *et al.* (2012). Recently a new concept of nano-scale hot-wire anemometer was used in the facility by Bailey *et al.* (2010), with a length of the sensing element $\approx 30\,\mu m$ compared to a standard hot wire length of $\approx 200\,\mu m$.

Recently also other high Re facilities have become operational: the Hi-Reff water pipe flow facility in Tsukuba, Japan and the CoLaPipe facility in Cottbus, Germany. The Hi-Reff facility uses water as the operating fluid and a gravimetric tank for a precise measurement of the bulk velocity. Two pipe sections can be used in the facility, one with a diameter of 100 mm and the other with a diameter of 387 mm. Furuichi *et al.* (2015) measured the friction factor with a very high degree of accuracy and mean velocity profiles using LDV up to $Re_\tau \approx 14 \times 10^3$. The Colapipe facility (König *et al.* (2014)) is a closed loop wind tunnel with diameter of the test section of 190 mm and of the return circuit of 342 mm, with aspect ratios L/D equal to 148 and 79, respectively. Both the test and return sections are completely made out of acrylic glass and are therefore ideally suited for extensive optical measurements.

1.8. Objectives of the thesis

Now that the mathematical and theoretical concepts regarding wall-bounded turbulent flows have been presented, together with a brief overview of the state of the art in the field, a more detailed description of the objectives of this investigation can be given. As already motivated in the introduction, the experimental approach remains our only tool for the investigation of high Reynolds number turbulence, yet it comes with great challenges that have so far been an hindrance for the advancements in our understanding, the most

important of which is the need for an extremely high spatial resolution. The overall aim of this experimental investigation is to expand our understanding on high Reynolds number turbulent wall-flows, making use of the exceptional resolution of the Long Pipe facility. In particular, the objectives of the thesis can be summarized as follows:

- **Characterization of the Long Pipe**. Being a new facility, a first objective is the characterization of the wind tunnel to ensure a correct and stable operation of the facility, but also to check that the flow corresponds to a canonical fully developed pipe flow. Particular attention is given to static pressure measurements along the pipe that are used to determine the friction velocity and are therefore of particular importance for the scaling of all the measured quantities. Additional measurements are also performed to test the symmetry and stability at different flow regimes.
- **Scaling of turbulent fluctuations**. The elements of the Reynolds stress tensor $\overline{u_i u_j}$ appear in the Reynolds averaged Navier-Stokes equations (RANS) that describe the dynamics of mean quantities in a turbulent flow. A description of these terms is needed to 'close' the turbulence problem, and every turbulence model has to take this into account. Despite being extremely important, their behaviour is object of debate and there is still no general consensus, even on the scaling of the streamwise normal stress $\overline{u^2}$. The main difficulty is that data from DNS is limited to low Reynolds number, while experimental data at high Re is affected by spatial resolution. One of the aim of the thesis is the characterization of these quantities, taking full advantage of the extra-ordinary resolution granted by the Long Pipe, to study their behaviour over a wide range of Reynolds numbers.
- **Structure and dynamics of turbulence**. For a detailed description of high Reynolds number turbulence, a quantitative characterization of Reynolds stresses is not enough; another important information is knowing how and when these stresses appear in the flow. Fluctuations can be associated with characteristic scales of motion trough a spectral analysis. In the last decade a lot of work was dedicated to the investigation of turbulent structures since the discovery of much larger coherent motions than previously believed. Although the general consensus now is that these large motions play an important role in wall turbulence and can influence and modulate the behaviour of smaller near-wall vortices, their exact nature and similarity (or lack thereof) between different wall-flows is still unclear. In particular the analysis is aimed at studying the characteristic length-scales and magnitudes associated with these motions at high Reynolds number. Additional insight in the dynamics of wall

turbulence can be gained by associating turbulence fluctuations with the occurrence of strong events. Using the technique of quadrant analysis it is possible to link the instantaneous value of $uv(t)$ with near wall events such as ejection and sweeps. These are very strong and intermittent movement of fluid from or to the wall linked to the production of Reynolds shear stress. The aim of the analysis is studying their contribution and role in high Reynolds number turbulence.

CHAPTER 2

The CICLoPE Laboratory

2.1. The need for a high Re facility

The idea behind the construction of the CICLoPE laboratory, and the Long Pipe (LP) facility in particular, is to provide a tool for the investigation of high Reynolds number wall turbulence in a way that has so far not been possible in other facilities. Although high Re wall turbulence appears in many flows of industrial and environmental interest, no data-set currently available is detailed enough to develop reliable models and to give definitive answers to fundamental questions on the physics behind the phenomenon. The overwhelming complexity of turbulence and its diversely sized motions are an enormous challenge for any experimental investigation. Space resolution in particular becomes a severe hindrance when high Reynolds numbers are concerned, and the Long Pipe is devised from the start to tackle this issue. The long pipe at CICLoPE has been designed to reach high Reynolds number but at the same time allow fully resolved measurements of all turbulent scales in the flow with traditional and well-established sensors, making it the first facility in the world to achieve both. The main design parameters of the Long Pipe were decided based on these two requirements by an international group of scientists in the field of wall-turbulence as reported in Talamelli *et al.* (2009).

The first requirement that should be set is the operational Reynolds number range that should be provided by the new facility, and to do this, the features of what can be considered a 'high' Reynolds number flow have to be specified. The defining traits of a high Re wall-bounded flow are two: a well developed overlap region in the mean velocity profile, and a well developed $k^{-5/3}$ region in wave-number spectrum. For the mean velocity profile, it is well-established that an overlap region exists at high Reynolds number, and is well-described by the logarithmic relationship of eq. (1.65). If the boundaries of this region are assumed to be $y^+ > 200$ and $y < 0.15\ R$ (where R is the pipe radius), and the logarithmic behaviour is required to extend for at least a decade (up to $y^+ = 2000$) then:

$$2000\, l_* < 0.15\ R \tag{2.1}$$

$$R^+ = Re_\tau > 13.3 \times 10^3 \tag{2.2}$$

which is the minimum Re_τ value that fulfils this requirement. In order to have enough operational range to study Reynolds number scaling, a factor of 3 is applied, ending up with a maximum Re_τ requirement of 40×10^3. For the emergence of a $k^{-5/3}$ region in the spectra instead, as theorized by Kolmogorov (1941) and observed in many turbulence measurements and numerical simulations, the condition to fulfil is a sufficient scale separation between the Kolmogorov scale η_K and the energy containing scale l_0, that in the case of a pipe can be taken as the diameter D. The $k^{-5/3}$ region is expected to appear at a wavenumber k one order of magnitude smaller than the Kolmogorov wavenumber and continue down to a wavenumber one order of magnitude bigger than the energy containing wavenumber D^{-1}. Using data from DNS and eq. (1.70), η_K at the centreline can be estimated for $Re_\tau = 14000$ at $\eta_{K_{CL}} = 10.6\, l_*$. This means that the $(-5/3)$ region would start from scales $\approx 106\, l_*$. If then it has to extend for at least a decade, up to $\approx 1060\, l_*$, the following has to be satisfied:

$$1060\, l_* < 0.1\, D \tag{2.3}$$

$$R^+ = Re_\tau > 5.3 \times 10^3 \tag{2.4}$$

as can be seen, the condition is fulfilled for the lower limit of the operational range at $Re_\tau = 13300$. The operational range of the facility is thus fixed at $13.300 < Re_\tau < 40000$.

Now that a value for what can be considered a high Reynolds number has been established, a method to achieve that Re range has to be devised. Looking at its definition:

$$Re = \frac{UL\rho}{\mu} \tag{2.5}$$

it is immediately clear that various strategies can be employed to increase Re. While the most direct method would seem to increase the speed of the flow U, this would also greatly increase the power needed, and the approach is limited by the appearance of compressibility effects. Increasing the density ρ with a pressurized facility is also a viable option, and this is the approach taken with the Superpipe facility (Zagarola & Smits (1998)), that can reach up to 187 atm in the test section and achieve Re_τ values in excess of 10^5. Another method would be to decrease the dynamic viscosity μ which appears in the denominator of eq. (2.5), and this is what happens in a cryogenic facility.

All the aforementioned methods to increase Reynolds number however, inherently imply a deterioration of spatial resolution for a given flow geometry. In wall turbulence in-fact, the characteristic length scale in the inner region is the viscous length l_*, defined in eq. (1.57). The well-known relationship between the friction Reynolds number Re_τ and the viscous length scale is:

$$l_* = \frac{R}{Re_\tau} \tag{2.6}$$

Where R is the flow characteristic outer scale, in this case the pipe's radius, but could also be the channel half height $h/2$ or the boundary layer thickness δ. This relationship implies that increasing Reynolds number without modifying the outer dimension of the flow results in a decrease of l_*. The smallest (on average) scale of turbulent motions is the dissipative Kolmogorov scale η_K defined in eq. (1.67). However, as shown in Smits *et al.* (2011*b*) the ratio η_K/l_* for a wall flow is independent on Re and nearly constant close to the wall with an value of ≈ 2. For this reason, l_* can be used instead of η_K to describe the size of the smallest turbulent scales that are found near the wall, and the parameter $L^+ = L/l_*$ can be used to quantify the magnitude of spatial filtering when using a sensor of size L. Specifically, hot-wires sensors will be considered here, since they are the most widely used sensors in turbulence research and provide excellent spatial and temporal resolution. The main effect of an insufficient spatial resolution is the measurement of an attenuated velocity variance, as fluctuations associated with smaller scales are averaged over the length of the wire. Numerous experimental studies have quantified the effects of spatial filtering on hot-wire sensors; Ligrani & Bradshaw (1987) in their experimental study have found that for $L^+ < 20 - 25$ no attenuation was measured on the magnitude of velocity fluctuations. Later studies by Smits *et al.* (2011*b*) and Hutchins *et al.* (2009) found a discernible difference on streamwise velocity variance down to $L^+ \approx 10$. For the Long Pipe sizing, this value was taken as the limit for the appearance of spatial filtering. The smallest traditional hot-wire sensor (not considering nano-scale sensors like the one described in Bailey *et al.* (2010)) that can be produced has a diameter of 0.6 μm and a minimum length of 120 μm to avoid end conduction effects. If the condition $L^+ < 10$ is imposed for this hot-wire:

$$\frac{L}{l_*} < 10 \tag{2.7}$$

$$l_* > \frac{L}{10} = 12\mu m \tag{2.8}$$

So, in order to encounter no spatial filtering effect at the highest operational Reynolds number of the facility ($Re_\tau = 40000$):

$$Re_\tau = \frac{R}{l_*} = 40000 \tag{2.9}$$

$$R = 40000 \times 12\ \mu m = 0.48\ m \tag{2.10}$$

This is the requirement for the minimum size of the pipe radius R, channel half height $h/2$ or boundary layer thickness δ, depending on the type of flow considered.

As far as canonical wall-flows go, a pipe flow, compared to a boundary layer, has the distinct advantage of an easier and more accurate measure of wall friction via pressure drop. It is also better suited to a large scale facility than a channel flow, which would require a section with a very high aspect ratio to avoid interference from the lateral walls, and would ultimately be impractical. For this reasons a pipe flow was selected, and the development length needed to reach a fully developed state, based on experimental studies (Zagarola & Smits (1998)) was estimated at 100 D, that for a radius of $R \approx 0.48m$ results in a length L of the pipe of just under 100 m. In Fig. 2.1 the operational range of such a facility in shown in the (l_*, Re_τ) space, the horizontal line represents a sufficient spatial resolution at $l_* = 12\ \mu m$, while the vertical line is the start of what can be considered a high Reynolds number range, at $Re_\tau = 13300$. It can be seen how the Long Pipe operates in a previously unexplored area of high resolution and high Reynolds number in the upper-right quadrant.

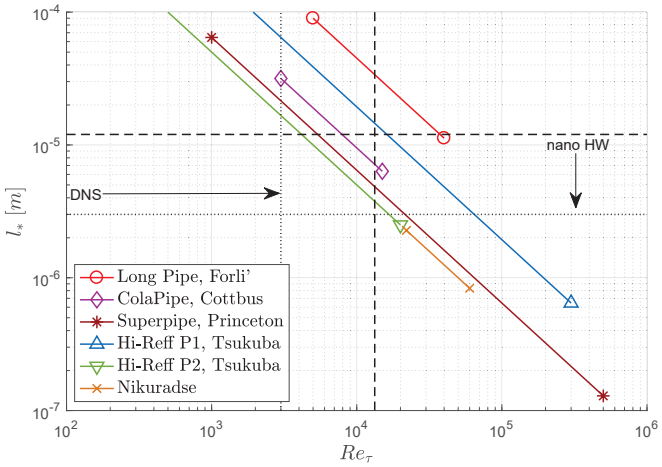

Figure 2.1: Viscous length scale as a function of friction Reynolds number for various experimental facilities. Vertical dashed line represents the start of high Reynolds number region at $Re_\tau = 13300$; vertical dotted line is the highest reported DNS in pipe flow ($Re_\tau = 3008$ by Ahn *et al.* (2015)); horizontal dashed line is the fully resolved measurement for a traditional high aspect ratio 125 μm hot-wire; horizontal dotted line is the fully resolved measurament for the 30 μm nano-scale NSTAP sensor by Bailey *et al.* (2010).

2.2. The Long Pipe layout

The requirements detailed in the previous section resulted in the design of the Long Pipe. The facility consists in a closed loop wind tunnel, whose test section is a 111.5 m long pipe with a circular test section. The facility is installed in one of the two 130 m long underground tunnels (see Fig. 2.2) of the former *Industrie Caproni*, one of the major producer of aircraft in Italy between 1930 and 1943, located in Predappio. The tunnels were excavated under the mountains prior to the second world-war, for the assembly of aircraft during bombing raids. The closed loop design ensures stable flow conditions, and low turbulence level; it includes a heat exchanger to control temperature within the range of $\pm 0.1\ ^{\circ}C$, and a flow-conditioning assembly composed of honeycomb, 4 screens, settling chamber, and a convergent with contraction ratio $CR = 4$, the maximum achievable given the dimensional limitations of the installation site. In Fig. 2.3 is shown a schematic of the wind tunnel, with a description of its main elements.

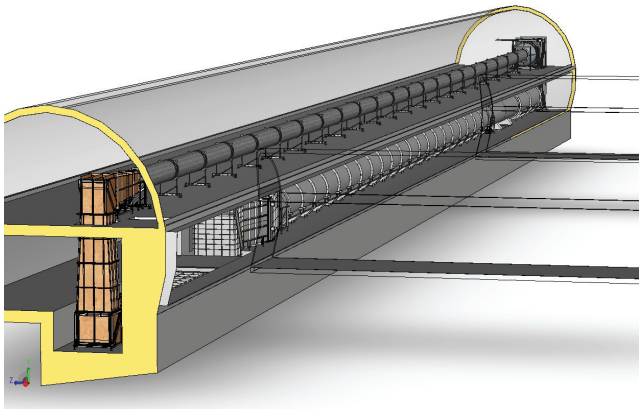

Figure 2.2: Overview of the Long Pipe installation inside the Caproni underground tunnel.

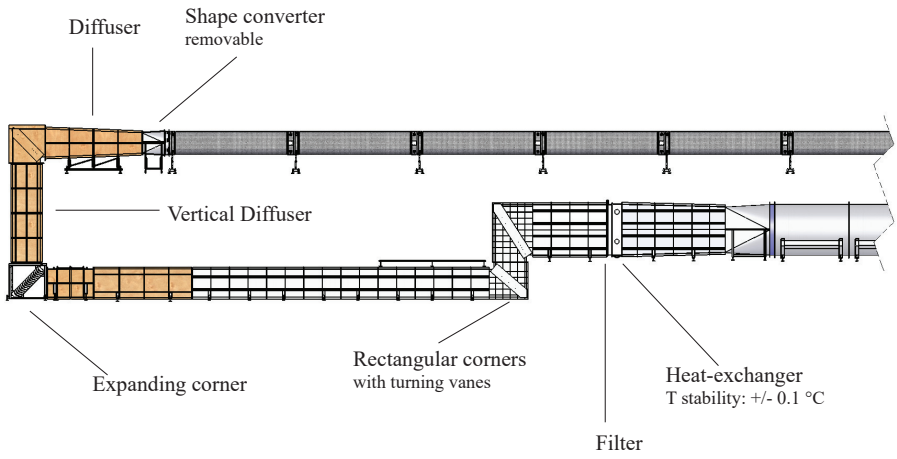

Figure 2.3: Schematic of the Long Pipe wind tunnel

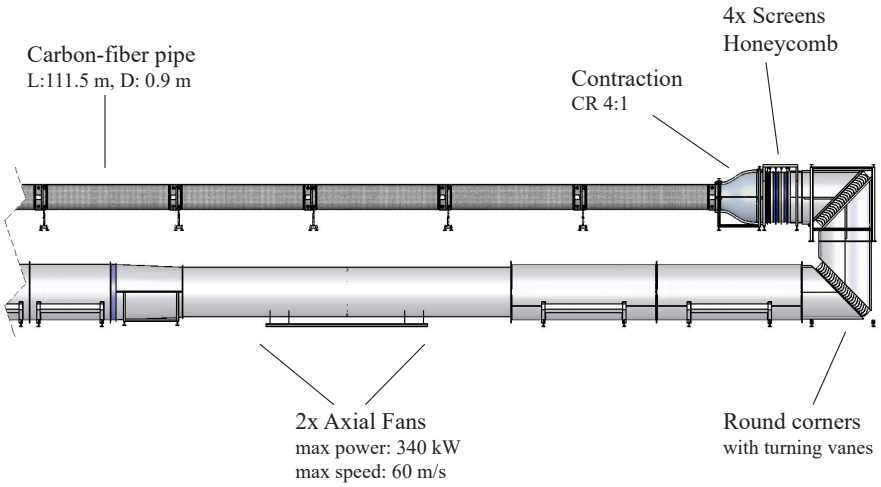
4x Screens
Honeycomb
Carbon-fiber pipe
L:111.5 m, D: 0.9 m
Contraction
CR 4:1
2x Axial Fans
max power: 340 kW
max speed: 60 m/s
Round corners
with turning vanes

The main element of the flow-loop, which accounts for 60 % of the total pressure losses, is a round pipe of constant cross-section. In Fig. 2.5 are shown some details of it. The pipe is 111.5 m long with an inner diameter of 900 mm, resulting in a L/D of about 123. The pipe is made of twenty-two 5 m long carbon-fibre elements, plus a final one 1.5 m long, produced using the filament-winding technology (see Fig 2.8b). This allowed the achievement of a surface roughness of $k_{rms} < 0.2\ \mu m$ ($k^+ < 0.02$), and a diameter precision of 900 ± 0.2 mm. All pipe elements are equipped with 4 axially-spaced static pressure taps and four access ports of diameter of 150 mm distributed radially to provide access to the pipe. The access ports are in aluminium and machined to sit flush with the inner surface of the pipe, as shown in Fig. 2.5d.

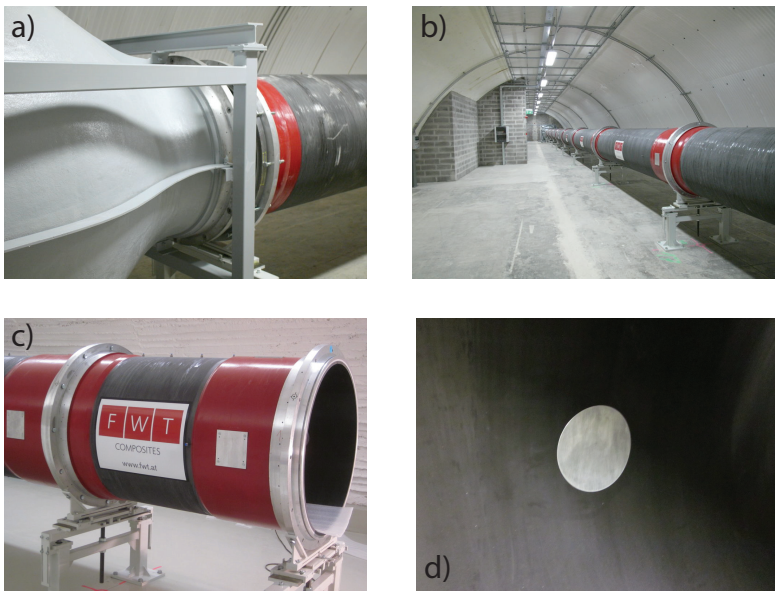

Figure 2.5: Elements of the test section. a) Convergent section and pipe. b) View of the pipe. c) Final pipe section of 1.5 m. d) Access port as seen from inside the pipe.

The test section is linked to the return circuit, one floor below, through a removable shape converter and a series of diffusers and corners. Various details of the return circuit are shown in Fig. 2.6-2.7. One peculiarity of this wind tunnel is that it includes six corners (instead of the four that are normally needed): the return duct first runs under the floor of the main laboratory to allow access to vehicles and then rises above the floor of the main tunnel

trough two expanding corners placed before the heat-exchanger (see Fig. 2.6b-d). In total, the circuit includes four rectangular expanding corners and two non-expanding circular ones, and all of them are equipped with turning vanes. The fan group has been designed to provide a pressure rise of 6500 Pa at a volume flow rate of 38 m^3/s, which corresponds to a velocity of 60 m/s in the test section. It is composed of two, two-stage counter-rotating axial fan mounted in series. Each axial fan includes two propellers mounted on a common motor powered by a dedicated inverter. Fan diameter is 1.8 m, a total length of 4.2 m and the maximum absorbed power is 340 kW. For twenty meters before and after the fans, the straight cylindrical elements of the return circuit are equipped with noise absorbing material (see Fig. 2.7c). For the current experimental campaign, only one of the two fan was operative, enabling the wind tunnel to reach a maximum centreline velocity of 40 m/s in the test section.

Figure 2.6: Elements of the return circuit. a) Rectangular to round shape converter after the heat-exchanger. b) Diverging section prior to the heat exchanger. c) Cylindrical elements of the return circuit. d) Section of the return circuit running under the floor prior to final assembly.

Temperature and humidity levels are controlled separately for the main tunnel area and for the laboratory (where the smaller 1.5 m section is located) with two air conditioning system, that are placed outside the site. The flow inside the wind tunnel, the two inverters and the electrical motors of the fans

Figure 2.7: Elements of the return circuit. a) Return circuit as seen from the heat-exchanger. b) Rectangular corner with turning vanes prior to final assembly. c) Cylindrical corner and noise-absorbing cylindrical elements d) Fan sections.

are all liquid-cooled through a refrigerating circuit that has an evaporating tower outside (see Fig. 2.9).

Figure 2.8: Elements during construction a) Axial fan prior to mounting showing first stage fan blades. b) Pipe section during the filament-winding manufacturing process.

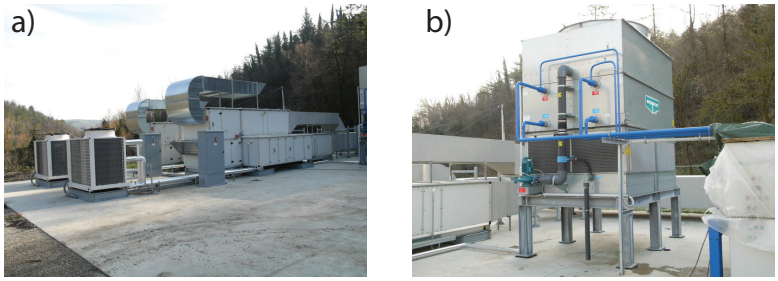

Figure 2.9: External systems. a) Systems for the air-conditioning of tunnel and laboratory. b) Evaporating tower for the cooling of fans, inverters and .

2.3. Experimental apparatus

Measurements are generally performed at $L/D = 123$, in the last 1.5 m long section before the shape converter. Two different traversing units have been designed and built for the Long Pipe. They are designed to fit the 150 mm round access ports that are found on every pipe section, which allows the mounting at different L/D stations and different azimuthal positions all along the pipe. The first traversing unit, shown in Fig. 2.10 and referred to as the 'small traversing', consists in a composite hollow air-foil that slides through the pipe wall. This traversing was designed for near-wall measurements and the main design focus was on minimum aerodynamic interference and maximum positioning accuracy. For this reason the system only requires one access port and the screw, bearings and guide rods are all placed outside the pipe, with only the profile and probe-holder being inside the test section. Cables from the sensor mounted on the traversing are conveyed outside through the hollow profile. The traversing spans from the wall up to $\approx 0.3\ R$, is operated via a stepper motor with a 10 μm resolution step and its position is retrieved using a Renishaw Tonic T100x relative optical linear encoder with a resolution of 0.5 μm. Using a linear encoder fixed on the moving part of the traversing ensures that any play in the mechanism will be measured and accounted for during profile acquisition.

The second traversing unit (see Fig. 2.11), referred to as 'global traversing', was designed to measure along all radial locations in the pipe section, from one wall to the other. It also offers a greater degree of flexibility at the expense of a bigger blockage and can hold multiple probes. The mounting requires the use of two opposite access ports and both the guide rods and the screw are located inside the pipe. It is operated with a similar stepper motor to the other traversing, but position is measured with an integrated rotative encoder

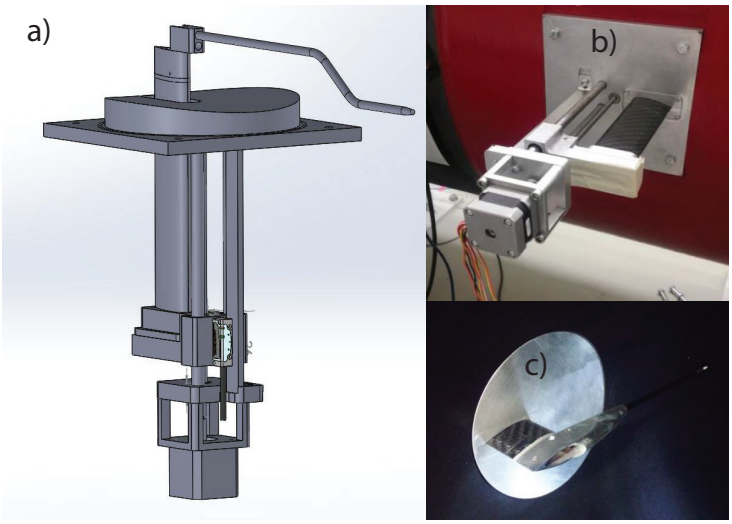

Figure 2.10: Small traversing. a) CAD model. b) Traversing when mounted, as seen from outside the pipe. c) Traversing as seen from inside the pipe.

mounted on the motor shaft. Both steppers are operated with National Instruments NI-9501 modules mounted on a cRIO 9068 chassis, while the digital signal from the encoders are read with a NI-9401 digital I/O module.

Static pressure drop along the pipe is measured trough 1 mm pressure taps placed on every pipe element. Pressure taps arrangement for each 5 meter section is as follows: taps are present in 5 longitudinal locations (with 1 meter separation between them) one of which consists of 4 azimuthally spaced taps, while the other 4 are single taps. Static pressure along the pipe is acquired with a 32-channel digital pressure scanner Initium, with a 2500 Pa range. Acquisition frequency of the instrument is kept at 10 Hz and the results are averaged over the duration of the experiment for the determination of u_τ. For the current measurements up to 19 channels have been acquired, extending to ≈ 70 meters upstream of the test section. Mean centreline velocity can be measured with a fixed L-shaped Prandtl tube mounted on a support that fits the pipe access ports. The difference between the total and static pressure is then acquired with an MKS Baratron 120AD differential pressure transducer with a 1333 Pa range, at a rate of 10 Hz. The ambient pressure and the temperature inside the test chamber are acquired respectively with a MKS Baratron 120A absolute pressure transducer and a PT 100 thermistor, and are then used to get the air density value.

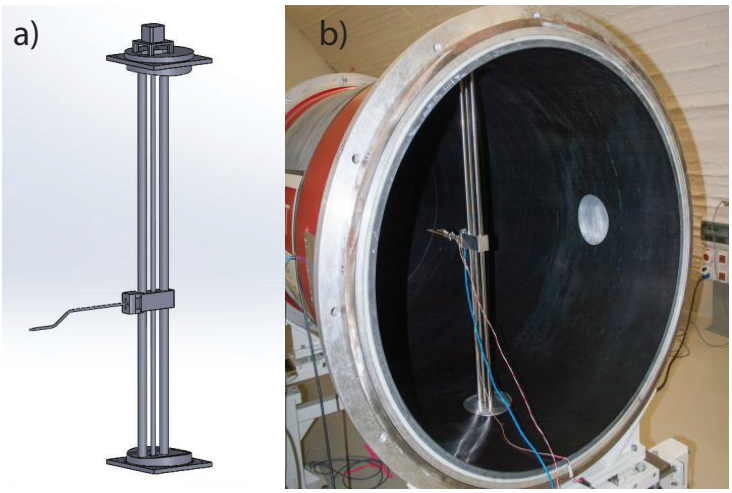

Figure 2.11: Global traversing. a) CAD model. b) Traversing mounted vertically in the test section.

2.3.1. *Hot-wire sensors*

The hot-wire probes used are custom made x-wire and single-wire type. The wires are Platinum Wollaston wires with a diameter of 5, 2.5 and 1.2 μm. The wires are soldered on steel prongs that have been electro-etched in a 65 % nitric acid solution to obtain an aerodynamic shape. The prongs' spacing is chosen to keep the wire aspect ratio L/d as close to 200 as possible, following the recommendation of Ligrani & Bradshaw (1987). Some pictures of the single-wire type of probes are shown in Fig. 2.12. In addition, a Dantec 55P11 commercial probe was also used, with a 5 μm thick and 1.1 mm long Tungsten wire. Concerning the x-wire probes, only one Platinum wire type with diameter equal to 2.5 μm was used, Spacing between the prongs is 0.5 mm and the wires are placed at $\approx \pm 45°$ with respect to the probe's longitudinal axis, resulting in a wire length of $\approx 0.7mm$ and a wire aspect ratio $L/d \approx 280$. The two wires have a separation of $\approx 0.75 - 0.8$ mm between them. Pictures of the custom-made x-wire probes are shown in Fig. 2.13. In table 2.1 are summarized the different hot-wire probes used and their parameters. The temperature coefficient of resistance is indicated as α_{el}, it is a property of the material and indicates the relative variation in resistance for a variation of $1°\ C$. The hot-wires are operated in CTA mode via a Dantec Streamline 90N10 frame and 90C10 CTA channels with an overheat ratio $a_w = (R_w - R_0)/R_0 = 1.0$, where R_w is the hot-wire resistance at operating temperature and R_0 is the resistance at reference (ambient) temperature. The resulting operating temperature of Platinum wires is $T_w \approx 260 - 270\ °C$. Sampling frequency is set to 60 kHz with a low pass

filter at 30 kHz for all present measurements. The analog signal is amplified prior to acquisition, done with a National Instruments cRIO 9068 chassis and a NI-9215 Analog Input module.

Probe n.	*Type*	*Material*	$d\ [\mu m]$	$L\ [\mu m]$	L/d	a_w	$\alpha_{el}\ [1/°C]$
1	bl-type	Platinum	5	1000	200	1.0	$3.93 \times 10^{-}3$
2	bl-type	Platinum	2.5	500	200	1.0	$3.93 \times 10^{-}3$
3	bl-type	Platinum	1.2	250	200	1.0	$3.93 \times 10^{-}3$
4	straight	Tungsten	5	1100	220	0.8	$3.60 \times 10^{-}3$
5	x-wire	Platinum	2.5	700	280	1.0	$3.93 \times 10^{-}3$

Table 2.1: Dimensional and physical parameters of the hot-wire probes used for the experimental campaign.

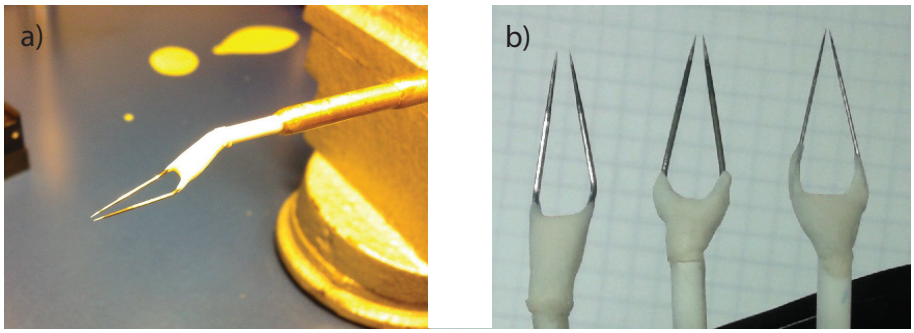

Figure 2.12: a) Example of a boundary-layer type, single wire probe used for the campaign. b) Differently sized probes; from left to right: 1 mm, 0.5 mm and 0.25 mm prongs spacing.

2.3.2. *Hot-wire calibration*

Hot-wire velocity and angular (for x-wire probes) calibration is performed *ex situ* in a Dantec Streamline 90H02 external calibrator jet with a velocity range of $0.5 - 50\ m/s$. During calibration, hot wire voltage E, flow velocity U and flow temperature T are acquired for every calibration point. Flow velocity is retrieved with a Pitot tube measuring in the jet core next to the hot-wire sensor. Temperature of the jet is acquired with a PT100 thermistor. A reference calibration temperature T_{ref} is computed as the mean temperature of calibration points, and voltage of every calibration point is corrected with respect to

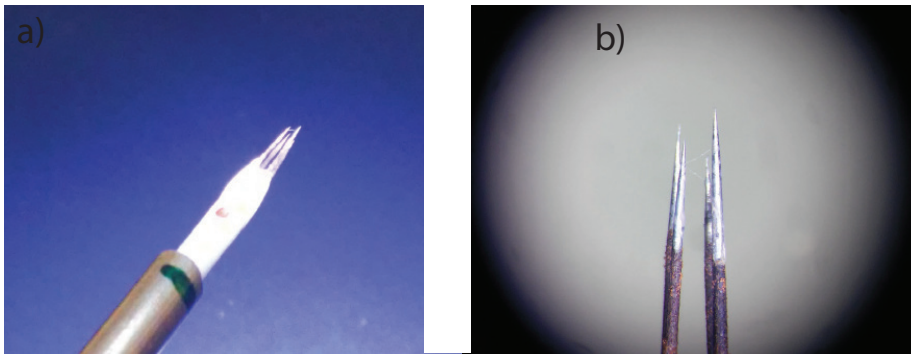

Figure 2.13: a) X-wire probe. b) Close up of the prongs' and wires' configuration.

the point's mean temperature T_i with the following expression (Bruun (1995)):

$$E(T_{ref}) = E(T_i)\left(1 - \frac{T_i - T_{ref}}{a_w/\alpha_{el}}\right)^{-(1/2)} \tag{2.11}$$

For single-wire probes, the calibration procedure consists in acquiring ≈ 20 calibration points spanning the wind tunnel velocity range. A calibration curve is then fitted on data-points in the form of a fourth order polynomial:

$$U = C_0 + C_1 E + C_2 E^2 + C_3 E^3 + C_4 E^4 \tag{2.12}$$

where $C_0 ... C_4$ are determined via least square fitting. An example calibration for a single wire sensor is shown in Fig. 2.14a.

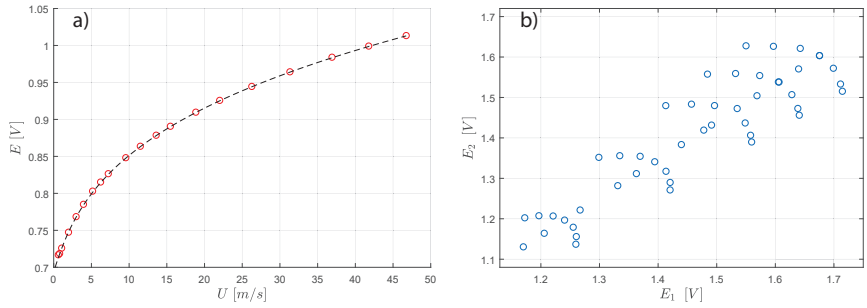

Figure 2.14: a) Calibration curve for a single wire probe. ○; calibration data-points. - -; 4th order polynomial. b) Example of voltage from the two wires acquired during an x-wire calibration.

For x-wire sensors, calibration points involve both a streamwise velocity U_{cal} and a lateral velocity V_{cal}. Lateral velocity is obtained by adjusting the angle between the axis of the probe and the flow. Multiple velocity and angle points are acquired as a part of the calibration, for the present campaign the angle during calibration was varied in a range $\pm 30°$. The way in which voltage from the two wires (E_1, E_2) is associated with instantaneous velocities (U, V) is the *sum and difference* method described in Bruun (1995). According to it, the streamwise and lateral velocity can be found as:

$$U = \frac{U_{1e} + U_{2e}}{2} \tag{2.13}$$

$$V = \beta \, \frac{U_{1e} - U_{2e}}{2} \tag{2.14}$$

where U_{1e} and U_{2e} are called the *effective cooling velocity* of wire 1 and 2, respectively, and β is an angular sensitivity coefficient that is determined through fitting of calibration data-points. It is possible to verify that these relationships follow directly from the Jorgensen law, provided that the angle between the local flow direction and the probe axis is small and that if $V = 0$, $U_{1e} = U_{2e} = U$. The effective cooling velocity U_e sensed by a wire, is the velocity that corresponds to the wire's voltage E when $V = 0$. To retrieve U_e, a calibration curve for each wire is obtained, considering only the calibration points with $V = 0$. This calibration curves can either be polynomials or of another kind and are used to compute the effective velocities (U_{1e}, U_{2e}) from (E_1, E_2). An example of calibration curves for the two wires is shown in Fig. 2.15.

The effective cooling velocity for all calibration data points can then be computed, and the results can be plotted as done Fig. 2.16. From this representation the value of the angular sensitivity coefficient β can be found by linear fitting to the data. During measurements, the instantaneous effective velocity for each wire, (U_{1e}, U_{2e}), can be found with the velocity calibration curves from a couple of instantaneous voltages (E_1, E_2), and finally the instantaneous (U, V) is retrieved using (2.13) and the computed value of β.

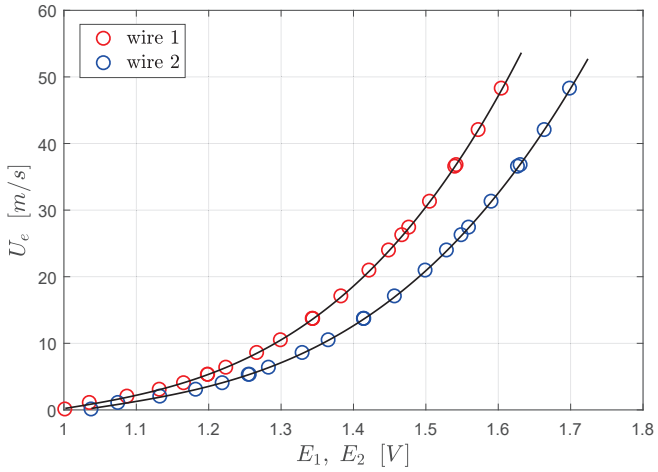

Figure 2.15: Relation between the effective velocity and wire tension E, obtained considering calibration points for which $V = 0$.

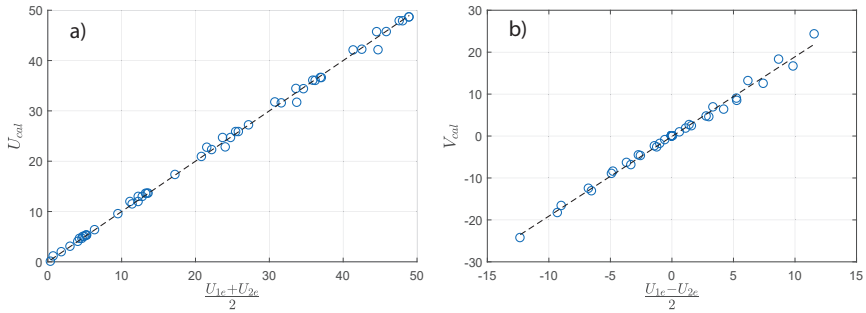

Figure 2.16: Directional calibration curves. —; linear relationships of the sum & difference method. ○; calibration data points. a) Streamwise velocity calibration. b) Lateral velocity calibration.

2.3.3. *Measurement profiles*

While chapter 3 reports results from different experiments characterizing the quality and global quantities of the Long Pipe flow, the bulk of experimental results analysed in chapters 4 and 5 comes from a series of profiles acquired with the single and x-wire sensors previously described. Since this data-set constitutes the main data source of the thesis, here a short description of the

methodology and set-up used will be given, together with a list of all the relevant experimental parameters for these flow-cases. The data was acquired as part of the experimental campaign *Re-Scale*, carried out by a team of the University of Bologna and of the KTH Royal Institute of Technology, and funded through the EuHIT consortium. Some experimental results of the campaign have already been published in Örlü *et al.* (2017).

Hot-wire measurements are performed at $L/D = 123$, in the last 1.5 m long section before the shape converter, for five different Reynolds number cases. Hot-wire probes are mounted on the small traversing shown in Fig. 2.10. Due to the geometrical constraints imposed by the x-wire probes, whose axis must be oriented in the flow direction, the closest obtainable distance from the wall was roughly 3 mm for those type of probes, while in all other cases the wall could be reached. Two different set-ups are used for x-wire profiles: in one the wires are placed in the $x - r$ plane, to measure the streamwise and radial velocity components $U(t)$ and $V(t)$. In the other the wires were placed in the $x - \theta$ plane, thus measuring the streamwise and spanwise components, $U(t)$ and $W(t)$.

During profile measurements, pipe flow temperature is acquired and instantaneous voltage is corrected using (2.11). The heat exchanger of the wind tunnel is regulated to achieve a stable flow temperature as close as possible to the calibration's, in order to minimize the correction applied. Pressure drop and centreline velocity were acquired simultaneously to the profiles and averaged over the entire duration of the profile. No fitting operation is performed on the measured u_τ. Given the fact that a relative encoder is used to record the traversing movements, the absolute wall position is not known *a priori*. To estimate it, the measured mean velocity profile is fitted for $U^+ < 10$ on the analytical expression of the law of the wall given in Chauhan *et al.* (2007). Calibrations are performed before and after each day of the measurement campaign to check for the presence of drift in the sensor's response. Due to sensor drift and wire breakages, different measurement runs had to be aborted or discarded and could not be repeated for time constraints, resulting in the fact that not every Reynolds number case was measured for each of the sensors used. There are however, more than enough datasets to analyse both the Reynolds number scaling and the effects of spatial filtering for different wire lengths. All data-sets acquired are summarized in table 2.2 together with the symbols that are going to be used in the text, unless differently specified.

probe	$L\ [\mu m]$	$d\ [\mu m]$	L/d	$U_{cl}\ [m/s]$	$u_\tau\ [m/s]$	Re_τ	$l_*\ [\mu m]$	L^+	$T\ [s]$	TU_{cl}/R	$f\ [kHz]$	*symbol*
3	250	1.25	200	6.38	0.226	6699	67.2	3.72	160	2265	60	◊
3	250	1.25	200	15.02	0.502	14768	30.5	8.19	140	4668	60	◊
3	250	1.25	200	24.27	0.786	22892	19.7	12.7	120	6464	60	◊
3	250	1.25	200	33.59	1.064	30969	14.5	17.2	100	7456	60	◊
3	250	1.25	200	41.37	1.294	37558	12.0	20.8	100	7346	60	◊
2	500	2.5	200	6.25	0.224	6510	69.2	7.2	160	2220	60	×
2	500	2.5	200	14.49	0.487	14458	31.2	16.0	140	4503	60	×
1	1000	5	200	14.62	0.490	14369	31.3	31.9	140	4544	60	○
1	1000	5	200	23.40	0.759	22220	20.3	49.3	120	6234	60	○
4	1100	5	220	24.25	.785	23049	19.5	56.3	120	6459	60	□
4	1100	5	220	33.58	1.063	31086	14.5	75.9	100	7455	60	□
5 (U-V)	700	2.5	280	6.31	0.222	6546	68.8	10.2	160	2240	60	▽
5 (U-V)	700	2.5	280	15.03	0.503	14696	30.6	22.8	140	4669	60	▽
5 (U-V)	700	2.5	280	24.22	0.782	22768	19.8	35.4	120	6452	60	▽
5 (U-V)	700	2.5	280	33.65	1.065	31184	14.5	48.4	100	7470	60	▽
5 (U-V)	700	2.5	280	41.45	1.294	37872	11.9	58.8	80	7361	60	▽
5 (U-W)	700	2.5	280	6.36	0.226	6649	67.7	10.3	160	2259	60	*
5 (U-W)	700	2.5	280	15.01	0.503	14697	30.6	22.8	140	4665	60	*
5 (U-W)	700	2.5	280	24.21	0.784	22603	19.9	35.1	120	6448	60	*
5 (U-W)	700	2.5	280	33.56	1.063	30692	14.7	47.7	100	7450	60	*
5 (U-W)	700	2.5	280	41.36	1.292	37311	12.1	58.0	80	7345	60	*

Table 2.2: Experimental parameters for the profiles measured as a part of this experimental campaign. Probe numbers in the first column refer to those reported in table 2.1.

CHAPTER 3

Flow in the Long Pipe

In order to characterize the Long Pipe facility, and ensure the stability and canonical condition of the flow, measurements involving static pressure taps, Pitot tube, Prandtl tube and hot-wire anemometry are carried out at different flow regimes, up to a friction Reynolds number of approximately $Re_\tau = 4 \times 10^4$. This chapter presents experimental results related to pressure drop, integral quantities and flow symmetry and stability.

3.1. Pressure drop

In the Long Pipe facility the wall shear stress τ_w (and hence the friction velocity u_τ) is measured indirectly via pressure drop along the pipe. In fact for a pipe flow, the equilibrium of forces acting on a volume of fluid contained in a pipe section of length dx is:

$$dp\pi R^2 = \tau_w 2\pi R dx \tag{3.1}$$

which yields:

$$\tau_w = \frac{dp}{dx}\frac{R}{2} \tag{3.2}$$

this directly links the pressure gradient and the wall friction. From τ_w, the friction velocity $u_\tau = \sqrt{\tau_w/\rho}$ can be computed which, according to classical wall-turbulence theory, is the relevant velocity scale both in the inner and in the outer region of the flow. For this reason estimating the pressure drop with accuracy is of great importance to obtain accurate normalized statistics; Örlü *et al.* (2010) shows the effect that an error on the estimated u_τ has on the inner-scaled mean velocity profile. Static pressure measurements are taken along the pipe from the test section up to $\approx 70\ m$ upstream, using wall pressure taps with a diameter of 1 mm. Measurements are performed at different flow regimes, that are achieved by varying the rotational speed of one axial fan of the facility, while the other was left free-running. Meanwhile, the mean flow centreline speed U_{cl}, the ambient pressure p_{amb} and the temperature were monitored in the test section. Difference between ambient pressure outside the pipe and mean static pressure measured in the pipe is shown in Fig. 3.1 for different Re_τ values as a function of the axial coordinate x, where $x = 0\ m$ corresponds to the exit of the convergent. The test section is located at $x \approx 110\ m$.

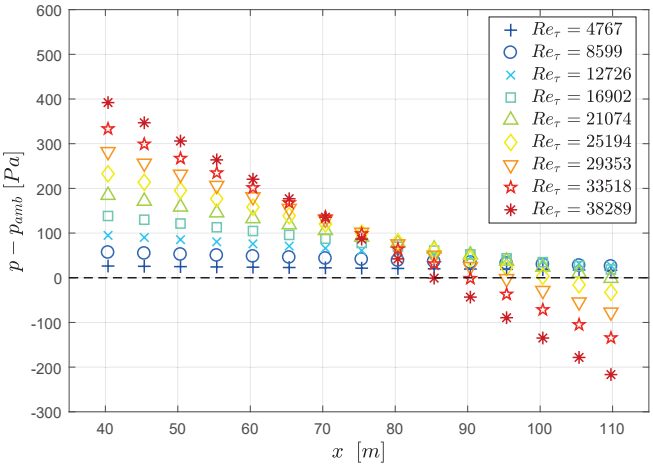

Figure 3.1: Differential pressure measured in the pipe, using outside ambient pressure as reference, for a range of Reynolds numbers. The black dashed line indicates the ambient pressure outside the pipe p_{amb}.

From the figure, a qualitative linear trend can be seen at all Re_τ cases, without any obvious deviation from it. One can notice that, by increasing the wind tunnel speed, an under-pressure with respect to outside ambient develops in the test section, that reaches $\approx -200\ Pa$ for the highest Reynolds number examined here. This however, doesn't seem to affect the linearity of the pressure drop.

3.1.1. *Extent of the linear fit*

As the pressure drop for a turbulent pipe flow is linear, the obvious way to compute it is by fitting a line to the experimental data points. An important factor to determine is the number of data points to use, i.e. the length over which the linear fit is applied. In principle it is desirable to measure the dp/dx (and get the u_τ) at the point where the measurements are taken, since pressure drop becomes constant only for a fully developed pipe flow, and there could still be some residual flow development effect far from the test section. On the other hand, the more points are used for the linear fit, the less sensitive the measure of dp/dx becomes to bias errors introduced by single pressure taps. These deviations could be caused by small imperfections in the wall taps. To decide the number of pressure taps to be used in the fit, different linear fits were computed from the pressure data set of Fig. 3.1, starting from the test section and using an increasing number of upstream pressure taps. To evaluate the quality of the different fits, the error can be computed, which is the difference

between the pressure data and the value of the linear fit at the same axial location:

$$p_e(x) = p_{data}(x) - p_{fit}(x) \tag{3.3}$$

Then the standard deviation of the error σ_{p_e} can be computed over the data points used for the fit. In Fig. 3.2, σ_{p_e} is plotted against the number of pressure taps used for the fit, while in figure 3.3 the same quantity is normalized by a reference value for τ_w, taken as the friction velocity resulting from fitting all the points.

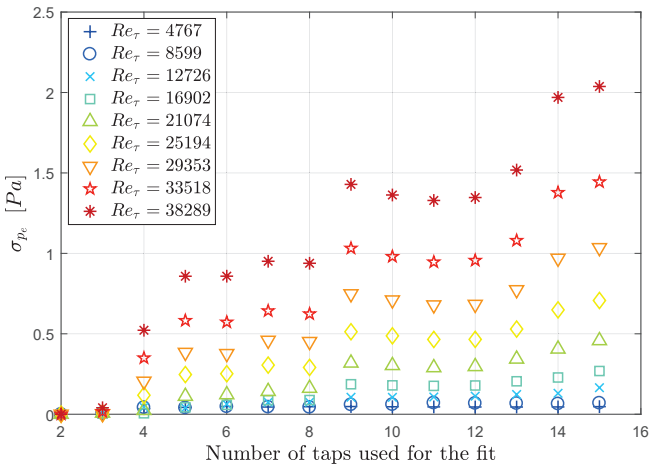

Figure 3.2: Standard deviation σ_{p_e} of the pressure error defined in equation 3.3, plotted against the number of taps used for the linear fit, with the first one always being the one closest to the test section.

As can be seen from Fig. 3.3 and 3.2, the absolute value of σ_{p_e} increases as more points are added to the fit (starting from 2 taps where it has to be mathematically zero), and is higher for high Re_τ cases. Although, as can be seen in Fig. 3.3, when normalized by a reference value of the friction velocity (the one resulting from using all the points in the fit), it becomes far more relevant for low Re_τ. It can also be noticed how there is a discontinuity and a sharp increase in σ_{p_e} in correspondence of the fourth and ninth tap, possibly pointing out a systematic deviation from the fit in those positions. From the standard deviation of the error of the fit, the 95 % confidence interval for the slope a of the linear regression $y = ax + b$ can be calculated; for a distribution of n points with coordinates (x_i, y_i):

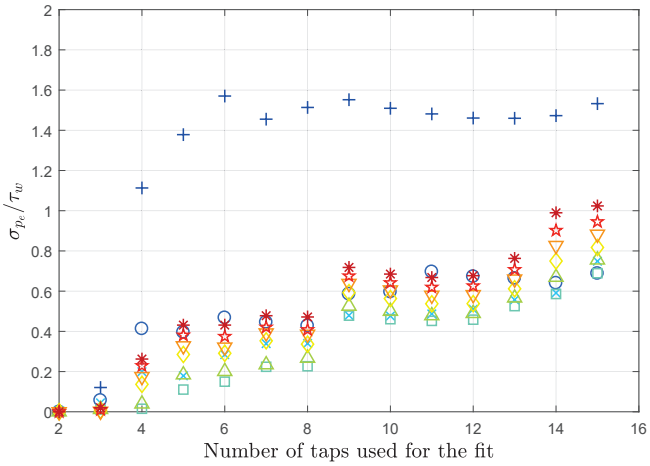

Figure 3.3: Standard deviation σ_{p_e} of the pressure error defined in equation 3.3 normalized by the value of the wall shear stress tau_w, plotted against the number of taps used for the linear fit, with the first one always being the one closest to the test section.

$$95\%\ CI_a = \sqrt{\frac{\sum(y_i - ax_i - b)^2}{n-2}} \times \sqrt{\frac{n}{n\sum x_i^2 - (\sum x_i)^2}} \tag{3.4}$$

The 95 % confidence interval for the slope of the fitted line is reported in figure 3.4. It must be noted that the one computed here is just the uncertainty of the fit, and not the total uncertainty on the determination of dp/dx. A more complete estimate of the uncertainty on u_τ and its effects on the measured statistics is given in appendix A. Despite the slight increase in σ_{p_e}, the uncertainty on the pressure gradient drops as more points are added to the fit, with a notable exception being when 3 taps are used. Also adding more taps after the 8th, doesn't seem to improve substantially the uncertainty for most Reynolds number cases. Based on these observations, It was decided to use the last 8 pressure taps for the computation of the pressure gradient, corresponding to a length of 40 meters.

In figure 3.5 is reported the mean pressure measured for all the taps together with the linear fits computed using the points previously described. To evaluate the linearity of the pressure drop, In figure 3.6 the pressure error p_e at every tap is shown, from the least square linear fit obtained using the selected 8 pressure taps. From this plot a deviation towards negative values of the pressure error p_e can be seen in the 4-5 taps farther away from the test section.

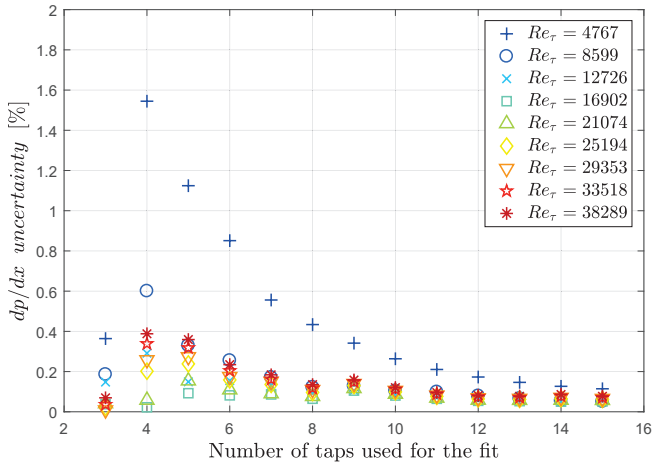

Figure 3.4: 95 % confidence intervals on dp/dx (plotted in percentage) as a result of the pressure errors on the linear fits, as a function of the number of taps used for the linear fit, with the first one always being the one closest to the test section.

This corresponds to a slight undershoot of the static pressure with respect to the linear fit, and is likely caused by residual flow development at those axial coordinates ($x = 40\ m$ corresponds to $x/D \approx 44$). What is important to notice in Fig. 3.6 is that within the region used for the linear fit no trend is noticeable and the points appear scattered around zero, with an error that for $Re_\tau > 1.3 \times 10^4$ is $-\tau_w < p_e < \tau_w$. In table 3.1 the measured pressure drop and friction velocities are reported for all the Reynolds number investigated.

3.2. Skin friction relation

After deriving the pressure gradient as described in the previous section, the wall shear stress can be computed using equation 3.2, and so can the friction velocity:

$$u_\tau = \sqrt{\frac{\tau_w}{\rho}} \tag{3.5}$$

From that, the friction Reynolds number Re_τ can be calculated:

$$Re_\tau = \frac{u_\tau R}{\nu} \tag{3.6}$$

Re_τ	$U_{cl}\ [m/s]$	$dp/dx\ [Pa/m]$	$dp/dx\ \ error$	$u_\tau\ [m/s]$	$u_\tau\ error$	$\ell_*\ [\mu m]$
2.99×10^3	2.40	0.054	± 0.78 %	0.102	± 0.39 %	151
4.77×10^3	4.39	0.137	± 0.43 %	0.161	± 0.22 %	95.0
6.64×10^3	6.32	0.266	± 0.26 %	0.225	± 0.13 %	68.1
8.60×10^3	8.40	0.447	± 0.12 %	0.292	± 0.06 %	52.5
10.66×10^3	10.55	0.685	± 0.12 %	0.361	± 0.06 %	42.4
12.73×10^3	12.80	0.978	± 0.10 %	0.432	± 0.05 %	35.5
14.80×10^3	15.10	1.326	± 0.08 %	0.503	± 0.04 %	30.5
16.90×10^3	17.41	1.731	± 0.06 %	0.575	± 0.03 %	26.7
19.00×10^3	19.75	2.184	± 0.09 %	0.645	± 0.04 %	23.8
21.07×10^3	22.07	2.689	± 0.08 %	0.716	± 0.04 %	21.4
23.17×10^3	24.41	3.244	± 0.10 %	0.787	± 0.05 %	19.5
25.19×10^3	26.74	3.841	± 0.10 %	0.856	± 0.05 %	17.9
27.27×10^3	29.09	4.498	± 0.10 %	0.926	± 0.05 %	16.6
29.35×10^3	31.44	5.205	± 0.11 %	0.996	± 0.06 %	15.4
31.41×10^3	33.82	5.964	± 0.11 %	1.066	± 0.06 %	14.4
33.52×10^3	36.22	6.783	± 0.12 %	1.137	± 0.06 %	13.5
35.57×10^3	38.60	7.642	± 0.13 %	1.207	± 0.06 %	12.7
38.29×10^3	41.66	8.834	± 0.13 %	1.297	± 0.07 %	11.8

Table 3.1: Experimental parameters for the characterization of the Long Pipe facility.

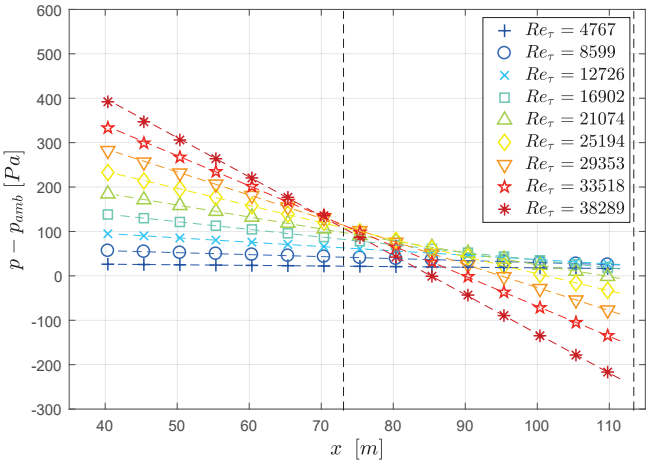

Figure 3.5: Differential pressure measured in the pipe, using outside ambient pressure as reference, for a range of Reynolds numbers. The dashed lines represent the linear fit obtained by least square, using the data from the last 40 meters of the pipe, the vertical lines represent the region of the pipe used for the linear fit.

By summing term-by-term eq. (1.65) and (1.66), respectively the logarithmic law of the wall in inner units and the velocity-defect law; the so-called skin friction relation can be obtained:

$$U_{cl}^{+} = \frac{1}{\kappa}\, ln(Re_\tau) + B^* \tag{3.7}$$

Where $B^* = B + C$ is the sum of the additive terms B and C that appear in eq. (1.65) and (1.66). Equation (3.7) links directly the value of the Von Kárman constant to a measure of the centreline velocity and the pressure gradient. In order to compare the results with the Superpipe facility, the expression given in McKeon *et al.* (2005) for their Superpipe measurements can be used:

$$U_{cl}^{+} = 2\sqrt{2}(D_1 log(Re_D\sqrt{\lambda}) + D_2) \tag{3.8}$$

Where Re_D is the Reynolds number based on the bulk velocity U_b and the pipe diameter D, and λ is the friction factor:

$$Re_D = \frac{U_b D}{\nu} \tag{3.9}$$

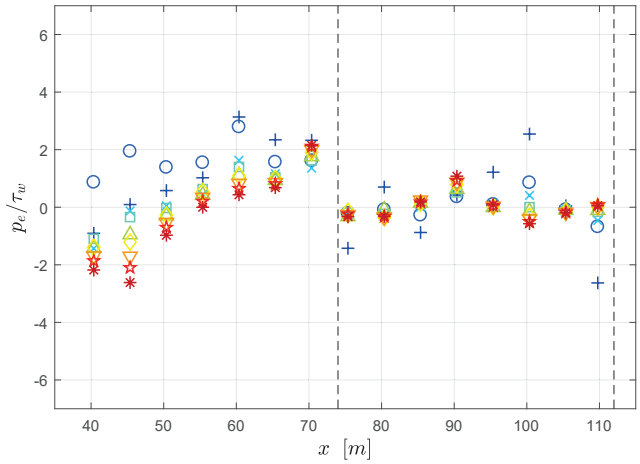

Figure 3.6: Error between the measured pressure at every tap and the linear fit shown in fig 3.5, normalized by the wall friction. The vertical lines represent the region of the pipe used for the linear fit.

$$\lambda = 8\left(\frac{u_\tau}{U_b}\right)^2 \tag{3.10}$$

While D_1 and D_2 are two constants

$$D_1 = \frac{1}{2\kappa\sqrt{2}log(e)} \tag{3.11}$$

$$D_2 = \frac{B+B^*}{2\sqrt{2}} - \frac{1}{\kappa}\left[\frac{log(4\sqrt{2})}{2\sqrt{2}log(e)}\right] \tag{3.12}$$

It can be shown how the reported expression in eq. (3.8) is equal to the skin friction relation in eq. (3.7). Indeed, by replacing expressions (3.9), (3.10), (3.11), and (3.12) into (3.8); we obtain an expression for the normalized centreline velocity as a function of the Von Kárman constant κ, the friction Reynolds number Re_τ and the constants B and B^*:

$$U_{cl}^+ = \frac{1}{\kappa}ln(Re_\tau) + B + B^* \tag{3.13}$$

Using the values of $D_1 = 1.934$ and $D_2 = 0.958$ given by McKeon *et al.* (2005) and substituting in (3.8), the following relation representing Superpipe data is obtained:

$$U_{cl}^{+} = 5.470 log(Re_{\tau}) + 6.826 \tag{3.14}$$

which corresponds to a value of the Von Kármán constant $\kappa \approx 0.421$. To check for anomalies in the values of dp/dx, u_{τ} and U_{cl} measured in CICLoPE, the normalized Superpipe expression (3.14) can be used to compute the respective centreline velocity, pressure gradient and friction velocity for a range of Reynolds number, using the CICLoPE pipe radius ($R = 0.45m$) and measured ambient quantities, to make a comparison between dimensional data. In figure 3.7 and 3.8 the pressure gradient and the friction velocity are reported, while in figure 3.9 the normalized centreline velocity is plotted against the Reynolds number for the CICLoPE measurements, together with expression (3.14) for comparison.

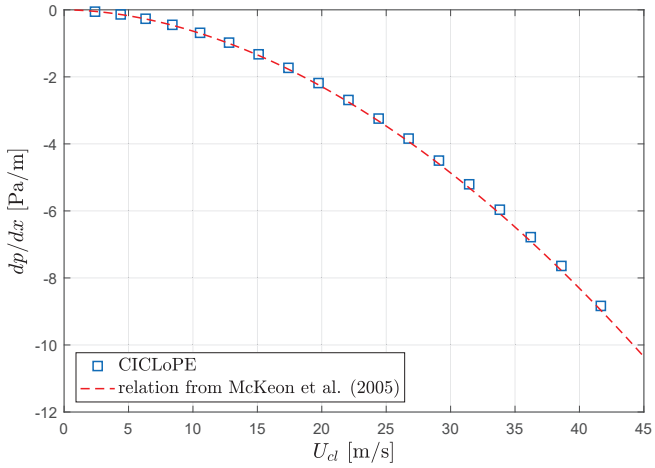

Figure 3.7: Pressure gradient plotted against centreline velocity measured with a Prandtl tube in the long Pipe. The dashed curve corresponds to the values that are obtainable from the Superpipe relation (3.14), using a pipe radius R equal to that of the Long Pipe. Errorbars resulting from uncertainty in dp/dx (see table 3.1) are omitted because are one order of magnitude smaller than the marker size.

In Fig. 3.9 are reported the values of the inner-normalized centreline velocity as a function of the friction Reynolds number. The data appear to collapse on a logarithmic trend at high Reynolds number, while there is a noticeable deviation at lower Reynolds numbers, that could be caused by increased uncertainty on u_{τ} estimation at lower velocities (note that both Re_{τ} and U_{cl}^{+} are

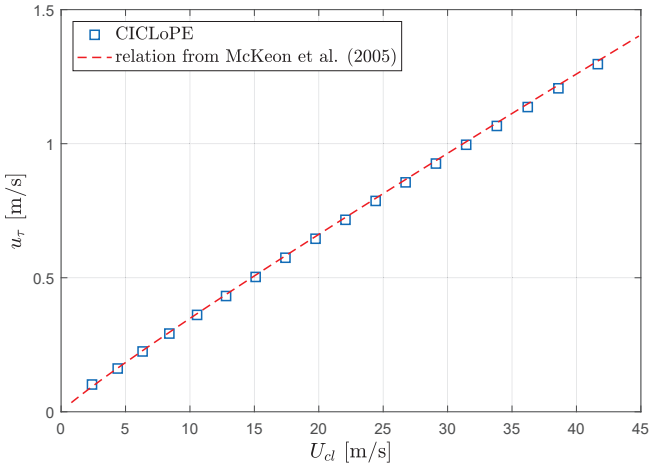

Figure 3.8: Friction velocity u_τ plotted against centreline velocity measured with a Prandtl tube in the long Pipe. The dashed curve corresponds to the values that are obtainable from the Superpipe relation (3.14), using a pipe radius R equal to that of the Long Pipe. Errorbars resulting from uncertainty in u_τ (see table 3.1) are omitted because are one order of magnitude smaller than the marker size.

functions of u_τ). By fitting data points on expression (3.15) and considering only data points for $Re_\tau > 10^4$ the following relation is obtained:

$$U_{cl}^+ = \frac{1}{0.437}\, ln(Re_\tau) + 8.062 \tag{3.15}$$

at $\kappa = 0.437$, the value of the von Kármán constant calculated with this method is considerably higher than the value that will be obtained later by fitting the log law of the mean velocity profiles. Although it should be remembered that the sensitivity of the errors on u_τ in this type of plot is rather high, it doesn't fully explain the difference observed here.

3.2.1. *Friction factor and bulk velocity*

For a fully developed turbulent pipe flow, the friction factor λ is defined by eq. (3.10). It can be shown that the friction factor is a unique function of the bulk Reynolds number Re_D. If we consider that the bulk velocity is the result of an integration of the profile of the mean velocity $\overline{U}$, by manipulating (3.10), it is possible to obtain the following:

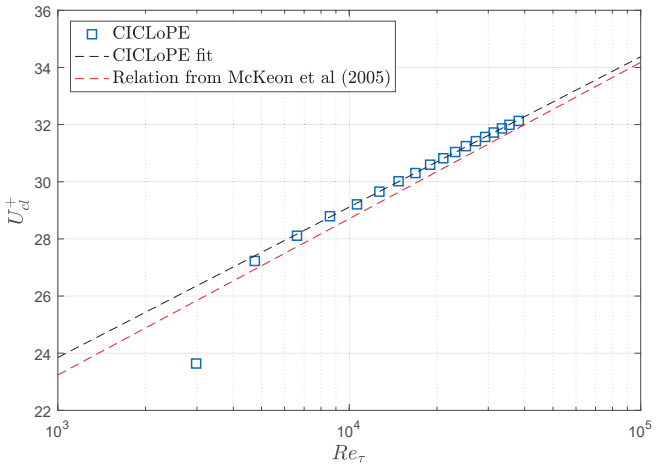

Figure 3.9: Inner-normalized centreline velocity as a function of friction Reynolds number. ––; CICLoPE data point fit for $Re_\tau > 10^4$. ––; Superpipe data fit from McKeon *et al.* (2005)

$$\sqrt{\frac{8}{\lambda}} = \frac{U_b}{u_\tau} = 2\int_0^1 U^+ \left(1 - \frac{y^+}{R^+}\right) d\left(\frac{y^+}{R^+}\right) \tag{3.16}$$

Which clearly shows how the friction factor is related to the shape of the mean velocity profile. Making the assumption that the mean velocity profiles follows the log law: $U^+ = (1/\kappa)\, ln(y^+) + B$, and resolving the integral, the following expression can be obtained:

$$\frac{1}{\sqrt{\lambda}} = \frac{1}{2\kappa\sqrt{2}}\, log(Re_D\sqrt{\lambda}) + C - D(Re_D) \tag{3.17}$$

Where C is a constant that accounts for the deviation of the mean profile from the log law in the core region (constant because U^+ is a function of y/R), and D is a coefficient that accounts for a similar deviation in the viscous and buffer region, and is generally dependent on Re. Prandtl, based on 1932 Nikuradse pipe data and neglecting the contribution of the viscous and buffer layers in the integral, derived:

$$\frac{1}{\sqrt{\lambda}} = 2.0\, log(Re_D\sqrt{\lambda}) - 0.8 \tag{3.18}$$

That is commonly known as the Prandtl equation. Since in eq. (3.17) the von Kárman constant κ appears, the expression can also be used to find κ with a

fitting procedure on experimental data of Re_D and λ. Both these quantities however rely on an estimation of the bulk velocity U_b. Here with a simple experimental set-up and some simplifying assumptions we use two different methods to get an estimate of U_b. In a separate experiment than the one previously described, two static pressure taps at the entry and exit section of the convergent were drilled, together with an opening that allowed a Prandtl tube to be placed on the centreline at the exit section of the convergent. By using static pressure taps before and after the convergent, and employing Bernoulli's theorem, valid for incompressible and irrotational flow, the following relation can be written:

$$p_1 + \frac{1}{2}\rho V_1^2 = p_2 + \frac{1}{2}\rho V_2^2 \tag{3.19}$$

Where subscript 1 and 2 denote respectively the entrance and exit section from the convergent, p_1 and p_2 are the static pressure and V_1 and V_2 are the mean velocities on the sections. Since the two sections must have the same mass flow and we assume the fluid to be incompressible:

$$\frac{V_1}{V_2} = \frac{A_2}{A_1} \tag{3.20}$$

For the Long pipe in CICLoPE the convergent section has a contraction ratio $CR = 4$, which means that $V_1 = (1/4)\ V_2$. Substituting this into (3.19), we obtain:

$$V_2 = \sqrt{\frac{32(p_1 - p_2)}{15\ \rho}} \tag{3.21}$$

Considering that V_2 is the mean velocity in section 2, for mass conservation considerations it effectively corresponds to the bulk velocity U_b in the test section. This estimate of U_b can be used to compute the bulk Reynolds number Re_D and the friction factor λ. Another way to estimate U_b is by measuring the mean velocity at the exit of the convergent. If we make the additional assumption that at the exit of the convergent section the velocity profile is flat ($\overline{U}$ constant for every point in the section) which is a good assumption for the flow after the screens and convergent. In fact there should be an almost uniform profile, with the boundary layer extremely thin and just starting to develop near the wall. In this case, the measured mean velocity $\overline{U}$ with a Prandtl tube at the exit of the convergent and near the centreline, was taken as the bulk velocity U_b. In Fig. 3.10 the computed values of the friction coefficient using the two methods described are plotted against Re_D and compared with Prandtl's relation (3.18) and measurements reported by McKeon *et al.* (2005) in the Superpipe. The Superpipe data used is based on Zagarola & Smits (1998) measurements with the correction reported by Mckeon *et al.* (2004) applied to

it. The results reported by Furuichi *et al.* (2015) from the Hi-Reff water pipe facility in Japan are also displayed. It should be noted that the simplified methods used here to estimate U_b have inherently larger uncertainties than both the profile integration used by McKeon *et al.* (2005) or the flow rate measurement by Furuichi *et al.* (2015). It is, however, beyond the scope of this simple analysis to establish a friction factor relationship, rather the aim is to characterize the facility and provide all the available data. Nonetheless, the data shown in Fig. 3.10 displays a remarkable agreement both between the two methods used here to estimate U_b and with the literature data.

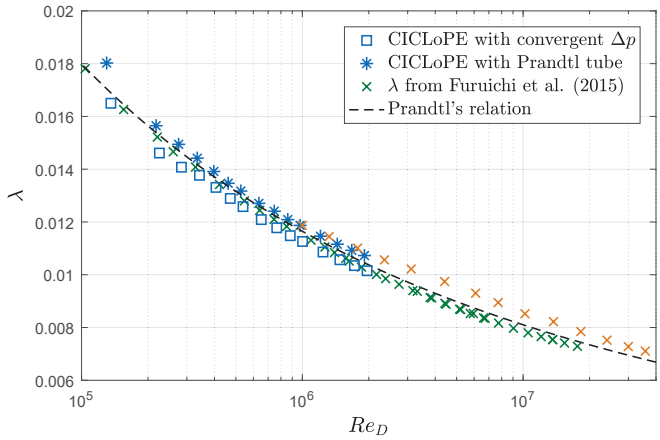

Figure 3.10: Friction factor as a function of the bulk Reynolds number. Black dashed line represent Prandtl's expression reported in eq. (3.18).

3.3. Flow development

In a different experiment from the centre-line Prandtl tube and pressure drop measurements presented previously, a single hot wire was mounted on the global traversing device (see Fig. 2.11) and positioned on the pipe centre-line, where acquisition was performed for different speed cases. For this set-up, hot-wire calibration is not performed separately before the acquisition, but *in situ* at the same time as measurements are taken. *A posteriori*, a calibration curve is obtained using for each speed case the mean velocity reading from the pitot tube and the mean hot-wire voltage. Hot-wire velocity timeseries acquired at different Re_τ values are used to compute statistical moments up to the fourth order and the power spectral density $\Phi_{uu}(k)$. In Fig. 3.12 the normalized power spectral density of the streamwise velocity is shown as a function of streamwise wavenumber k_x inferred using the frozen turbulence hypothesis by Taylor

(1938), $k_x = 2\pi f/U_{cl}$. The streamwise wavenumber was from the timeserie of velocity and the local mean velocity U_{cl} as the convective velocity of the waves. Normalization is done with the mean dissipation rate ϵ and the Kolmogorov scale $\eta_k = (\nu^3/\epsilon)^{1/4}$. The dissipation rate is estimated by making the hypothesis of homogeneous and isotropic turbulence and integrating the dissipation spectrum:

$$\epsilon = 15\nu \int_0^\infty k_x^2 \Phi_{uu}(k_x)\, dk_x$$

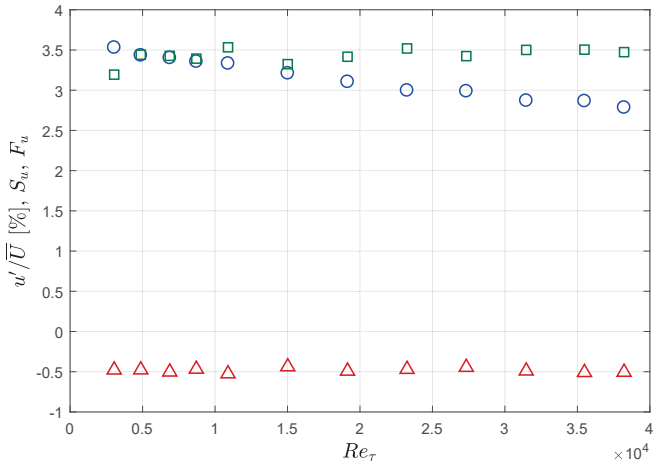

Figure 3.11: Turbulence Intensity, Skewness and Flatness factor plotted against the Friction Reynolds number.

This procedure has been shown by Bailey *et al.* (2009) to yield accurate results in the almost-isotropic pipe centerline.

To check that the flow has reached a fully developed state (at least with regards to the mean velocity) in the test section, a Pitot tube with an inner diameter of 0.5 mm was mounted on the small traversing and together with the static pressure from a tap placed at the same axial coordinate, mean velocity profiles were taken at three different axial stations: $L/D = 123$ (which corresponds to the test section), $L/D = 121$ and $L/D = 116$, for one Reynolds number case corresponding to $Re_\tau = 2 \times 10^4$. The assembly of the Pitot tube and holder prevents the probe to come closer than ≈ 4 mm from the wall. hence only data points in the overlap and core region are available. Data is reported in Fig. 3.13 in semi-log sand linear scaling. The data is shown together with a reference log-law. No significant deviation between the three data-sets

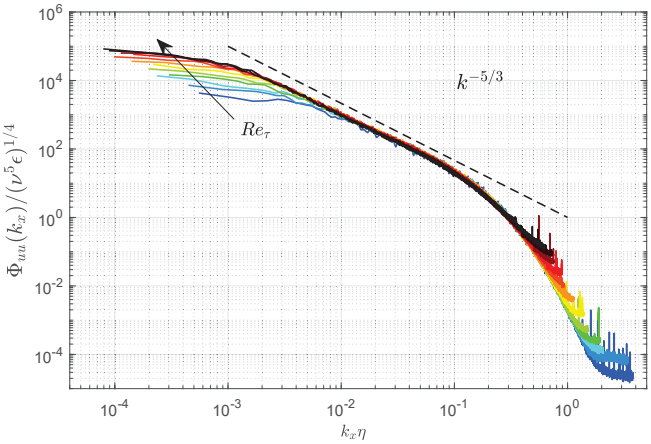

Figure 3.12: Normalized Power spectral densities in the pipe centreline.

can be observed; so no development on the mean velocity profile takes place in the last part of the pipe and more importantly no upstream effect is present on the very last section ($L/D = 123$) from the shape converter and diffuser that follow it.

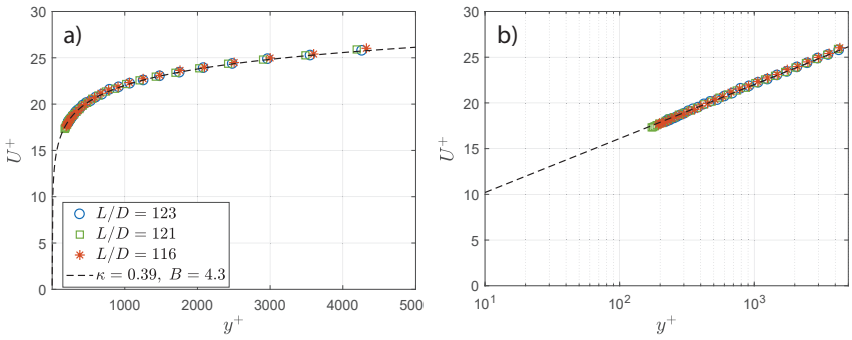

Figure 3.13: Inner normalized mean velocity from Pitot tube measurements at different L/D stations, as a function of wall distance in inner units, in: a) linear scale. b) logarithmic scale. The log-law coefficients are only for reference.

3.4. Flow simmetry

Additional measurements were performed with a Pitot total pressure probe mounted on the global traversing device, resulting in a symmetrical blockage effect. This set-up allows to check the axial symmetry of the flow. Static pressure is acquired from a tap on the wall at the same axial location. The probe is traversed from one side of the pipe to the other with uniform step sizes, for 3 different Reynolds number cases, profiles are shown if figure 3.14. By using this set-up it is impossible to perform measurements very close to the wall but it is still possible to check the symmetry of the flow for the overlap and core region of the pipe.

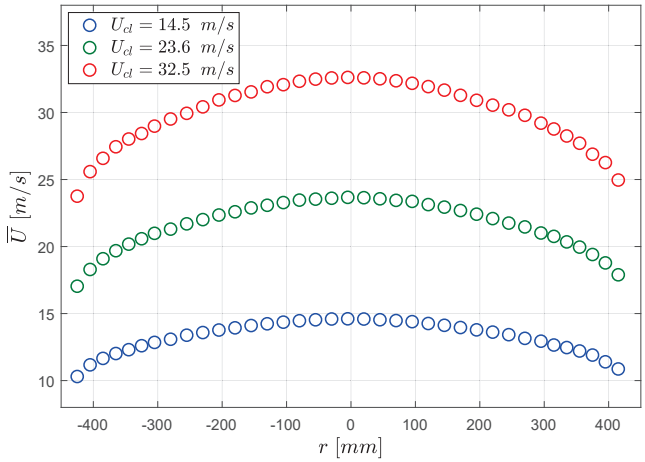

Figure 3.14: Dimensional velocity profiles

After the measurements were taken, the location of the maximum of the velocity were found by fitting a third order polynomial function to all three profiles. Taking this location as the centreline of the flow ($r = 0$), the mean velocity data points can be plotted as a function of $|r/R|$, therefore making a comparison between the two sides of the velocity profile. Dimensional profiles plotted in this way are shown in Fig. 3.15, while normalized velocity profiles are shown in Fig. 3.16. From the figures, no deviation from the axial symmetry is detectable for all the speed investigated, that span the operational range of the facility.

3.5. Flow Stability

In this section the wind tunnel stability in terms of mean flow speed and temperature will be assessed. The data used are the temperature and centreline

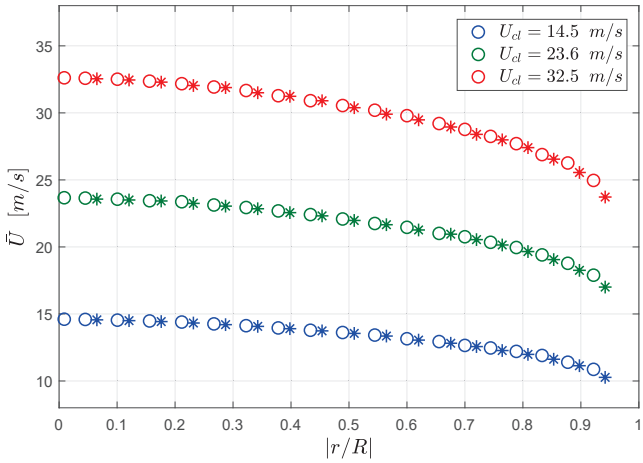

Figure 3.15: Dimensional velocity profiles, mirrored around the centreline found with the fitting procedure described in 3.4. Asterisks corresponds to negative values of the coordinate r, while circles corresponds to positive values.

velocity timeserie measured respectively with a Prandtl tube and a pt100 thermistor during the pressure drop characterization measurements presented in section 3.1. Five velocity cases are analysed, spanning the operative range of the Long Pipe. In Fig. 3.17 are reported the temperature timeserie $T(t)$ over their total duration of 300 seconds, acquired with a freqency $f_a = 1\ Hz$, with the respective mean $\overline{T}$ subtracted. As shown in the figure, the heat-exchanger is able to maintain a constant temperature within $\pm 0.05\ ^\circ C$ up to the highest flow velocity case, corresponding to $Re_\tau \approx 3.8 \times 10^4$.

The centreline velocity measured with the Prandtl tube is shown in Fig. 3.18. The aim is to verify the absence of trends or drift in the value of mean centreline velocity $\overline{U}_{cl}$, without considering the natural velocity fluctuations produced by turbulence. For this reason a simple moving average is applied to the data, and the averaged value is referred to as $\widetilde{U}_{cl}(t)$. The number of seconds over which the moving average is applied is different for every case and equal to $500\ R/\overline{U}_c l$, to take into account the different characteristic time-scales of each flow case. all speed cases show a stable moving average, with no discernible trends around the mean value $\overline{U}_{cl}$.

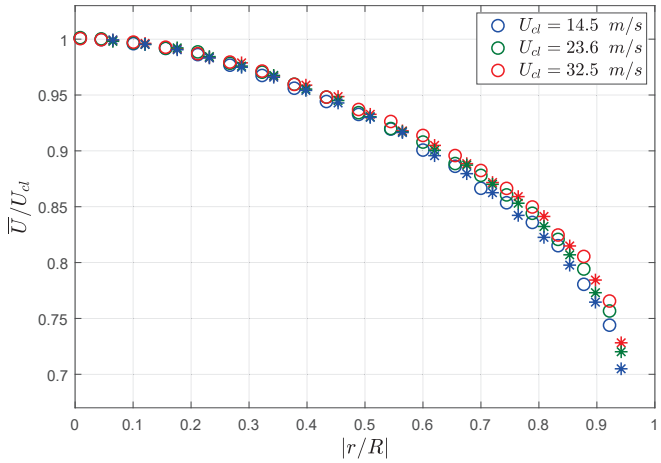

Figure 3.16: Normalized velocity profiles, mirrored around the centreline found with the fitting procedure described in 3.4. Asterisks corresponds to negative values of the coordinate r, while circles corresponds to positive values.

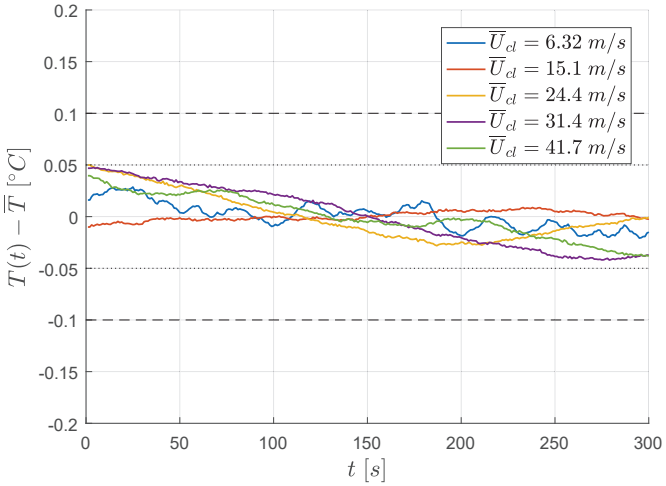

Figure 3.17: Istantaneous temperature fluctuations as a function of time for five flow cases. $\cdot\cdot$; $\pm 0.05\ ^\circ C$ $--$; $\pm 0.1\ ^\circ C$.

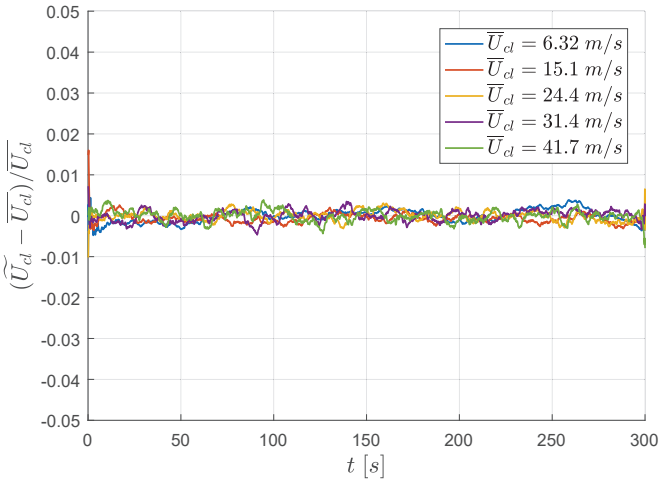

Figure 3.18: Relative variation of the moving average of centreline velocity $\widetilde{U}_{cl(t)}$ with respect to the mean value $\overline{U}_{cl}$, for five flow cases.

CHAPTER 4

Turbulence statistics

In this chapter Pipe Flow statistics from single and x-wire measurements will be analysed, with a particular focus on the scaling of turbulent fluctuations and Reynolds stresses. The set-up and methodology used is reported at the end of chapter 2.

4.1. Mean velocity

The normalized mean velocity profiles are shown in the classical logarithmic inner-scaling in Fig. 4.1 for all Reynolds number cases. The agreement is satisfactory, with a small noticeable deviation in the lowest Reynolds number case, that can be explained with a combination of higher uncertainty on u_τ estimation and the difficulty in providing enough calibration points at the lower velocity range. In appendix A the effects of these uncertainties on the measured statistics are explored in detail. In Fig. 4.2 the profiles are reported in linear scaling, while in Fig. 4.3 is shown the velocity defect $U_{cl} - \overline{U}$ normalized with the friction velocity and presented in outer scaling.

For the determination of the log-law coefficients, different methods can be employed. The most direct one applies a least-square fit of a log law on a measured velocity profile. The boundaries of the logarithmic region are assumed to be $0.15\ R < y < 200\ l_*$. Calculating κ in this way results in a large fit uncertainty, in particular for the lower velocity range where statistical convergence is more problematic and the number of data points that fall within the assumed log-region range is limited. The fitted κ resulting from this procedure are shown in Fig. 4.5 with error-bars representing the fit uncertainty. On the same figure are shown the results obtained with the same method by Bailey *et al.* (2014) in the Princeton Superpipe. Despite the large uncertainty on the fit, particularly at lower Re_τ values, that doesn't allow to make definitive conclusion on Reynolds number behaviour of the coefficient, a remarkable agreement with the Superpipe data-sets can be observed. In order to lower the uncertainty of the fit, after discarding the case at $Re_\tau = 6.5 \times 10^3$, all mean velocity profiles can be used together for the fit (shown in Figure 4.6), yielding a log law with the coefficients:

$$\overline{U}^+ = \frac{1}{0.399}\, ln\, y^+ + 4.50 \tag{4.1}$$

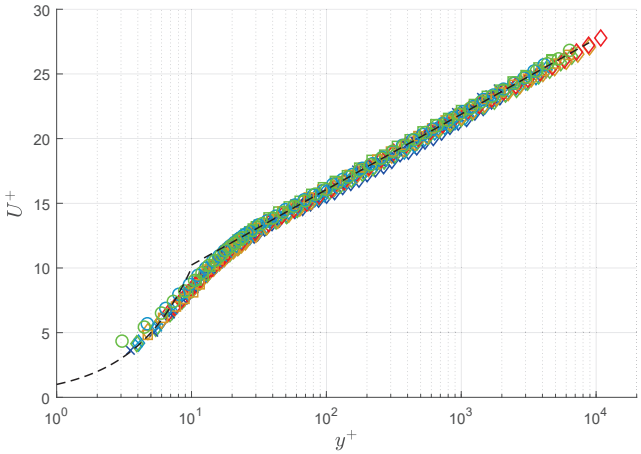

Figure 4.1: Normalized mean velocity profiles for all data-sets in table 2.2; the values of log-law coefficients shown for reference in the figure as a black dashed line are $\kappa = 0.395$ and $B = 4.4$.

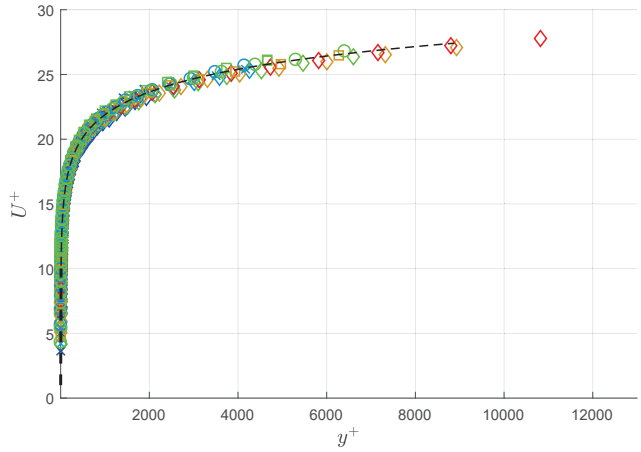

Figure 4.2: Normalized mean velocity profiles for all data-sets in table 2.2; the values of log-law coefficients shown for reference in the figure as a black dashed line are $\kappa = 0.395$ and $B = 4.4$.

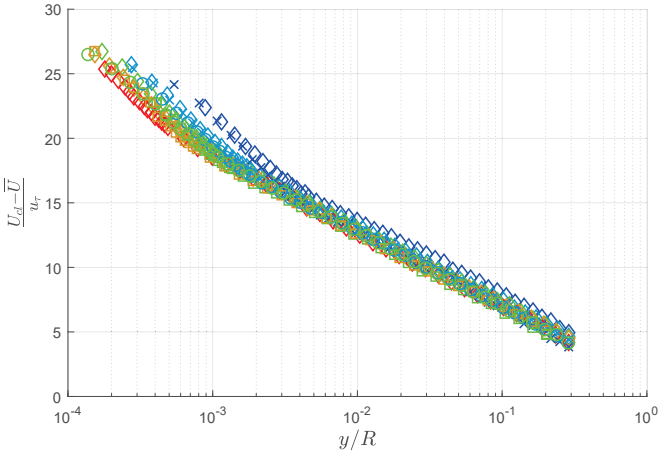

Figure 4.3: Inner normalized velocity defect in outer scaling.

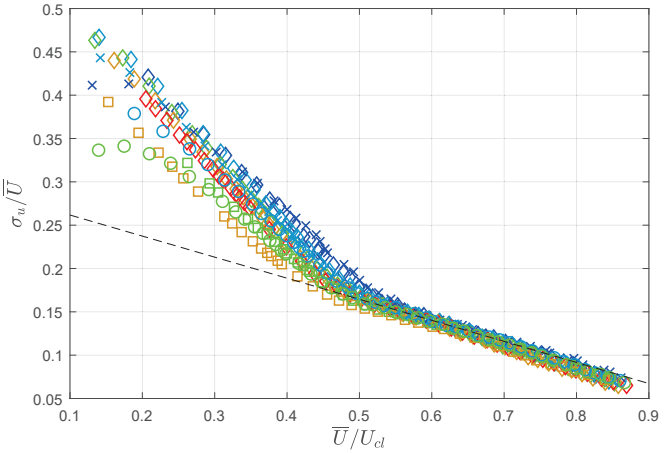

Figure 4.4: Diagnostic plot. $--$; $\sigma_u/\overline{U} = 0.286 - 0.243\ (\overline{U}/U_{cl})$ as reported by Alfredsson *et al.* (2012)

4.2. Streamwise normal stress

The inner-normalized streamwise variance $u^{2+} = \overline{u^2}/u_\tau^2$ is shown in figure 4.1 for all Reynolds number cases. For clarity, only one data-set from the most

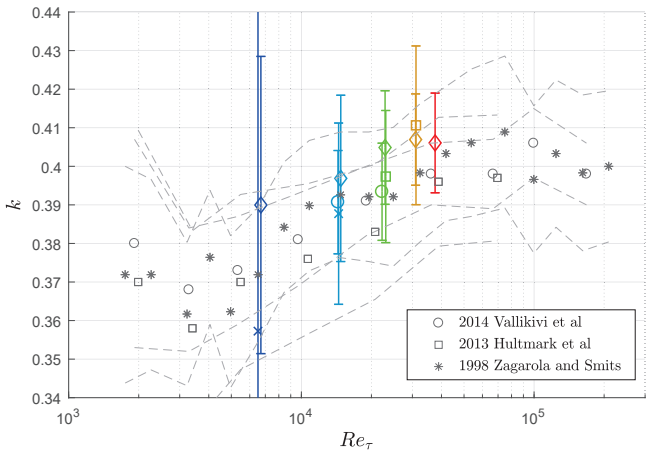

Figure 4.5: Value of the von Kármán coefficient κ computed from a fit in the region $200\, l_* < y < 0.15\, R$ for each velocity profile, compared with the results obtained with the same method in the Princeton Superpipe for different datasets, as reported by Bailey *et al.* (2014). Error-bars and dashed-lines represent the fit uncertainty.

well-resolved single wire sensor (with a length of 250 μm) is shown. The data is presented without any correction scheme applied. Despite the high resolution of the facility, some spatial filtering is to be expected, as for $Re_\tau = 3.8 \times 10^4$, $L^+ \approx 20$.

Using the semi-empirical correction scheme proposed by Smits *et al.* (2011*b*), where the corrected value of the normalized variance u^{2+} is found by multiplying the measured value u_*^{2+} with a function of the wall distance in viscous units y^+, the length of the wire in viscous units L^+ and the measured value of the near-wall maximum at $y^+ = 15$, $u_*^{2+}|_{y^+=15}$.

$$u^{2+} = u_*^{2+} \left[f(y^+) M(L^+, u_*^{2+}|_{y^+=15}) + 1 \right] \tag{4.2}$$

where M and f are:

$$M(L^+, u_*^{2+}|_{y^+=15}) = \frac{A\, tanh(\alpha L^+) tanh(\beta L^+ - E)}{u_*^{2+}|_{y^+=15}} \tag{4.3}$$

$$f(y^+) = \frac{15 + ln(2)}{y^+ + ln\left[e^{15-y^+}+1\right]} \tag{4.4}$$

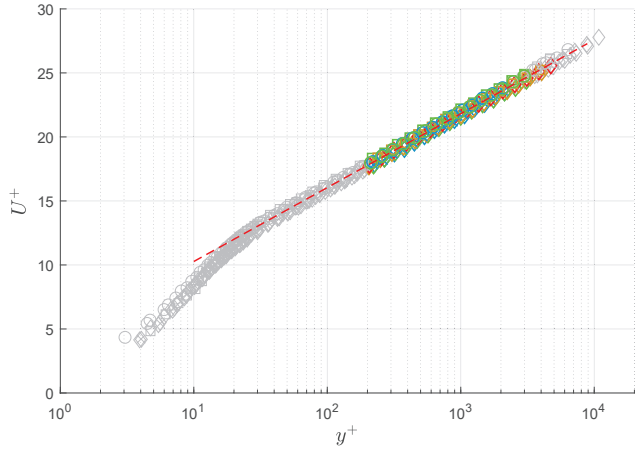

Figure 4.6: Normalized mean velocity profiles for all data-sets excluded the ones at $Re_\tau = 6.5 \times 10^3$; the values of log-law coefficients shown for in the figure as a red dashed line are $\kappa = 0.399$ and $B = 4.50$, resulting from fitting all data points in the region $0.15\ R < y < 200\ l_*$.

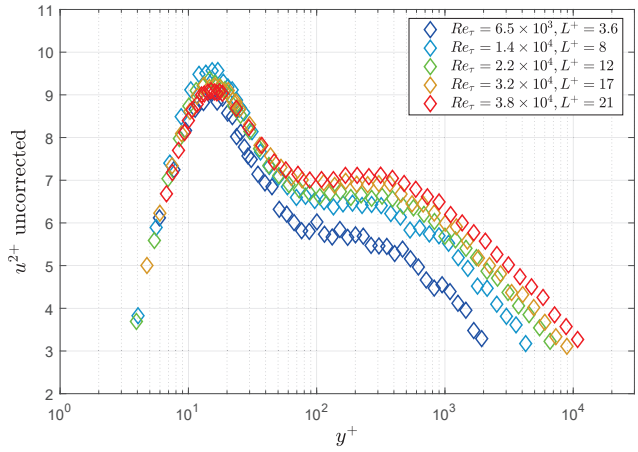

Figure 4.7: Inner-scaled streamwise velocity variance profile. Data shown is the measured one without any correction applied.

Where $\alpha = 5.6 \times 10^{-2}$, $\beta = 8.6 \times 10^{-3}$, $A = 6.13$ and $E = -1.26 \times 10^{-2}$ are fitting parameters. The result after correcting data with the proposed scheme is shown in figure 4.8. The data shows a visible increase of the peak at lower Reynolds number, after being corrected for spatial resolution using the previously described scheme. In figure 4.9 the corrected near-wall maximum u_m^{2+} is reported as a function of the friction Reynolds number Re_τ. The trend appears very clearly in a logarithmic scaling, and is in agreement with previously reported values by Örlü & Alfredsson (2013) in lower Reynolds number pipe experiments where the data was corrected using the same scheme, and roughly in agreement with the reported values by Metzger & Klewicki (2001). In Fig. 4.9 CICLoPE data is plotted together with the previously cited data reported in pipe experiments by Hultmark *et al.* (2012) and boundary layer by Vallikivi *et al.* (2015*b*). While there is experimental and numerical evidence to support the increase in the peak value, its rate of increase is not well determined. The rate of increase of the peak was quantified by Hutchins & Marusic (2007) who proposed an increase of 0.69 per decade in Re_τ for boundary layers, while Marusic *et al.* (2010*a*) estimated 0.96 per decade again for TBL. In the case of CICLoPE a logarithmic fit of the data results in:

$$u_m^{2+} = 0.640\, ln\,(Re_\tau) + 3.52 \tag{4.5}$$

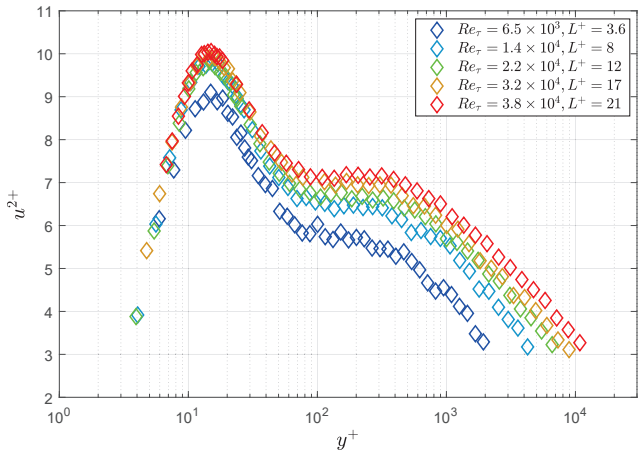

Figure 4.8: Inner-scaled streamwise velocity variance profile. Data shown applying the correction scheme proposed in Smits *et al.* (2011*b*).

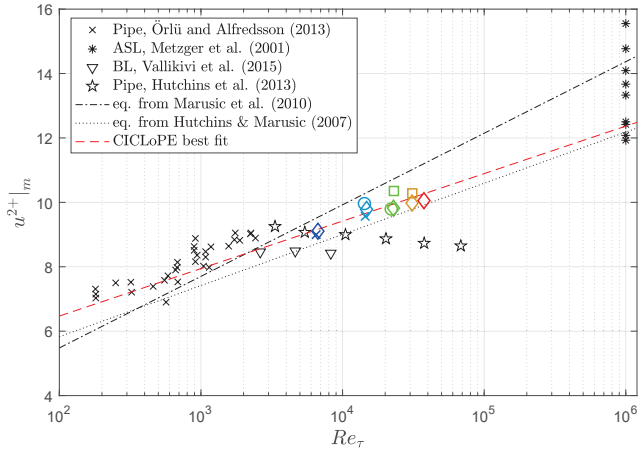

Figure 4.9: Near wall maximum of the Inner-scaled streamwise velocity. Symbols according to table 2.2 represent data corrected for spatial resolution, while grey symbols is uncorrected data. × is data reported in Ref. Örlü & Alfredsson (2013) and corrected using the same scheme.

As far as the 'second peak' observed in different Superpipe experiments (Vallikivi *et al.* (2011); Morrison *et al.* (2004); Hultmark *et al.* (2010, 2012, 2013)) and predicted by Alfredsson *et al.* (2011) is concerned, the present measurements do not confirm its presence, as no clear peak is visible up until the highest Reynolds number investigated here ($Re_\tau = 3.8 \times 10^4$), with the exclusion of data highly affected by spatial filtering. It should be noted however, that in Superpipe measurements at these Reynolds number such peak has only started to appear and is still quite 'subtle' in appearance. Although no clear peak is visible, a comparison can be made with the magnitude of the variance in the 'shoulder' of the profile. Hultmark *et al.* (2012) identified the location of the peak at $y^+_{II} \approx 0.23\, Re_\tau^{0.67}$; by using these locations a comparison can be made between the CICLoPE values and the peak magnitudes as reported by Vallikivi *et al.* (2015*b*) for pipe and boundary layer experiments at very high Reynolds number, the values are shown in Fig. 4.10. A surprisingly good agreement can be observed between the values of u^{2+} measured in CICLoPE in the expected location of the peak and the values from Superpipe experiments; taking into account uncertainties, the data also agrees well with what is measured in the atmospheric surface layer by Metzger *et al.* (2007). In Fig. 4.10 the expression logarithmic expression given by Pullin *et al.* (2013) is included, as well as the proposed trend of the u^{2+} shoulder by Monkewitz & Nagib (2015). By fitting a linear relationship in logarithmic scale on CICLoPE data, we obtain:

$$u_{II}^{2+} = 0.697\, ln\,(Re_\tau) - 0.358 \tag{4.6}$$

which is very similar to the rate of increase measured for the inner peak of variance at $y^+ = 15$.

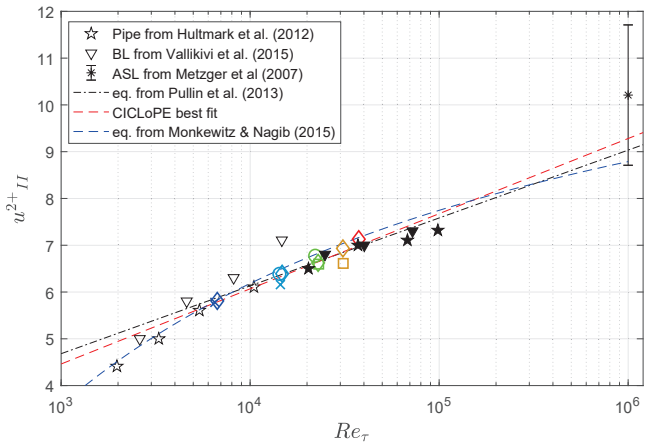

Figure 4.10: Outer peak of the Inner-scaled streamwise velocity. For CICLoPE values the location of the outer peak given in Hultmark *et al.* (2012) as $y^+_{II} \approx 0.23\, Re_\tau^{0.67}$ was used. Data from Vallikivi *et al.* (2015*b*) BL experiment and Hultmark *et al.* (2012) Pipe experiments are shown; filled symbols represent the data-sets where an outer peak was visible, for empty symbols the inflection points was used. Also shown the value measured by Metzger *et al.* (2007) in the atmospheric boundary layer. Dash-dotted line is the expression given by Pullin *et al.* (2013), while dashed line is the best fit to current CICLoPE measurements.

The measured profiles can be compared with those from the Superpipe; three cases were selected from the measurements of Hultmark *et al.* (2013), for having similar Re_τ and L^+ values to the data presented here, although it should be noted that in the Superpipe case experiments were performed with a nano-scale probe while here 'traditional' hot-wires with a higher l/d ratio were employed. In table 4.1 the flow cases from both facilities used in the comparison are detailed.

In figure 4.11 the three cases from both facilities are compared. Taking into account the difference in Reynolds number examined (up to 10 % for lower Re_τ

Facility	Re_τ	l_* $[\mu m]$	L $[\mu m]$	L^+
Superpipe	5.4×10^3	12	60	5.0
Superpipe	10.5×10^3	6.3	60	9.7
Superpipe	20.2×10^3	3.2	60	18.8
CICLoPE	6.7×10^3	67	250	3.7
CICLoPE	14.8×10^3	30	250	8.2
CICLoPE	22.9×10^3	19.6	250	12.7

Table 4.1: Experimental parameters of the 6 selected case for comparison between current CICLoPE measurements and Superpipe data from Hultmark *et al.* (2012).

case), some observations can still be made. First of all a very good agreement is observed for the low Reynolds number case, while at higher Reynolds number a deviation starts to appear for $y^+ < 100$ where the Superpipe data seems attenuated when compared to the one presented here. This, together with the fact that the value of the 'shoulder' measured in CICLoPE experiments is in line with the magnitude of the outer peak as reported by Hultmark *et al.* (2012) in Superpipe experiments (see Fig. 4.10), could lead to the indication that the observed outer peak is a by-product of an additional filtering of near wall fluctuations for $y^+ < 100$ in the Superpipe data. This could mean that the spatial filtering effect is either stronger or its influence extends further away from the wall than anticipated by the semi-empirical correction scheme applied by Smits *et al.* (2011*b*). Although to have any definitive conclusion on the matter CICLoPE Reynolds number range should be extended beyond $Re_\tau \approx 4 \times 10^4$ (as is indeed possible when using both the fans), the difference in L^+ is rather small and additional spatial filtering does not fully explain the different behaviour observed between the two data-sets for $y^+ < 100$.

Apart from the well-established logarithmic region in the mean velocity profile, with increasing Reynolds number a logarithmic region for all even order moments of the streamwise velocity is expected to appear in outer scaling following the prediction of the attached eddy model by Townsend (1976) and this behaviour has recently found support in experimental data (Meneveau & Marusic (2013); Zhou & Klewicki (2015)). Thus, the normalized streamwise variance u^{2+} is expected to follow equation (4.7):

$$u^{2+} = B_2 - A_2 \, ln \left(\frac{y}{R}\right) \tag{4.7}$$

Where A_2, the so called *Townsend-Perry constant* is expected to reach a universal value for high Reynolds numbers, according to Meneveau & Marusic (2013), while in the scaling proposed by Monkewitz & Nagib (2015) the slope of the

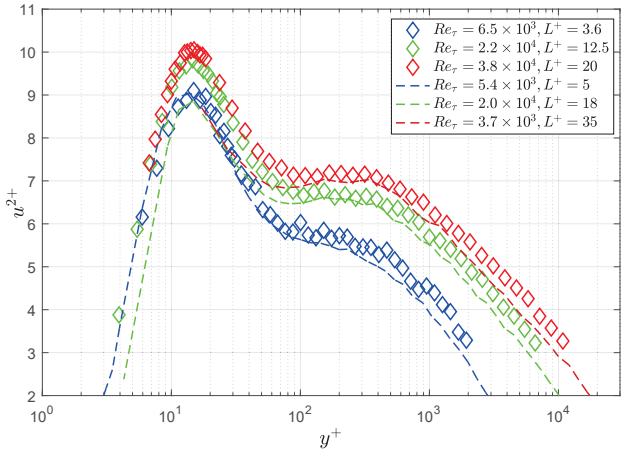

Figure 4.11: Inner-scaled streamwise variance from both Superpipe and CICLoPE. Dashed lines is data from the Superpipe (Hultmark *et al.* (2013)), while diamond symbols is data from current measurements for the cases listed in table 4.1. Both data-sets were corrected with the same correction scheme by Smits *et al.* (2011*b*).

logarithmic region changes with Re and is not universal. Recent high Reynolds number experiments in pipe by Hultmark *et al.* (2012) report a logarithmic behaviour for $Re_\tau > 2 \times 10^4$ with values of $A_2 = 1.24$, and $B_2 = 1.48$, which Vallikivi *et al.* (2015*b*) found to agree very well with boundary layer results at similar Reynolds number. The normalized variance is shown in figure 4.12 in outer scaling. As predicted by the attached eddy model, the data collapses well into a logarithmic behaviour in outer scaling. The lower limit of the logarithmic behaviour for variance is believed to be further away from the wall compared to the mean; Meneveau & Marusic (2013) propose a lower limit of $y^+ \approx 3\, Re_\tau^{0.5}$, this value is supported theoretically by the analysis of Klewicki (2013) according to which $y^+ \approx 2.6\, Re_\tau^{0.5}$ is where the mean lose a leading order viscous effect. Fitting CICLoPE data in the region $y^+ > 600$, $y/R < 0.25$, yields:

$$u^{2+} = 1.81 - 1.26\, ln\, \left(\frac{y}{R}\right) \tag{4.8}$$

The Value of the Townsend-Perry constant $A_2 \approx 1.26$ is very similar to the one reported in the Superpipe, while the additive coefficient $B_2 \approx 1.81$ is higher than reported value of 1.48, although it agrees nicely with pipe DNS by Ahn *et al.* (2013) performed at $Re_\tau = 3 \times 10^3$.

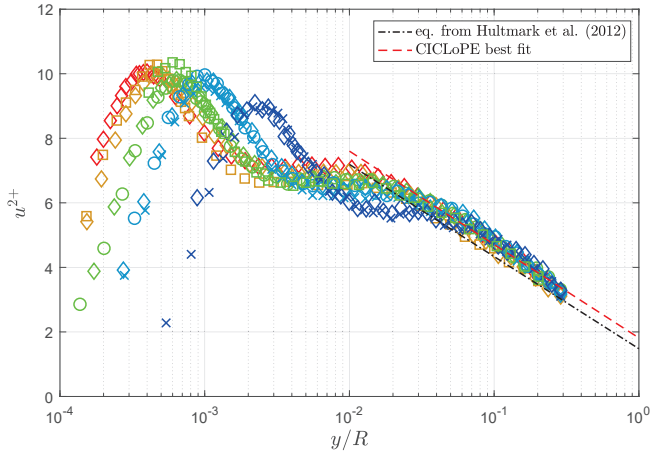

Figure 4.12: Outer-scaled streamwise velocity variance profiles. Dashed line represent best fit on CICLoPE data, dash-dotted line is expression reported in Hultmark *et al.* (2012) to fit Superpipe data.

4.3. Other Reynolds stresses

Apart from the streamwise Reynolds normal stress $\overline{u^2}$, the other elements of the Reynolds stress tensor were measured in two additional set of profiles with an x-wire probe positioned first with the wires on the $x-r$ and then on the $x-\theta$ plane, to be able to measure the V and W velocity components, albeit not simultaneously. Given the straight probe-holder and the traversing used, geometrical constraints made impossible to come closer than 3.5 mm to the wall in physical distance. In Fig. 4.13 are shown together the mean streamwise velocity U^+ and the normal Reynolds shear stress u^{2+} from the 0.25 mm single-wire dataset and the x-wire measurements to asses the agreement between the two. The data displays a particularly good agreement on the streamwise variance, while there is a noticeable deviation on the mean velocity, which appears shifted upwards for almost all x-wire profiles. However streamwise velocity data is not the main aim of the x-wire measurements, and some interference effects might have come into play for the more cumbersome x-wire probe.

All the Reynolds stresses measured in CICLoPE are shown in Fig. 4.14 normalized with u_τ^2 as a function of wall-normal distance in outer scaling. These results were presented in Örlü *et al.* (2017). A small degree of scatter is noticeable in the data and no clear Re variation appears, so only general trends will be assessed. The normal streamwise Reynolds stress confirms the behaviour observed in single wire measurements, with a logarithmic decay that collapses

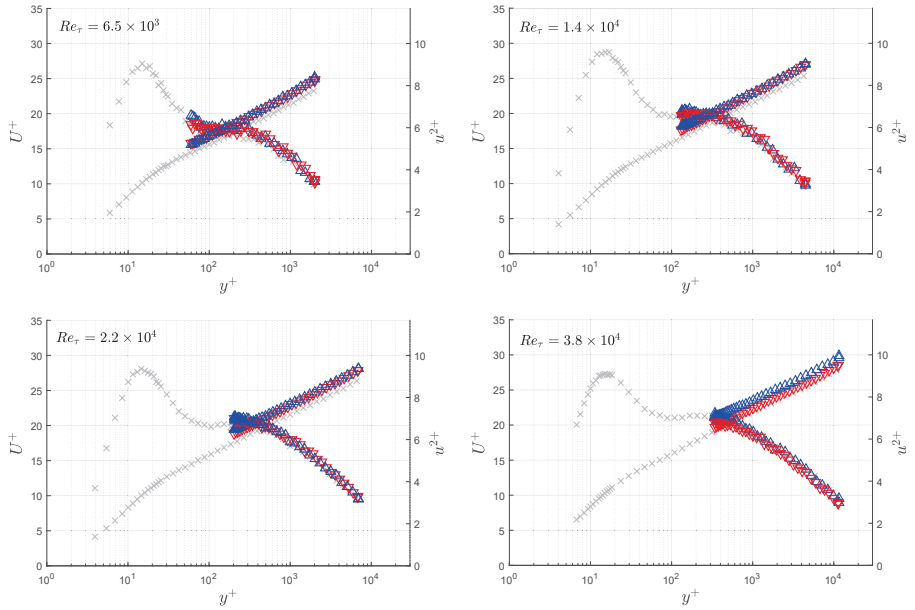

Figure 4.13: Inner-normalized streamwise mean velocity U^+ and inner-normalized streamwise variance u^{2+} (multiplied by 3 to fit the scale) as a function of wall units y^+. $\times$; single wire data from probe n. 3 in table 2.1. $\bigtriangledown$; x-wire data in $U-W$ configuration. $\bigtriangleup$; x-wire data in $U-V$ configuration.

for different Reynolds numbers in outer scaling on equation (4.8). The uw^+ stress is close to zero for all datasets taken in the $U-W$ configuration, and the shear stress uv^+ has a plateau at -1 for the profiles in $U-V$ configuration, as it should be. This, together with the good agreement shown in Fig. 4.13, is a qualitative demonstration of the good angular calibration of the probe. It should be underlined that while the L^+ values for the x-wire measurements are in the range $8-40$ and this implies that there is some degree of spatial filtering, it most likely doesn't concern the wall-normal locations examined here. In-fact, applying the correction of Smits *et al.* (2011*b*), no discernible difference can be noticed. Regarding the other Reynolds stresses, the wall-normal and spanwise component, there is very few experimental data regarding them and none at high Reynolds number. Buschmann & Gad-el Hak (2010) collected and compared various DNS and experimental data-sets regarding wall-normal and spanwise components of Reynolds stresses. The wall-normal Reynolds stress measured here shows an almost constant value of $v^{2+} \approx 2$, while the spanwise normal stress $w^{2+} \approx 2$ shows a rather clear logarithmic decay with

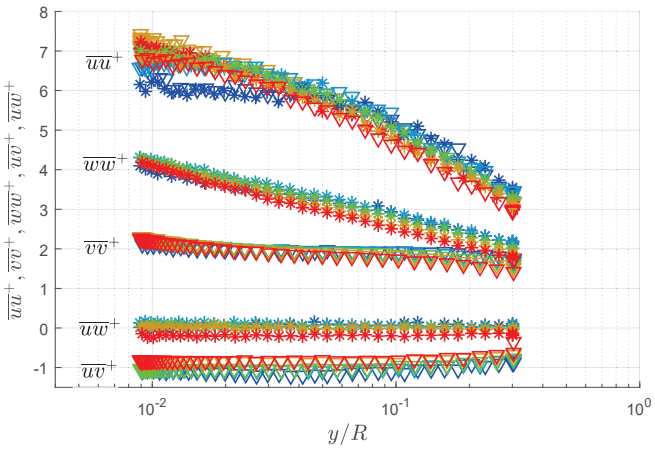

Figure 4.14: Reynolds stress tensor elements normalized with u_τ^2 as a function of wall-normal distance in outer scaling. The symbols used are those reported in table 2.2.

y/R, although not as fast as the streamwise normal stress u^{2+}. The attached eddy model (Townsend (1976)) predicts the following behaviour of these two Reynolds stresses in the overlap region:

$$v^{2+} = B_v \tag{4.9}$$

$$w^{2+} = B_w - A_w \, ln(y/R) \tag{4.10}$$

Where B_v, B_w and A_w are constants. Generally the DNS and the few experimental data tend to support the scaling of the attached eddy model, with the recent exception of the experimental study from Morrill-Winter *et al.* (2015) in boundary layers, that do not support the plateau scaling for v^{2+} but instead a weak logarithmic increase with a peak at the edge of the overlap layer. Qualitatively CICLoPE data agrees well with the model, and by fitting the data to the expressions in eq (4.9), the following values can be obtained for B_v, A_w and B_w:

$$v^{2+} = 2.01 \tag{4.11}$$

$$w^{2+} = 1.21 - 0.64 \, ln(y/R) \tag{4.12}$$

Current data can be compared with the highest available DNS of pipe flow at $Re_\tau = 3008$ by Ahn *et al.* (2015), as shown in Fig. 4.15. Numerical data agrees well with the present experimental results for what concerns u^{2+} and uv^+, and although the near-constant value of v^{2+} and the logarithmic

behaviour of w^{2+} are found both in the present experimental results and in DNS data, it must be noted that the magnitude of these last two quantities are positively higher for the present data. High Re x-wire measurements in the Superpipe were reported in Zhao & Smits (2007), and measured a constant value of v^{2+} with $B_v \approx 1.32$ in the log layer, although with a very high value of L^+ up to $\approx$ 1200. Boundary layer experiment seems to agree with this value, as both LDV data from De Graaff & Eaton (2000) and PIV data from Carlier & Stanislas (2005) show a plateau at $v^{2+} \approx 1.3$. One exception is the experimental study of Kunkel & Marusic (2006), performed in the atmospheric surface layer, in which the v^{2+} plateau has a value of ≈ 1.8, which is the closest to the value reported here.

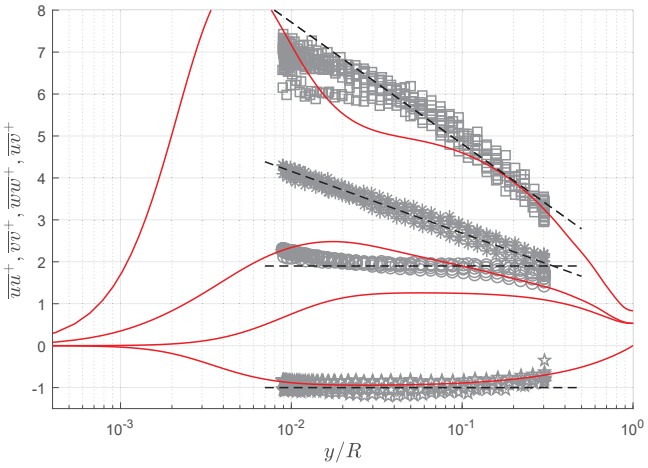

Figure 4.15: Grey symbols are present measurements. −−; trends from present measurements as expressed in eq. 4.8 and 4.11. —; Pipe DNS by Ahn *et al.* (2015) at $Re_\tau = 3008$.

4.4. Higher order moments

The skewness and flatness factor S_u and F_u are shown in this section in inner and outer coordinates in figures 4.16 - 4.19; for clarity only the complete data-set for the most spatially-resolved case is shown (the 250 μm long hot-wire, indicated as probe n. 3 in table 2.1). Skewness and flatness factor are defined as:

$$S_u = \frac{\overline{u^3}}{\overline{\sigma_u^3}} \tag{4.13}$$

$$F_u = \frac{\overline{u^4}}{\sigma_u^4} \tag{4.14}$$

Where σ_u is the standard deviation of the streamwise velocity. Skewness in inner scaling, shown in Fig. 4.16, displays a positive value near the wall, for $y^+ < 200$ while it becomes negative further away from the wall. The inner scaling does not collapse the value of the skewness on a single curve, with a residual Reynolds number effect visible; although it should also be noted that different data-sets corresponds to different L^+ values, hence a different spatial filtering effect is also present which could be masking a true Reynolds number behaviour. No well-established correction method in the case of higher order moments, unlike the variance, exists. Different Reynolds number cases collapse reasonably well for $y^+ > 100$, keeping in mind that these measurements are taken up to $y/R = 0.3$ due to current limitations of the traversing set-up, so no wake region is clearly visible, where S_u would scale in outer units. A good agreement is just starting to show in Fig. 4.18 for the outer part of the profile. Considering the flatness factor shown in Fig. 4.17 in inner scaling, a small region where $F_u > 3$ can be observed, for $y^+ < 10$, while the behaviour remains sub-gaussian for the rest of the profile, because no wake region is measured here, where flatness would be $F_u > 3$, although an increasing trend is starting to show. Viscous scaling shows a good agreement for $y^+ > 50 - 60$ and $y/R < 0.2$ with an apparent Reynolds number effect in the region closer to the wall. In outer scaling there is good collapse for $y/R > 0.003$ with the exception of the lower Re_τ profile.

4.5. Spatial resolution effects

4.5.1. L^+ *effects on streamwise variance*

In this subsection, more plots showing the variance of the streamwise velocity are shown, with particular focus on the effect of spatial resolution. The measurements taken with different probes at the same Reynolds number can be examined. Those are shown in figures 4.20 - 4.23, with both the measured and the corrected data-sets. In figure 4.20 it is possible to notice a vey small deviation between the two probes thanks to the very low values of L^+; and an attenuation effect is only barely noticeable between the two. In figure 4.21 at $Re_\tau \approx 1.5 \times 10^4$ the spatial filtering effect becomes clearly visible and the correction scheme works very well, with the three corrected values collapsing almost flawlessly. Results at $Re_\tau \approx 1.5 \times 10^4$, shown in figure 4.22 start to show the appearance of a 'synthetic' outer peak, in the more filtered data-sets, as already shown experimentally at lower Reynolds number by Hutchins *et al.* (2009); it is worth noting that in this case the spatial resolution correction

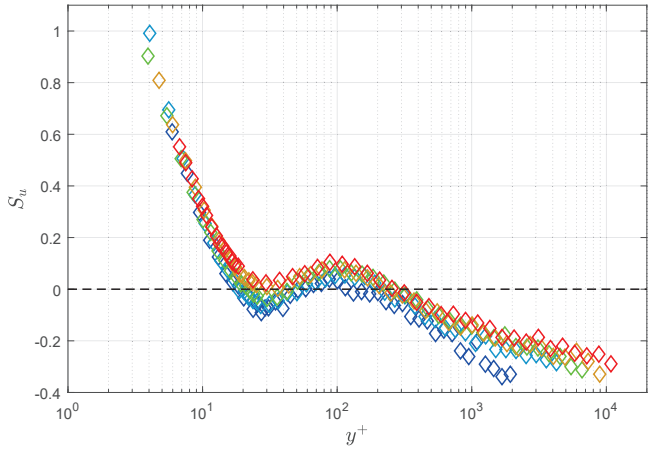

Figure 4.16: Skewness factor in inner scaling, the dashed black line corresponds to a gaussian behaviour, with $S_u = 0$.

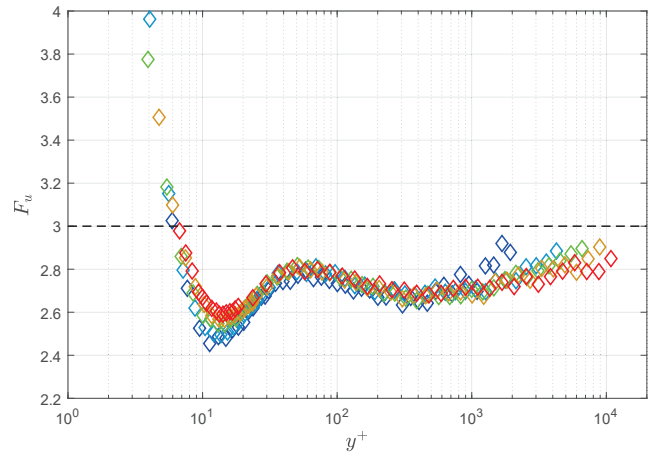

Figure 4.17: Flatness factor in inner scaling, the dashed black line corresponds to a gaussian behaviour, with $F_u = 3$.

employed do not restore a perfect collapse of the measured data, with the notable deviation of the data measured by the 55P11 Dantec probe, which is corrected to a value above other measurements. For $Re_\tau \approx 3.8 \times 10^4$, the outer

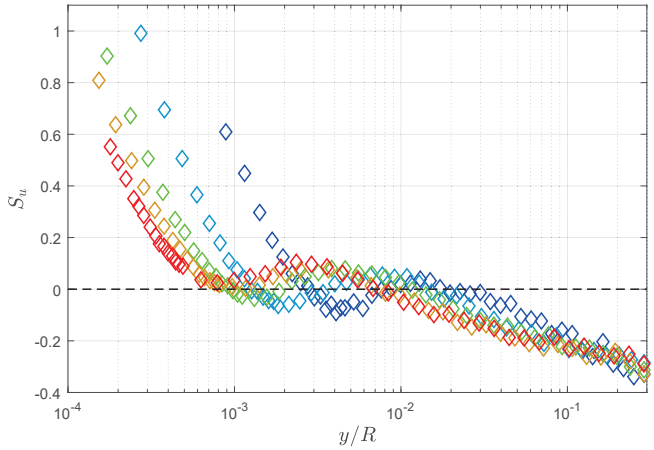

Figure 4.18: Skewness factor in outer scaling, the dashed black line corresponds to a gaussian behaviour, with $S_u = 0$.

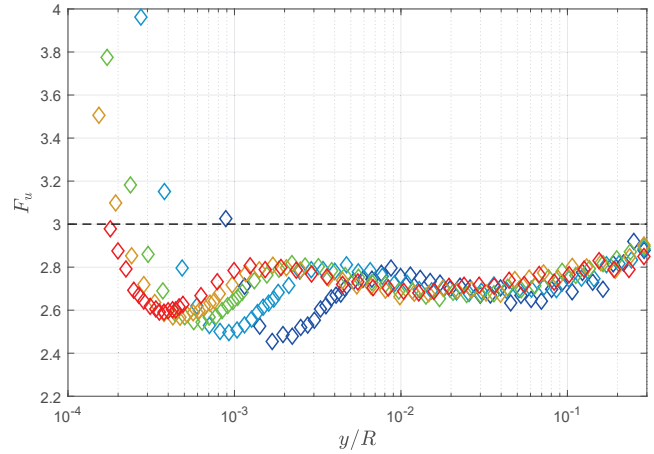

Figure 4.19: Flatness factor in outer scaling, the dashed black line corresponds to a gaussian behaviour, with $F_u = 3$.

bump resulting from insufficient spatial resolution becomes more obvious, and

the correction scheme returns a reasonable agreement. For the highest Reynolds number case, $Re_\tau \approx 3.8 \times 10^4$ only one data-set of the 0.25 mm probe is available, so no considerations can be made.

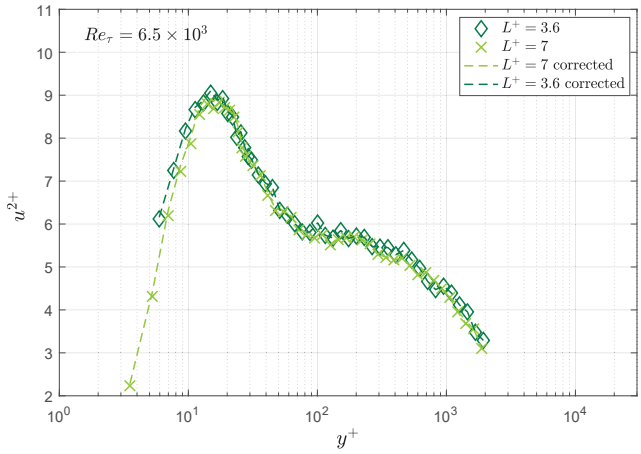

Figure 4.20: Inner-scaled streamwise variance for $Re_\tau \approx 6.5 \times 10^3$

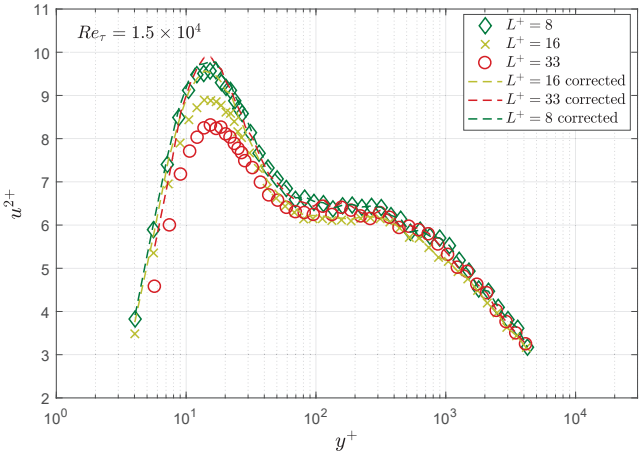

Figure 4.21: Inner-scaled streamwise variance for $Re_\tau \approx 1.5 \times 10^4$

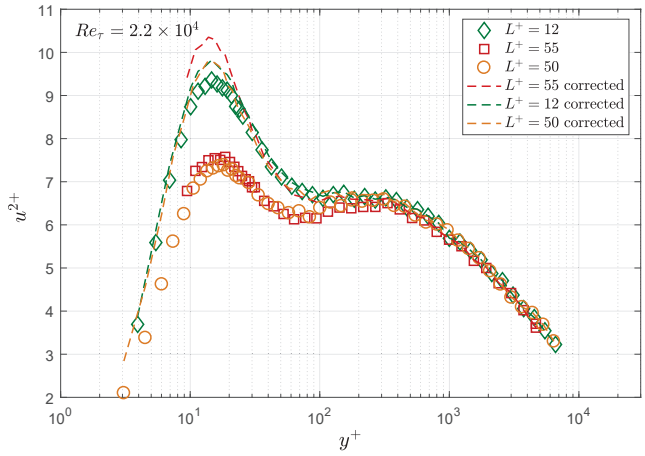

Figure 4.22: Inner-scaled streamwise variance for $Re_\tau \approx 2.2 \times 10^4$

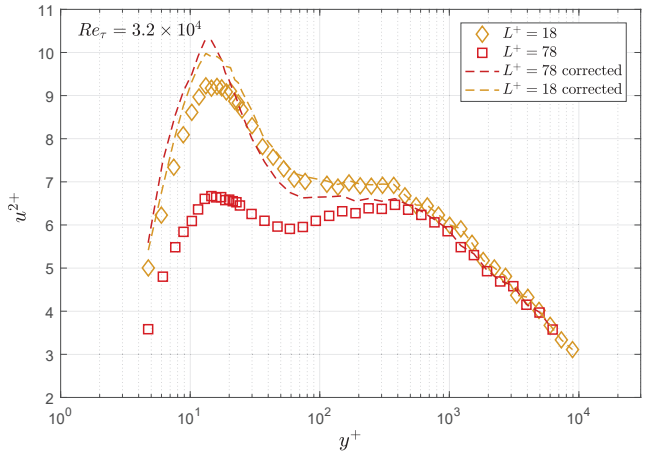

Figure 4.23: Inner-scaled streamwise variance for $Re_\tau \approx 3.2 \times 10^4$

4.5.2. L^+ *effects on higher order moments*

In this sub-section, the 3rd and 4th order statistics are analysed for matching Reynolds number cases, in order to qualitatively asses the effect of a finite sensor length on the measured statistics. As previously reported, most of the

work so far on spatial resolution of hot-wire measurements has been directed towards the effect on the second order statistical moment and in particular the attenuation observed for the normalized streamwise variance, u^{2+}, when the length of the hot-wire sensor in viscous units, L^+, is increased. As far as the higher order moments, no established method of correction exist and the extent of the effect that an insufficient spatial resolution has on them is not entirely clear. In their very influential work, Ligrani & Bradshaw (1987) state that: "...a wire length of (very roughly) 20-25 viscous length scales may be a limiting value for measuring flatness factor and skewness...", based on their own measurements and Johansson & Alfredsson (1983) boundary layer data . As can be seen from Fig. 4.24 - 4.31, where S_u and F_u are reported in inner scaling for matching Reynolds number cases and different L^+ values, the spatial resolution affects also higher order moment. The attenuation is particularly visible around the local near-wall minimum of both moments, that for the skewness is located at $y^+ \approx 30$ and for the flatness at $y^+ \approx 15$. While the attenuation does not appear to be as severe as the one found on the second order moment, it is still distinctly present and with a magnitude able to cover any apparent Reynolds-number effect that is displayed in Fig. 4.16 and 4.17. As can be seen in Fig. 4.29 and 4.30, the filtering effect for the relative un-resolved cases is enough to mask the negative region of skewness factor found at $y^+ \approx 30$ for the better-resolved cases, and for $L^+ \approx 60 - 70$, the local minimum disappears entirely. A similar attenuation of the local minimum affects also the flatness factor, for which an insufficient spatial resolution has the additional effect of shifting the location of the minimum from $y^+ \approx 15$ to $y^+ \approx 20$ for stronger attenuations, see Fig. 4.26. In Fig. 4.32 and 4.33 the near-wall minima of higher order moments are plotted as a function of the viscous scaled-wire length. From both figures the trend due to spatial filtering is clear. The number of cases from present measurements, in particular those with matching L^+ values, is not sufficient to settle the presence (or lack thereof) of a scaling of these moments with Reynolds number. However, it is clear that these statistical quantities are considerably affected by insufficient spatial resolution in the near-wall region, so much that if a Reynolds number effect is present, it is small and covered by the spatial resolution effect.

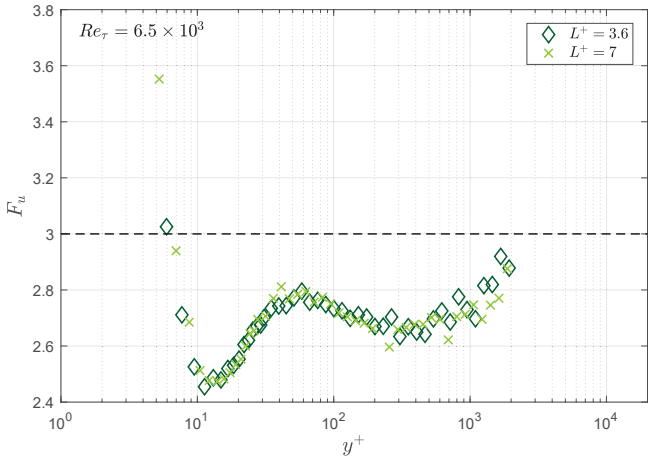

Figure 4.24: Flatness factor in inner scaling, measured with different hot-wires for $Re_\tau \approx 6.5 \times 10^3$; the dashed black line corresponds to a gaussian behaviour, with $F_u = 3$.

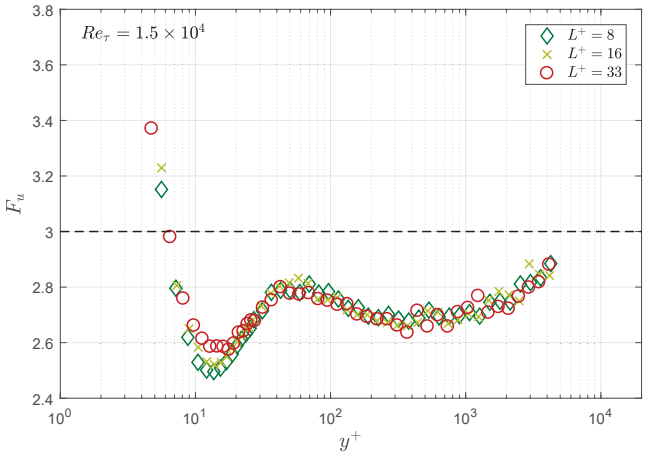

Figure 4.25: Flatness factor in inner scaling, measured with different hot-wires for $Re_\tau \approx 1.5 \times 10^4$; the dashed black line corresponds to a gaussian behaviour, with $F_u = 3$.

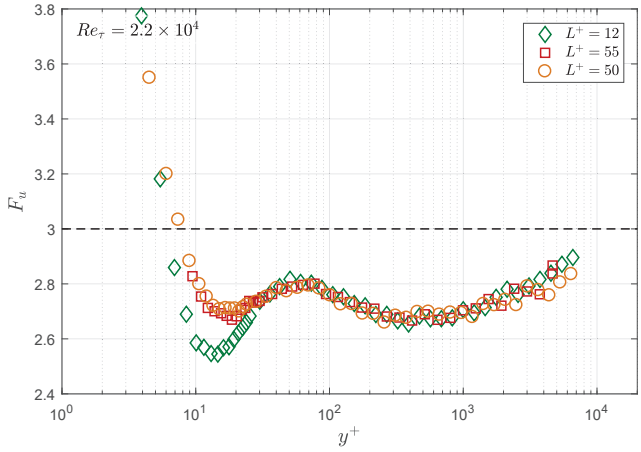

Figure 4.26: Flatness factor in inner scaling, measured with different hot-wires for $Re_\tau \approx 2.2 \times 10^4$; the dashed black line corresponds to a gaussian behaviour, with $F_u = 3$.

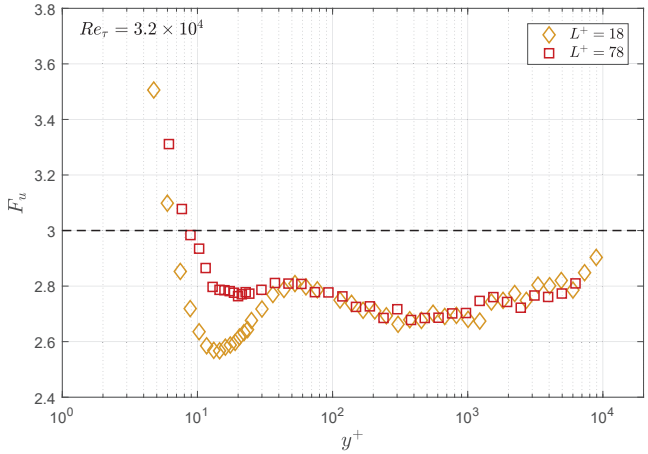

Figure 4.27: Flatness factor in inner scaling, measured with different hot-wires for $Re_\tau \approx 3.2 \times 10^4$; the dashed black line corresponds to a gaussian behaviour, with $F_u = 3$.

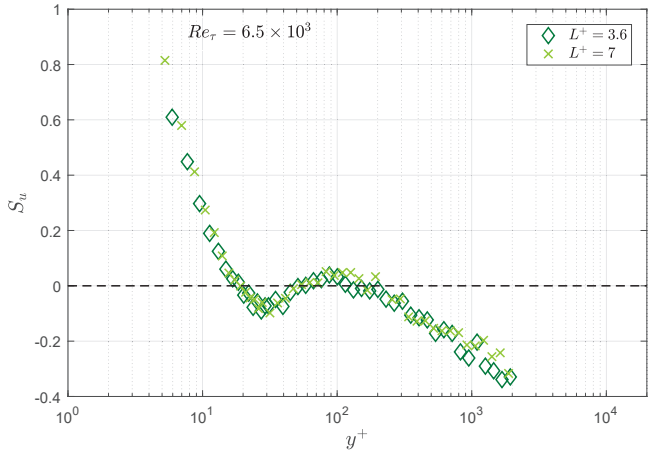

Figure 4.28: Skewness factor in inner scaling, measured with different hot-wires for $Re_\tau \approx 6.5 \times 10^3$; the dashed black line corresponds to a gaussian behaviour, with $S_u = 0$.

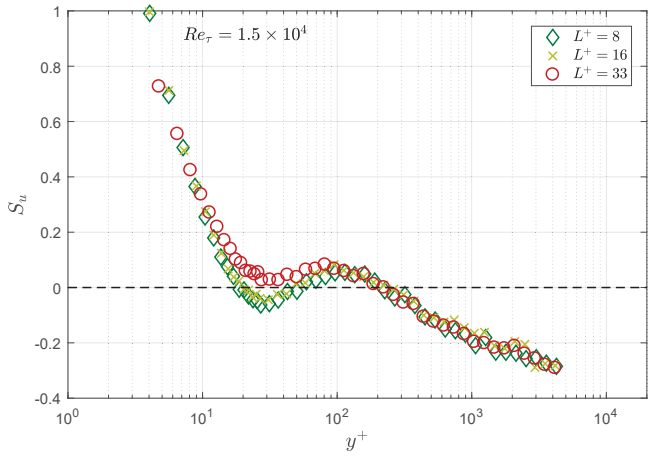

Figure 4.29: Skewness factor in inner scaling, measured with different hot-wires for $Re_\tau \approx 1.5 \times 10^4$; the dashed black line corresponds to a gaussian behaviour, with $S_u = 0$.

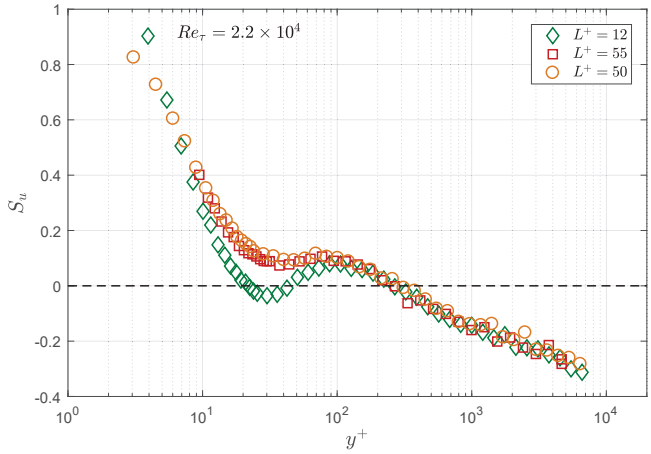

Figure 4.30: Skewness factor in inner scaling, measured with different hot-wires for $Re_\tau \approx 2.2 \times 10^4$; the dashed black line corresponds to a gaussian behaviour, with $S_u = 0$.

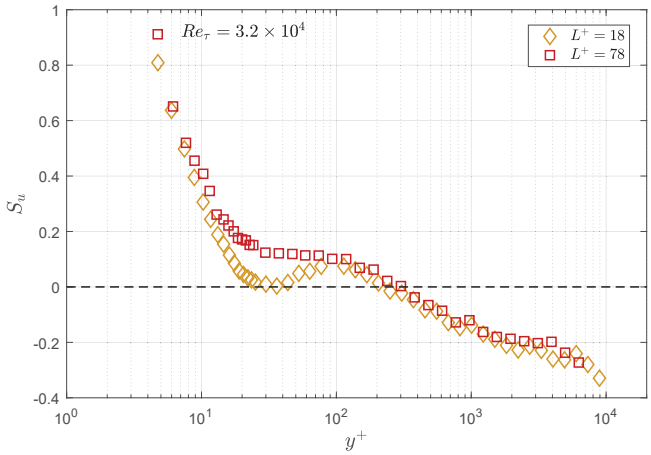

Figure 4.31: Skewness factor in inner scaling, measured with different hot-wires for $Re_\tau \approx 3.2 \times 10^4$; the dashed black line corresponds to a gaussian behaviour, with $S_u = 0$.

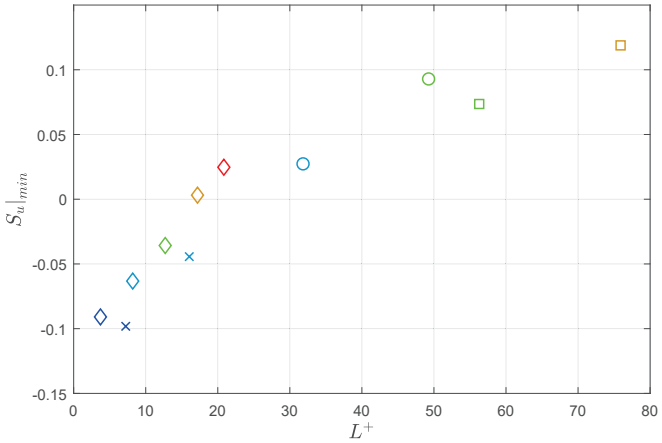

Figure 4.32: Value of the local minimum of the skewness factor S_u found at $y^+ \approx 30$ as a function of viscous-scaled wire length for current measurements. Symbols from current measurements corresponds to the ones in table 2.2.

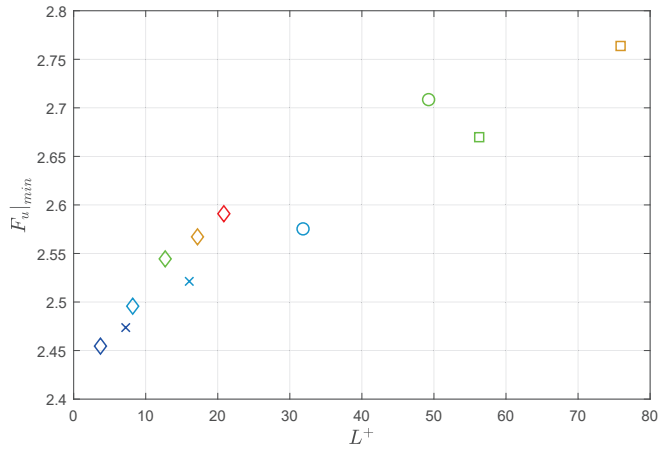

Figure 4.33: Value of the local minimum of the flatness factor F_u found at $y^+ \approx 15$ as a function of viscous-scaled wire length for current measurements. Symbols from current measurements corresponds to the ones in table 2.2.

CHAPTER 5

Spectral and quadrant analysis

Two of the features that characterize wall-bounded turbulence are the presence of a great variety of scales, and its highly random and intermittent nature. Coherent motions can be found ranging from the order of the viscous length scale l_* to the outer length scale, in the case of a pipe the radius R. In the first part of this chapter, the structure of turbulence is analysed, while in the second part the focus is on the identification description of sudden and strong events that occur in wall turbulence.

5.1. Spectra of streamwise velocity fluctuations

the power spectral density (PSD) of velocity fluctuations can be analysed to infer informations on turbulent coherent motions. Spectral analysis reveals how the energy of turbulent fluctuations is distributed among frequencies and, using frozen turbulence hypothesis by Taylor (1938), to associate them with characteristic wave-lengths of turbulent motions, providing valuable information on the structure of turbulence. The validity of Taylor's hypothesis for wall bounded flows has been debated by Del Álamo & Jiménez (2009), who showed from DNS results that the large structures do not travel with the local mean velocity close to the wall but rather with the bulk velocity, but the hypothesis remains a good approximation for most of the flow field. In Fig. 5.2 - 5.6 are shown the pre-multiplied wavenumber spectral maps of the streamwise turbulent fluctuations, normalized in inner units, $\Phi_{uu}k_x/u_\tau^2$. The spectra can be plotted as a function of wall distance in inner units y^+ and inner-normalized frequency f^+, defined as:

$$f^+ = \frac{f\, l_*}{u_\tau} \tag{5.1}$$

or alternatively the streamwise wavenumber k_x or its inner-normalized counterpart k_x^+ can be used, which is found using the local mean velocity as the convection velocity:

$$k_x = \frac{2\pi f}{\overline{U}} \tag{5.2}$$

$$k_x^+ = k_x l_* \tag{5.3}$$

To help a visual understanding of how much energy is associated with different scales, PSDs are plotted in pre-multiplied form. When the pre-multiplied power spectral density is plotted on a semi-logarithmic scale, the area below the curve is proportional to the actual variance of turbulent fluctuations. An example of a power spectral density map is reported in Fig. 5.1 as a function of the inner-scaled wall distance y^+ and the inner-scaled frequency $f^+ = fl_*/u_\tau$. A visual inspection of the image allows to identify two peaks: one very sharp and located close to the wall at relatively high frequencies, and another located in the overlap region, lower in magnitude, broader and characterised by a lower frequency. This two features of the pre-multiplied power spectra will be referred to as *inner spectral peak* (ISP) and *outer spectral peak* (OSP), respectively.

5.1.1. *Inner and outer spectral peaks*

Any analysis to be performed on these features require first to locate them. For the present data, a Gaussian surface was locally fitted near the position of the peaks to find their location in (y^+, f^+) coordinates; a fitting procedure was performed with a 2-d Gaussian function of the type:

$$F(x,y) = Ae^{-\left(\frac{(x-x_0)^2}{2\sigma_x^2} + \frac{(y-y_0)^2}{2\sigma_y^2} - \frac{2\rho_{xy}(x-x_0)(y-y_0)}{\sigma_x\sigma_y}\right)} \tag{5.4}$$

Where $A, x_0, y_0, \sigma_x, \sigma_y$ and ρ_{xy} are parameters found by least-square fitting. The starting point of the iterative procedure was manually selected case-by-case, as well as the region of the spectra around the peaks' expected locations, to be used as data points for the fit. An example of the procedure outcome is displayed in Fig. 5.1 for the $Re_\tau = 2.2 \times 10^4$ case. The peaks location was then computed as the maximum of the resulting fitted function.

Power spectral density maps for all Reynolds number cases are shown in Fig. 5.2 - 5.6 as a function of y^+ and the inner-normalized streamwise wavenumber $k_x^+ = k_x l_*$, computed using Taylor's frozen turbulence hypothesis.

The inner spectral peak (ISP) is located at the same wall-normal distance that corresponds to the streamwise variance peak ($y^+ \approx 13 - 14$); so that the peak in the variance profile is predominantly caused by the relatively high frequencies (hence small scales) of ISP. As wall-normal distance is increased however, energy gets distributed over a wider range of scales, with the eventual appearance of the OSP in the overlap region, that becomes more prominent as the Reynolds number increases. In fact, while a substantial similarity can be noticed in the near-wall region between different flow-cases, a higher magnitude of the low-frequency contribution in the overlap-region clearly develops as Reynolds number is increased. This indicates that the inner scaling used here for the pre-multiplied spectra doesn't represent well the larger scale coherent structures of the overlap layer, whose energy contribution keeps growing with Reynolds number. The outer spectral peak has been associated to the energy contribution of the Very Large Scale Motions (VLSM). According to Hutchins

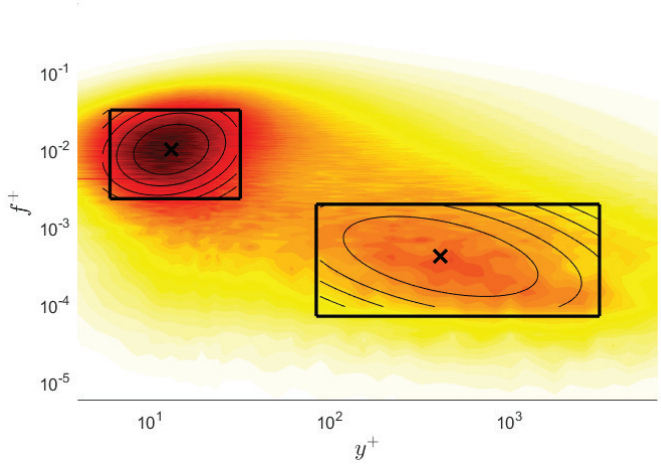

Figure 5.1: Example of the fitting procedure used to locate the spectral peaks. The black rectangles show the region of data that was used for the fit, the black contour lines are the function of the type of eq. (5.4) resulting from the fit, while the black crosses are the peaks locations.

& Marusic (2007) the OSP is expected to appear for $Re_\tau \approx 1700$; Mathis *et al.* (2009) identified its location to correspond roughly to the geometric centre of the logarithmic region in the mean velocity profile, and proposed $y^+ \approx 3.9\sqrt{Re_\tau}$ as the peak's location.

The location of the spectral peaks, identified with the aforementioned fitting method, can be analysed in wavenumber and space domain. In Fig. 5.7 the wall-normal location of both peaks is plotted against Reynolds number. The location of the ISP is nearly constant in inner scaling at $y^+ \approx 12 - 13$, while the location of the OSP clearly moves away from the wall in inner units as Reynolds number is increased. The location of both peaks in outer scaling shows how they both move closer to the wall in physical space. The OSP location of the present data agrees well with the analysis performed by Vallikivi *et al.* (2015*a*) using pipe data from Hultmark *et al.* (2012), despite the different algorithm used for the peak location. In Fig. 5.8 the wavenumber of the peaks is reported, the inner-scaled wavenumber of the ISP shows a slight decreasing trend. However, this could be caused by the use of the local mean velocity to determine k_x. To eliminate the influence of Taylor hypothesis, the same analysis can be done in the frequency domain, as shown in Fig. 5.9. Now the ISP inner normalized frequency location appears almost constant at $f^+ \approx 0.01$, while the outer spectral peak shifts towards lower inner-scaled frequencies.

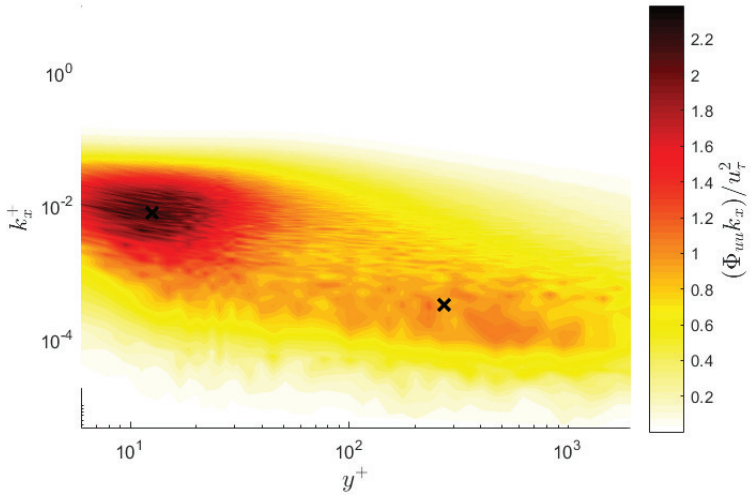

Figure 5.2: Contour plot of the pre-multiplied power spectral density of the streamwise velocity fluctuations for $Re_\tau \approx 6.5 \times 10^3$

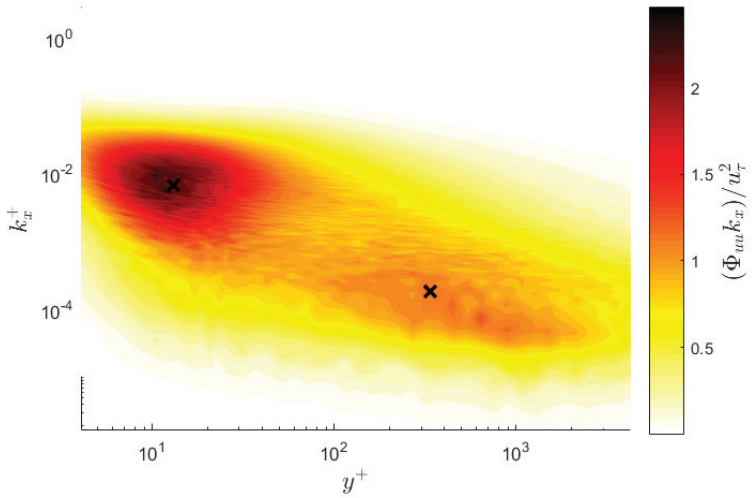

Figure 5.3: Contour plot of the pre-multiplied power spectral density of the streamwise velocity fluctuations for $Re_\tau \approx 1.4 \times 10^4$

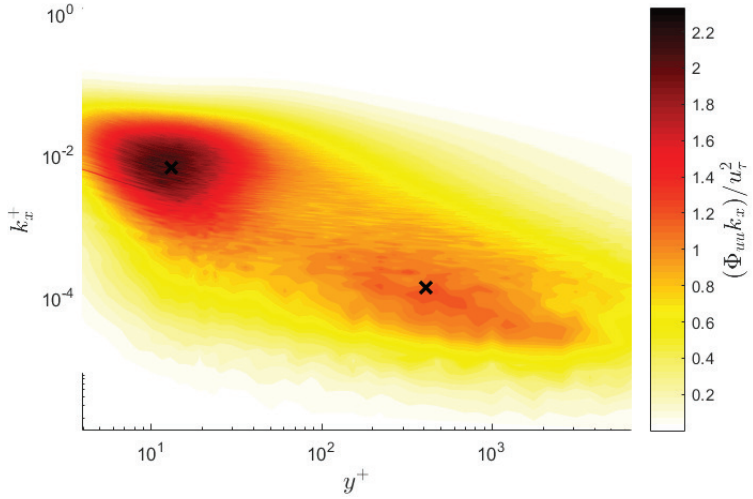

Figure 5.4: Contour plot of the pre-multiplied power spectral density of the streamwise velocity fluctuations for $Re_\tau \approx 2.2 \times 10^4$

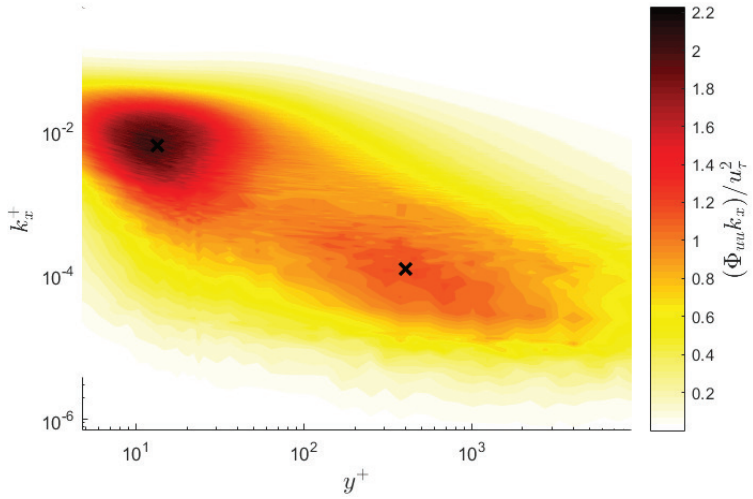

Figure 5.5: Contour plot of the pre-multiplied power spectral density of the streamwise velocity fluctuations for $Re_\tau \approx 3.2 \times 10^4$

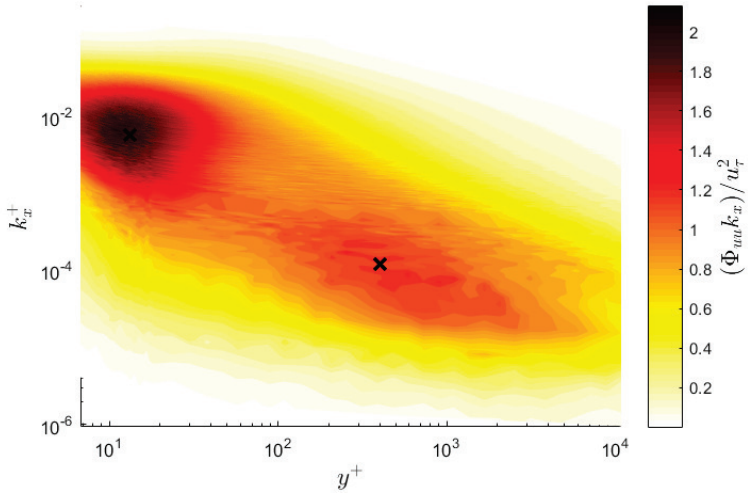

Figure 5.6: Contour plot of the pre-multiplied power spectral density of the streamwise velocity fluctuations for $Re_\tau \approx 3.8 \times 10^4$

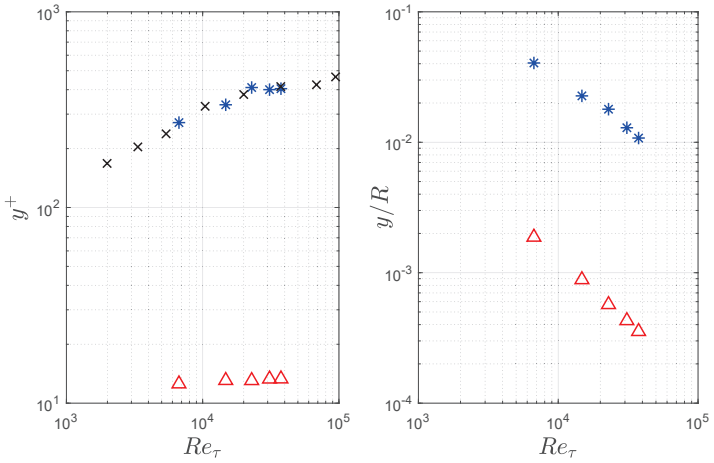

Figure 5.7: Wall-normal location of the spectral peaks in inner (left) and outer variables (right). △; inners spectral peak. ∗; outer spectral peak. ×; Pipe OSP from Vallikivi *et al.* (2015*a*).

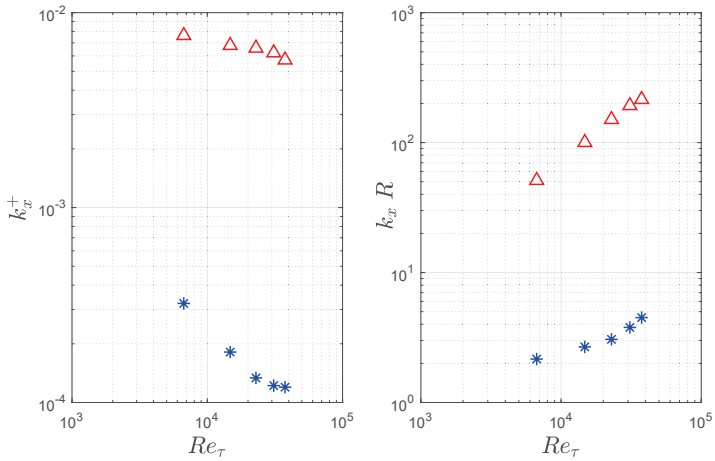

Figure 5.8: Wavenumber of the spectral peaks in inner (left) and outer variables (right). △; inners spectral peak. ∗; outer spectral peak.

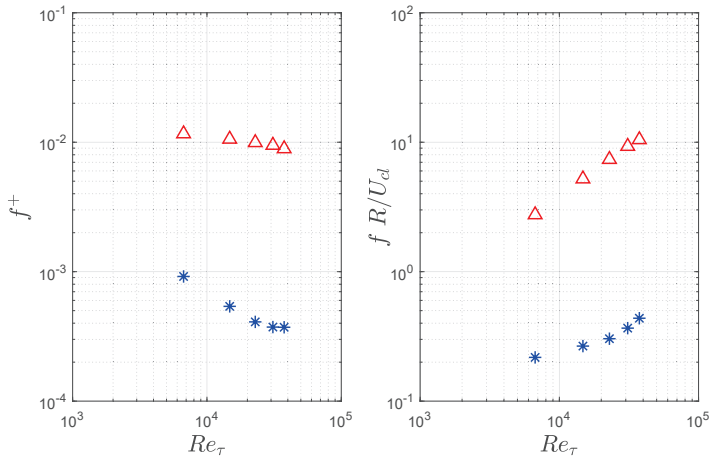

Figure 5.9: Frequency of the spectral peaks in inner (left) and outer variables (right). △; inners spectral peak. ∗; outer spectral peak.

Unsurprisingly, the inner spectral peak seems to scale very well in inner variables, while the outer spectral peak does not. Both peaks however do not scale on outer variables with even the outer spectral peak moving closer to the

wall in physical distance as the Reynolds number increases, and shifting towards higher outer-scaled wavenumbers. One possible interpretation is that the OSP, instead of being associated with a single characteristic coherent motion is the sum of different type of structures, some of which scale on outer variables and some don't.

In Fig. 5.10 and 5.11 are shown the power spectral densities corresponding to the location of the ISP and OSP for every Re_τ case. Note that the location might not be exactly the same as the one computed from the fitting procedure, instead the spectra at closest available hot-wire station is shown. By observing the spectra corresponding to the ISP locations, an attenuation of the magnitude of the spectra with Re_τ appears. Although according to the observations by Ng *et al.* (2011), the inner peak should remain almost constant, it should be taken into account that this region is likely to be affected by some spatial resolution issues, and for the cases examined here, L^+ is not constant. The trend seen could therefore be just an artefact of spatial filtering, but no established method for correction of the spectra exist. To asses spatial resolution effects on the spectra, the pre-multiplied power spectral densities are shown in Fig. 5.12 at the ISP location from different sensor length, and matching Re_τ cases. The peak attenuation with L^+ is clear in the high and intermediate wavenumber, while the different curves collapse at low wavenumbers. This produces an artificial shift of the spectra maximum at lower k_x that explains the behaviour observed in Fig. 5.9, thus it can be concluded that the position of ISP remains constant in inner units. A very important aspect to note is that the increase of u^{2+} with Re_τ shown in the previous chapter at this location ($y^+ \approx 15$) can now be clearly linked to the increase of energy at lower frequencies, which are not affected by spatial resolution. This is an important trend and it qualitatively matches the observation of Marusic *et al.* (2010*a*): at high Reynolds number, contribution of large structures to the turbulent kinetic energy becomes more and more relevant, even extremely close to the wall ($y^+ \approx 15$). Considering this, the 'failure' of inner scaling for the variance profile (increase of u^{2+} inner peak with Re_τ) appears an almost logical effect if the larger structures do not scale in inner variables.

In Fig. 5.11, the spectra corresponding to the locations of the OSP is shown. In this case the increase of area under the curves is evident and explains the increase of u^{2+} in this region (corresponding to the 'shoulder' of the variance profile); while the spectra tend to collapse at higher frequencies, the low frequency part extends with Reynolds number, which causes the OSP to move to lower f^+ values. Figure 5.13 shows that at the wall-normal location of the OSP, spatial resolution is not an issue in the present measurements.

Finally the magnitude of the ISP and OSP, as found from the fitting procedure and corresponding to the maximum of the fitted Gaussian, is plotted versus Reynolds number. Data is compared in Fig. 5.14 with the results of the analysis performed by Vallikivi *et al.* (2015*a*) on the Pipe data of Hultmark

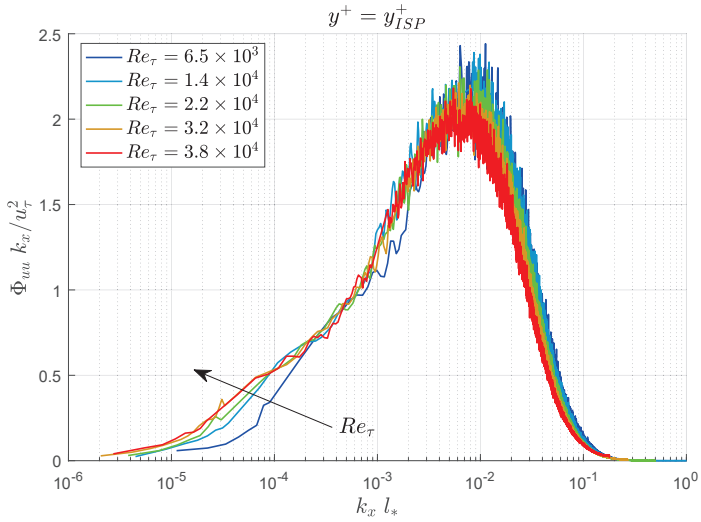

Figure 5.10: Pre-multiplied inner-normalized power spectral density at the location $y^+ = y^+_{ISP}$ for all Re_τ cases.

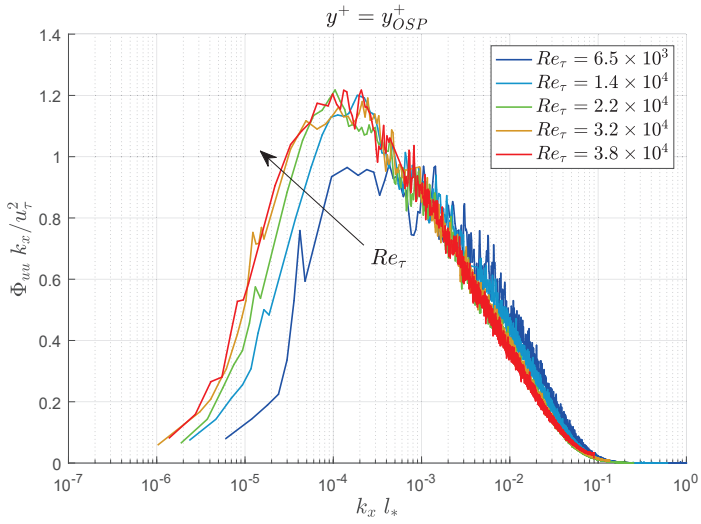

Figure 5.11: Pre-multiplied inner-normalized power spectral density at the location $y^+ = y^+_{OSP}$ for all Re_τ cases.

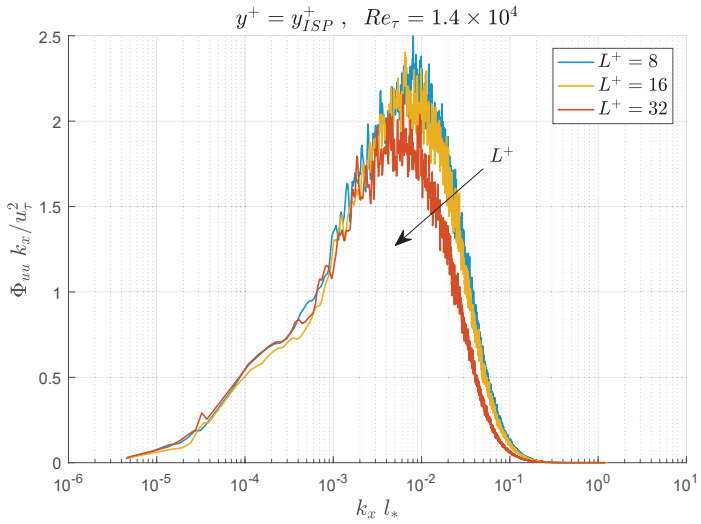

Figure 5.12: Pre-multiplied inner-normalized power spectral density at the location $y^+ = y^+_{ISP}$ for $Re_\tau = 1.4 \times 10^4$ and different sensor lengths.

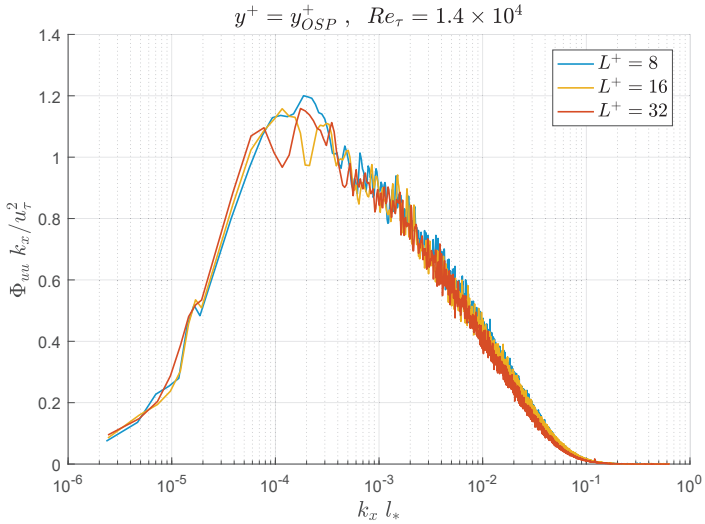

Figure 5.13: Pre-multiplied inner-normalized power spectral density at the location $y^+ = y^+_{OSP}$ for $Re_\tau = 1.4 \times 10^4$ and different sensor lengths.

et al. (2012). The outer spectral peak magnitude increases up to a a value ≈ 1.2 at $Re_\tau = 3.8 \times 10^4$; and agrees very well with Superpipe results despite the different peak location algorithm used, which testifies the robustness of the results. The magnitude of the outer spectral peak shows a decrease, although as already proved, this is caused by spatial filtering.

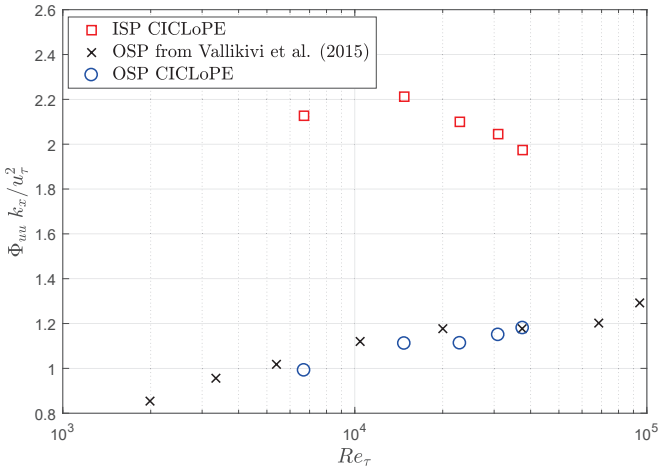

Figure 5.14: Magnitude of the pre-multiplied and inner-normalized spectral peaks as a function of friction Reynolds number.

5.2. Reynolds shear stress and quadrant analysis

In this section the streamwise and wall-normal velocity fluctuations measured with x-wire probes are analysed with the quadrant analysis technique. For a detailed review on quadrant analysis and its field of applicability the reader is referred to Wallace (2016). Quadrant analysis was first employed by Wallace *et al.* (1972), motivated by the desire to gain insight into the near wall streaks at the time observed by Kline *et al.* (1967), who used hydrogen bubbles as markers in water. Corino & Brodkey (1969) used a high-speed camera to record events in which the streaks slowed down and then erupted away from the wall, and other instances where large scale motions far from the wall moved towards it with a small angle; they called these events respectively ejections and sweeps. Wallace *et al.* (1972) realized the importance of sign for the streamwise and wall-normal fluctuations in describing the dynamics of these structures. They divided the (u, v) plane into four quadrants corresponding to different signs combinations of the velocity fluctuations: $Q_1(+u, +v)$, $Q_2(-u, +v)$, $Q_3(-u, -v)$ and $Q_4(+u, -v)$. With this method ejection-like events are in Q_2

while sweep-like events in Q_4. Willmarth & Lu (1972) computed the contributions to the total shear stress for each one of the quadrant and saw how important ejection and sweep events are for the production of Reynolds stress $\overline{uv}$. The shear stress is a key element of turbulence dynamics, because apart from appearing in RANS equation with the other Reynolds stress tensor elements, it appears also in the production term of the turbulent kinetic energy (TKE) equation, multiplied by the mean shear:

$$\mathcal{P} = -\overline{u_i u_j}\,\frac{d\overline{U_i}}{dx_j} \tag{5.5}$$

In Fig. 5.15 are shown the contour plots of the joint probability density functions (JPDF) of velocity's fluctuations $P(u, v)$. The JPDFs are taken at the closest location to $y^+ = 3\sqrt{Re_\tau}$ (indicative of the middle of the logarithmic region) for four Re_τ cases examined in the present measurements, normalized by their local standard deviations σ_u and σ_v. The iso-lines of the JPDFs exhibit an elliptical shape with the main axis crossing the 2nd and 4th quadrant and the JPDF maximum located just inside the fourth quadrant, with a longer tail towards the 2nd quadrant. This indicates the higher number of $uv(t) < 0$ events, with in particular the 2nd quadrant (associated with ejections) being characterized by more extreme events, with a higher value of $|uv(t)|$. The probability density functions of streamwise and wall-normal fluctuations, f_u and f_v, are shown In Fig. 5.16 for $Re_\tau = 2.2 \times 10^4$. Note that f_v is skewed towards negative values while f_u is slightly skewed towards positive ones.

5.2.1. *Contribution to the total shear stress*

In order to compute the contribution that events from the Q_i quadrant have on the mean Reynolds shear stress $\overline{uv}$ acquired over a finite acquisition time T_{tot}, the (u, v) plane can be divided as shown in Fig. 5.17, following the analysis by Lu & Willmarth (1973). Of particular importance here are the quadrant Q_2 and Q_4, that can be associated with the ejection-like and sweep-like events previously described. In the central part of the plane, a 'hole' region can be defined, delimited by $|uv| = const$ curves. The extension of this region can be defined by a hole parameter H, so that a point in the (u, v) plane is located inside the hole if:

$$|uv| < H\sigma_u\sigma_v \tag{5.6}$$

with σ_u and σ_v being the local root mean square of u and v fluctuations. Most of the times $|uv|$ is small, as can be seen from the JPDFs shown in the previous section, Where higher values $P(u, v)$ are found near the plane origin. By modulating the magnitude of the parameter H, more or less extreme events can be taken into account when performing the analysis. Turbulence

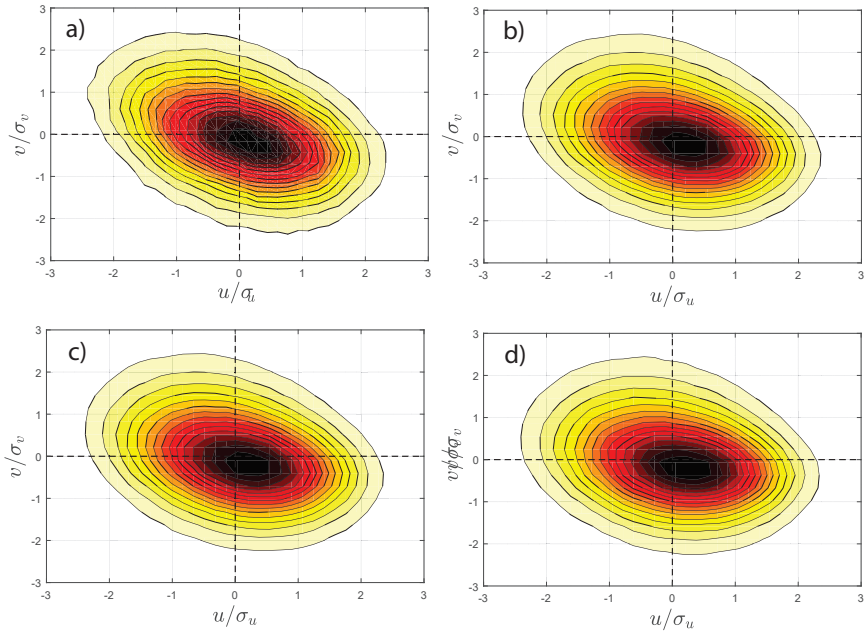

Figure 5.15: JPDF of streamwise and wall-normal velocity fluctuations u and v, normalized by their local root mean squares, at $y^+ = 3\sqrt{Re_\tau}$. a)$Re_\tau = 6.5 \times 10^3$. b)$Re_\tau = 1.4 \times 10^4$. c)$Re_\tau = 2.2 \times 10^4$. d)$Re_\tau = 3.8 \times 10^4$.

exhibits a highly intermittent nature and extreme events, although rare, play an important role in the production of total Reynolds shear stress.

To compute the contribution of quadrant Q_i to the total Reynolds shear stress, that will be indicated as $\widetilde{uv}_i$, the following can be used:

$$\frac{\widetilde{uv}_i}{\overline{uv}} = \frac{1}{\overline{uv}} \frac{1}{T} \int_0^T uv(t)\, \chi_i(t, H)\, dt \tag{5.7}$$

With $\chi_i(t, H)$ being a function of the ith quadrant, the time t and the hole size parameter H:

$$\chi_i(t, H) = \begin{cases} 1 & \text{if } uv(t) \in Q_i \text{ and } |uv(t)| \geq H\sigma_u\sigma_v \\ 0 & \text{otherwise} \end{cases} \tag{5.8}$$

similarly, a contribution from the hole region $\widetilde{uv}_h$ can be calculated, with $\chi_h(t, H)$ in place of $\chi_i(t, H)$ in expression (5.7):

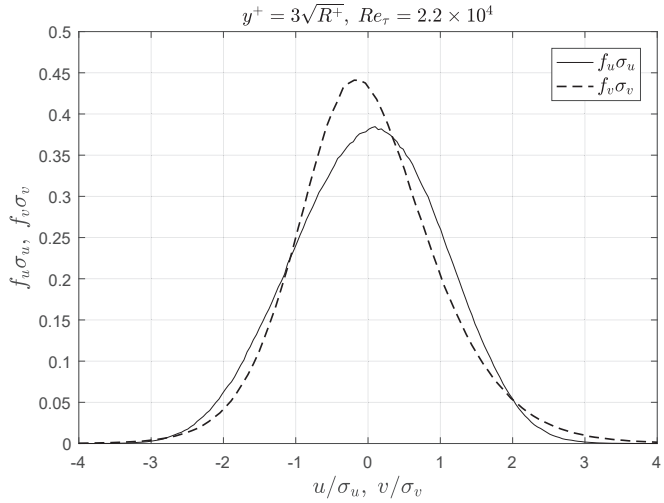

Figure 5.16: Probability density functions of streamwise and wall-normal fluctuations for $Re_\tau = 2.2 \times 10^4$ and $y^+ = 3\sqrt{Re_\tau}$.

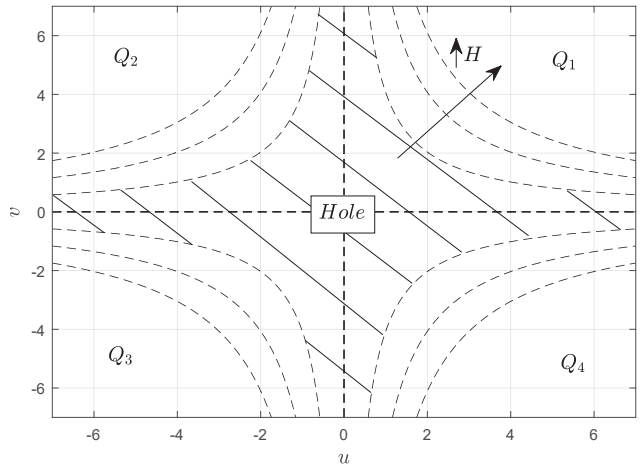

Figure 5.17: Schematic of the (u, v) plane and its subdivision in four quadrants and a central hole region.

$$\chi_h(t, H) = \begin{cases} 1 & \text{if } |uv(t)| < H\sigma_u\sigma_v \\ 0 & \text{otherwise} \end{cases} \tag{5.9}$$

it is important to note that, due to their definitions, the sum of contributions from all the quadrants and the hole region must result in the mean Reynolds shear stress $\overline{uv}$:

$$\widetilde{uv}_h + \sum_{i=1}^{4} \widetilde{uv}_i = \overline{uv} \tag{5.10}$$

Although the previous definitions have been given for $uv(t)$ a continuous function of time, the result of the acquisition process in an experiment is a discrete series of uv_j samples. In practice, when dealing with discrete and not continuous time-series, instead of eq. (5.7), the following is used:

$$\frac{\widetilde{uv}_i}{\overline{uv}} = \frac{1}{\overline{uv}} \frac{1}{N} \sum_{j=1}^{N} uv_j \; \chi_i(j, H) \tag{5.11}$$

Where N is the total number of acquired samples and uv_j is the jth sample of the discrete series. In Fig. 5.18 the contributions $\widetilde{uv}_i$ are shown as a function of the hole size parameter for $Re_\tau = 2.2 \times 10^4$ and $y^+ = 3\sqrt{Re_\tau}$. As can be expected, when the hole size is increased the absolute value of the contributions from all the quadrants tend to zero, while the hole contribution Q_h approaches one. It should be noted that due to their definitions, contributions can be negative as is the case for Q_1 and Q_3, that are characterized by positive values of $uv(t)$.

The fundamental point to outline here is that, while the behaviour of contributions from Q_3 and Q_1 are almost identical, a clear difference can be pointed out for the second and fourth quadrants. As already noticed by Lu & Willmarth (1973), ejections-like events of the Q_2 quadrant contribute substantially more to $\overline{uv}$ than the sweep-like events of Q_4. The scaling of this contributions with varying Reynolds number is displayed in Fig. 5.19, where results from the highest and lowest Re_τ cases are shown together for the same reference wall-normal location, $y^+ = 3\sqrt{Re_\tau}$.

For the sake of clarity in the figure, only these two Reynolds number cases are shown. Normalized contributions from all quadrants are increased in their absolute value with Re_τ, both the positive contributions from Q_2 and Q_4 and the negative ones from Q_1 and Q_3; in particular $\widetilde{uv}_3$ and $\widetilde{uv}_1$ nearly double while $\widetilde{uv}_2$ and $\widetilde{uv}_4$ increase by roughly $15 - 20\%$. On the other hand, the hole contribution $\widetilde{uv}_h$ remains practically unchanged. One interpretation of this could be that, at this reference location with increasing Re_τ, the normalized JPDF 'spreads' over a wider area of the (u, v) plane, and does more so in the $Q_3 - Q_1$ direction that the $Q_2 - Q_4$ one. In other words, also relatively 'extreme' $uv(t) > 0$ events start to become more common, this is clearly visible in the PDF of $uv(t)$, shown in Fig. 5.20. As Reynolds number is increased the tails of

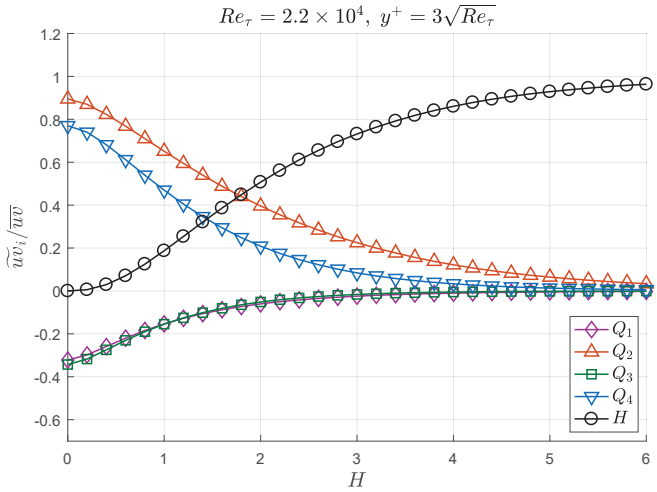

Figure 5.18: Contributions $\widetilde{uv}_i$ to the Reynolds shear stress $\overline{uv}$ normalized by the local value of the shear stress as a function of the hole size parameter H. For $Re_\tau = 2.2 \times 10^4$.

the PDF widen, and this is particularly noticeable for $uv(t) > 0$. Another thing to be noticed is that the contribution from Q_4 collapse for different Reynolds number after approximately $H > 1.5$. This indicates that while contributions from both sweep and ejection events increase with Re_τ, for sweeps this growth is mainly due to relatively weaker events ($|uv| < 1.5\ \sigma_u\sigma_v$) when compared to ejections, where the increase with Reynolds number is noticeable up to higher values of the parameter H.

The same analysis can be carried out for varying wall-normal locations, shown in Fig. 5.21 for $Re_\tau = 2.2 \times 10^4$. It should be remembered that given the limitations in the traversing/probe set-up, only measurements in the $200l_* < y < 0.3R$ range are available for this Reynolds number. Nonetheless some trends can still be extracted from the figure.

Trends from the contributions of Q_1, Q_3, Q_4 and Q_h with decreasing wall distance are qualitatively similar to the behaviour for increasing Reynolds number, with the hole contribution remaining practically unchanged and all the others growing in absolute value. The ejection contribution on the other hand, displays a particular behaviour: with decreasing wall-normal distance in inner units, the $\widetilde{uv}_2$ term increases for $H < 1$ but decreases for $H > 1$. Which means that while the overall Q_2 quadrant contribution increases moving towards the wall, stronger ejections events ($H > 1$) are less likely to be detected at the start of the logarithmic region ($y^+ \approx 200$) rather than at its outer edge ($y \approx 0.3\,R$).

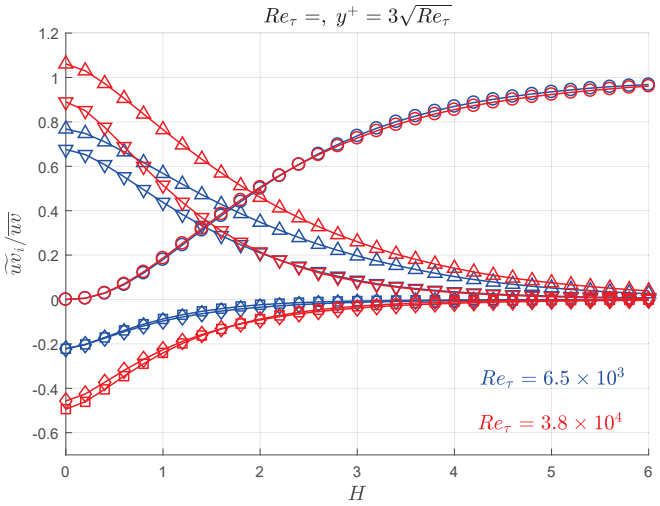

Figure 5.19: Contributions $\widetilde{uv}_i$ to the Reynolds shear stress $\overline{uv}$ normalized by the local value of the shear stress as a function of the hole size parameter H at $y^+ = 3\sqrt{Re_\tau}$. In red is displayed the highest Re_τ from present data, while in blue the lowest.

To reduce the number of variables in the analysis, a value for the hole size can be fixed at $H = 1$, and the Re_τ and y^+ dependency can be simultaneously examined. If we consider the ratio between the contribution from sweeps and ejections events, $\widetilde{uv}_2/\widetilde{uv}_4$, we can plot it as a function of wall distance for the different Reynolds numbers, as in Fig. 5.22

The ratio is plotted both in inner and outer units, and it can be observed how the different Re_τ curves collapse fairly well on a linear trend when plotted in inner units. The contribution from ejection events becomes gradually more dominant with respect to the sweeps as we move away from the wall, with a value that becomes 70% greater than $\widetilde{uv}_4$ at $y = 0.3\,R$.

5.2.2. *Quadrant residence time*

To complement the previous results, a similar analysis to the shear stress contribution can be performed considering the time out of the total acquisition time T_{tot}, for which $uv(t)$ 'resides' in a particular quadrant. We call this the residence time of Q_i quadrant, T_{Qi}. That can be computed with the following:

$$\frac{T_{Qi}}{T_{tot}} = \frac{1}{T_{tot}} \int_0^{T_{tot}} \chi_i(t, H)\, dt \tag{5.12}$$

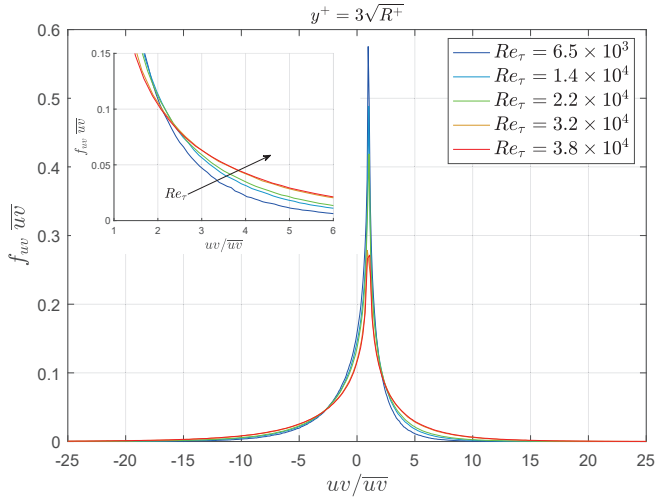

Figure 5.20: Probability density functions of $uv(t)$ for all Reynolds number cases.

where $\chi_i(t, H)$ is the same function defined in eq. (5.8). The sum of each residence time must then equal the total acquisition time:

$$T_{Qh} + \sum_{i=1}^{4} T_{Qi} = T_{tot} \tag{5.13}$$

Just like for the shear stress contribution $\widetilde{uv}_i$, the experimental data is a discrete time series uv_j with $j = 1...N$, so that the residence time can simply be calculated instead with:

$$\frac{T_{Qi}}{T_{tot}} = \frac{1}{N} \sum_{j=1}^{N} \chi_i(j, H) \tag{5.14}$$

In Fig. 5.23 the residence time of every quadrant, normalized by the total acquisition time is plotted as a function of the hole size parameter H, for the highest and lowest $Re_\tau = 2.2 \times 10^4$ and $y^+ = 3\sqrt{Re_\tau}$.

One difference that can be immediately noticed in comparison with the $\overline{uv}$ contributions shown in Fig. 5.18, is the sharper increase in T_{Qh} with H. For $H = 1$, $uv(t)$ is found inside the hole region 80 % of the time, compared with less than 10 % for Q_2 - Q_4 and around 1% for Q_1 - Q_3. This means that most of the time the $uv(t)$ is 'quiescent' and loiters around the origin of the (u, v) plane. An interesting thing to add is that residence time from Q_2 and Q_4 are

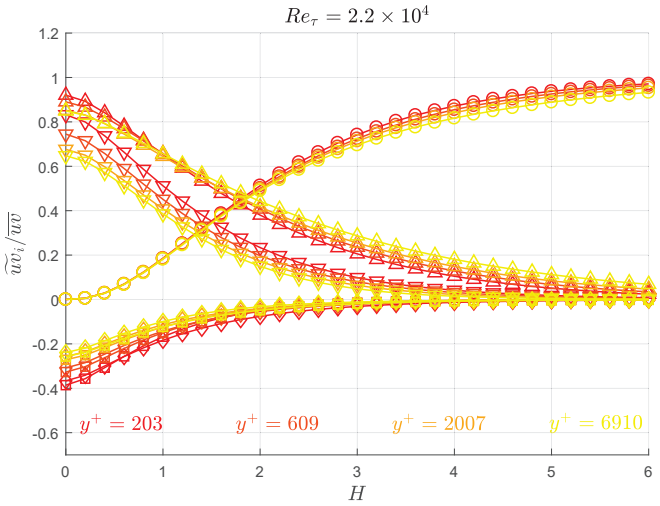

Figure 5.21: Contributions $\widetilde{uv}_i$ to the Reynolds shear stress $\overline{uv}$ normalized by the local value of the shear stress as a function of the hole size parameter H at different wall-normal distances from the wall. Symbols are the same as those in Fig. 5.18. In red is shown the lowest value of y^+ while in yellow the highest. For $Re_\tau = 2.2 \times 10^4$.

almost identical with the noticeable difference that for low values of H T_{Q4} is slightly bigger, while the opposite occurs as the hole size is increased. This is a confirmation of what already noticed with $\overline{uv}$ contributions: Q_4 events are the more common than Q_2 ones, but as we start neglecting weak events by increasing H, ejection-like events become predominant. The variation of the residence times with Reynolds number and wall distance is shown rspectively in Fig. 5.24 and 5.25.

It can be observed how residence time are a lot less affected by the location and Reynolds number compared to the $\overline{uv}$ contributions. Only very small variations can be distinguished: T_{Q2} - T_{Q4} become slightly smaller and T_{Q1} - T_{Q3} slightly bigger with increasing Reynolds number, this is the same effect that was previously noticed and described as a 'spreading' of the JPDF in the Q_1 - Q_3 direction.

Residence time ratio between the second and the fourth quadrants are plotted, for $H = 1$, in Fig. 5.26. The overall behaviour is very similar to the contribution's ratio shown in Fig. 5.22, with a linear increase and a good collapse in inner units.

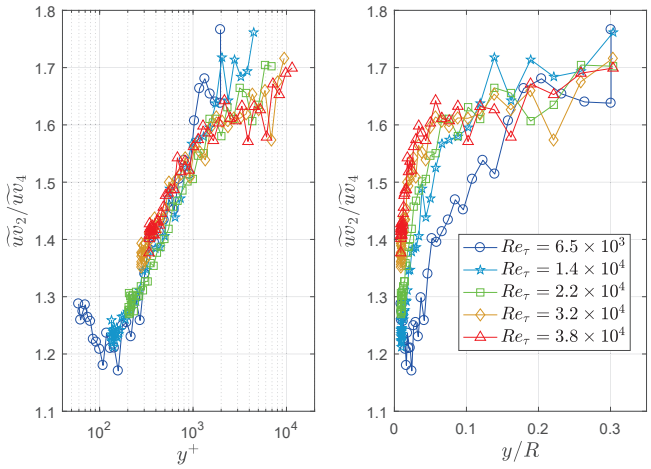

Figure 5.22: Ratio of contribution from ejection-like to sweep-like events for a fixed hole size $H = 1$. As a function of wall-normal distance.

Overall the most important observation that can be made looking at residence times is that, while for a hole size parameter $H = 1$ the $uv(t)$ signal spends $\approx 80\%$ of the total time in the hole region, when observing Fig. **??** the contribution to the total Reynolds shear stress $\widetilde{uv}_h$ remains very modest with $\approx 20\%$ of the total $\overline{uv}$. This underlines the strongly intermittent behaviour of Reynolds stress production in wall turbulence, with most of it being produced in sudden and strong events.

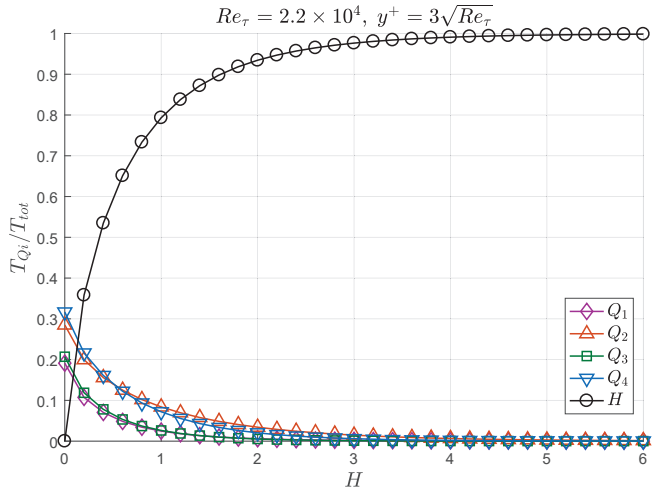

Figure 5.23: Residence times T_{Qi} normalized by the total acquisition time T_{tot} as a function of the hole size parameter H at $y^+ = 3\sqrt{Re_\tau}$ for $Re_\tau = 2.2 \times 10^4$.

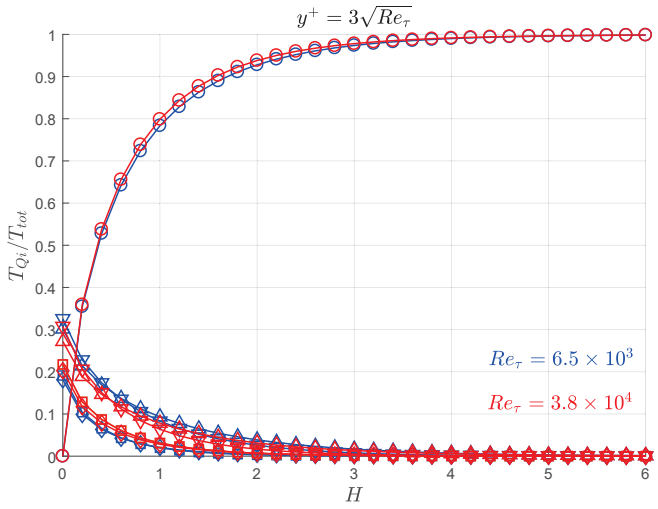

Figure 5.24: Residence times T_{Qi} normalized by the total acquisition time T_{tot} as a function of the hole size parameter H at $y^+ = 3\sqrt{Re_\tau}$. In red is displayed the highest Re_τ of present measurements, while in blue the lowest. Symbols are the same as those in Fig. 5.23.

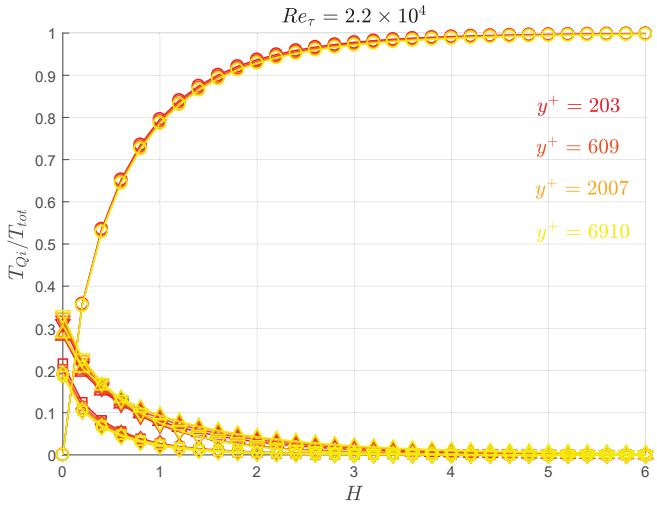

Figure 5.25: Residence times T_{Qi} normalized by the total acquisition time T_{tot} as a function of the hole size parameter H at different wall-normal locations y^+. In red is shown the lowest value of y^+ while in yellow the highest. Symbols are the same as those in Fig. 5.23.

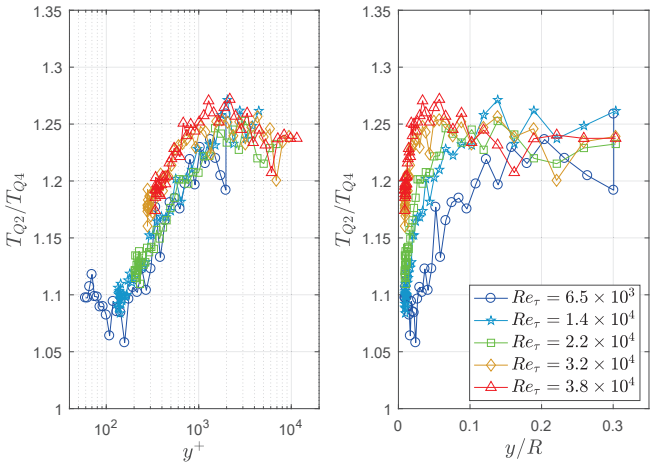

Figure 5.26: Ratio of residence times from ejection-like to sweep-like events for a fixed hole size $H = 1$. As a function of wall-normal distance.

CHAPTER 6

Conclusions

The aim of the thesis was to expand our current understanding of wall-bounded turbulence at high Reynolds number, a problem extremely common in engineering and environmental applications. In order to do so, an experimental study was carried out in the new Long Pipe facility at the CICLoPE laboratory of the University of Bologna. The facility is unique in its kind as it provides the access to high Reynolds number wall turbulence with a degree of resolution that can not be found elsewhere. The thesis includes a characterization of the flow in the novel facility, as well as a detailed analysis of the experimental data acquired, in order to gain information on the behaviour of high Reynolds number turbulence. The bulk of experimental results presented comes from high-resolution measurements with custom-built single and x-wire probes performed for a Reynolds number range of $6500 < Re_\tau < 38000$ in a fully developed pipe flow. Summarizing the main results:

- A characterization of the facility has been carried out, to ensure the proper operation of the wind tunnel and the canonical flow conditions in the test section, through measurements involving static pressure, temperature, mean and fluctuating velocity. The results show that the wind tunnel provides a stable flow condition in terms of velocity and temperature across its operational range. The flow was found to be symmetrical at different regimes, the measured velocity spectra and statistical moments at the centreline are typical of a fully developed pipe flow. The pressure drop and wall-friction were carefully assessed and a detailed analysis was performed in order to decide the suitable range over which to apply the fit for τ_w determination. An uncertainty estimation was given based on the uncertainty of the fit. The mean streamwise velocity shows a clear logarithmic behaviour, with a value of the von Kármán constant $\kappa \approx 0.4$ from fitting of the profile data points. While this value is lower than some previously reported values from the Superpipe, $\kappa = 0.438$ by Zagarola & Smits (1998) and $\kappa = 0.421$ by Mckeon *et al.* (2004), it is qualitatively in agreement with more recent analysis by Bailey *et al.* (2014), that concluded $\kappa = 0.40 \pm 0.02$ from previous Superpipe data using both velocity profile fitting and bulk properties. The value found here is however higher than values recently reported

by Furuichi *et al.* (2015) $\kappa = 0.385 - 0.382$ in pipe flow and the one reported for boundary layers ($\kappa = 0.38$) by Österlund *et al.* (2000) and in channel ($\kappa = 0.37$) by Monty (2005).

- One of the focus of the investigation was the scaling of velocity fluctuations, and Reynolds stresses in particular, that can greatly benefit from the high resolution granted by the facility. Different wire length were also used in the measurements to explore the effects of spatial resolution. The streamwise normal stress u^{2+} velocity was examined in detail. When corrected with the scheme proposed by Smits *et al.* (2011*b*), the near-wall peak of the inner-normalized variance of the streamwise velocity shows a clear increasing trend with Re_τ, as such confirming results from lower Reynolds number DNS and experiments (Örlü & Alfredsson (2013)), but at odds with results from Superpipe by Hultmark *et al.* (2012). In addition, in the present measurements no clear outer peak of the streamwise stress is observed up to highest Reynolds number investigated ($Re_\tau = 3.8 \times 10^4$). The shoulder of the profile assumes instead a plateau behaviour, whose magnitude agrees very well with the reported value of the outer peak in Superpipe. A comparison of the profiles show additional attenuation of the Superpipe streamwise stress closer to the wall, which might point out to spatial filtering unaccounted by the correction scheme. The data qualitatively supports the attached eddy model (Townsend (1976)) by displaying a region of logarithmic behaviour in outer scaling for the streamwise stress, with a Townsend-Perry constant ≈ 1.26. The wall-normal, spanwise and shear stress were also measured with an x-wire probe. The results show again a good agreement with the predictions of the attached eddy model: the spanwise normal stress shows a logarithmic behaviour with a slope half that of the streamwise stress, and the wall-normal stress exhibits a constant plateau.

- The signature of coherent motions was analysed via spectral analysis. On the power spectral density map an inner and an outer spectral peak were identified. Their scaling has been explored and results are found to be in general good agreement with Vallikivi *et al.* (2015*a*). While the inner spectral peak (ISP) scales on inner units and shows a constant magnitude, the outer spectral peak moves away from the wall in inner units as the Reynolds number is increased, but closer to the wall in physical units, suggesting a sort of mixed scaling. Furthermore the magnitude of the outer spectral peak (OSP), that can associated with large scales in the logarithmic region, increases with increasing Reynolds number, becoming more and more relevant. The analysis of the premultiplied spectra at the ISP location confirms the increasing trend of streamwise variance's inner peak and shows how the increase is related

to low-frequency and large-scale motions, that extends their influence down to the wall.

- The Reynolds shear stress was analysed in conjunction with near-wall events such as ejections and sweeps. Quadrant analysis (Wallace (2016)) was performed on x-wire measurements. The analysis focus on events in the near wall region such as ejections (movement of slower fluid away from the wall) and sweeps (movement of faster fluid from the log-region towards the wall). The results show the fundamental role that these events have in the production of Reynolds shear stress $\overline{uv}$, and their highly intermittent nature, true in particular for ejection-like events. This agrees well with what was found by Lu & Willmarth (1973) in boundary layer, but thanks to the larger range of measurements locations and Re_τ values for the present data-set, it was possible to study the scaling of these events. In particular, it is shown how with increasing Reynolds number the contribution of these events on the total shear stress increases, and they tend to intensify their highly intermittent nature, particularly true in the case of ejections. An interesting point is that the ratio of contribution to the shear stress from ejection and sweeps is found to increase logarithmically with the distance from the wall, up to 1.7 at $y/R = 0.3$, and collapse in inner units for different Re cases.

Overall, this first experimental campaign in the Long Pipe facility has produced a rich data-set of highly resolved wall-turbulence data. These are the best resolved measurements at these Reynolds numbers currently available using traditional hot-wire sensors in a laboratory flow. Results from the first analysis carried out on the data has given precious insight on high Reynolds number wall turbulence and has (at least in the opinion of the author) settled some long-lasting controversy on the scaling of turbulence quantities, such as the inner peak of the streamwise normal Reynolds stress. Surely in the future valuable results will continue to be produced, both from further analysis of this data-set as well as the currently ongoing experimental activities in the facility.

APPENDIX A

Uncertanty estimation

In this appendix the uncertainty on the measured statistical moments of the first and second order will be analysed. The sources of error considered are the uncertainty introduced during calibration, the statistical uncertainty of the measurements and the uncertainty in friction velocity determination.

A.1. Calibration uncertainty

Uncertainty introduced by calibration is a random error that is "fossilized" in the calibration curve and behaves as a fixed error (bias) during velocity measurements. The assumption is made that the only uncertainty present during calibration is on the value of velocity measured with a Pitot total pressure probe, placed in the calibration jet next to the hot-wire. The accuracy and resolution of hot-wire voltage measurement is deemed sufficient and neglected from the analysis. Furthermore, since calibration is carried out at the exit of a jet, in a laminar and uniform flow, no statistical uncertainty will be considered for the calibration. Velocity of a calibration point is determined by measuring the difference between static and total pressure with a Prandtl tube, which equals the dynamic pressure $p_d = 0.5\,\rho\,U^2$:

$$U = \sqrt{\frac{2\,p_d}{\rho}} \tag{A.1}$$

the fluid density ρ is computed through an ambient pressure and temperature measure, using the ideal gas law, $\rho = p_{amb}/R_g T$. Where R_g is the specific ideal gas constant and T is the gas temperature in Kelvin.

$$U = \sqrt{\frac{2\,\Delta p\,R_g\,T}{p_{amb}}} \tag{A.2}$$

Following Yavuzkurt (1984), the total uncertainty on velocity in the calibration, ΔU, can be computed using the uncertainties on temperature, dynamic pressure and ambient pressure:

$$\Delta U = \sqrt{\left(\frac{\partial U}{\partial p_d}\Delta p_d\right)^2 + \left(\frac{\partial U}{\partial T}\Delta T\right)^2 + \left(\frac{\partial U}{\partial p_{amb}}\Delta p_{amb}\right)^2} \tag{A.3}$$

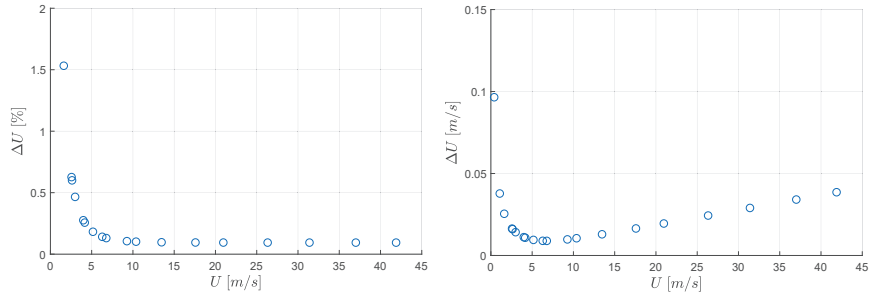

Figure A.1: Left: absolute uncertainty of an example calibration velocity data. Right: relative uncertainty.

The instrument used for temperature measurement is the same PT100 thermistor used in the test chamber during profile acquisition, with a rated accuracy of $\Delta T = \pm 0.20\ ^{\circ}C$ at $20\ ^{\circ}C$. Ambient and dynamic pressure are measured respectively with a MKS 120AA and 120AD pressure transducers, both with a reported accuracy of ± 0.12 % of the reading. However, the voltage output of the transducers is digitalized through a five-digit reading unit, as such the resolution uncertainty introduced by the reading unit must also be accounted for. Uncertainty due to resolution for dynamic pressure is $\pm 0.05\ Pa$. For ambient pressure, resolution uncertainty is $\pm 5\ Pa$. The total uncertainty for pressure measurements is therefore given by:

$$\Delta p = \sqrt{\Delta p_{acc}^2 + \Delta p_{res}^2} \tag{A.4}$$

where Δp_{acc} is the uncertainty due to the transducer accuracy and Δp_{res} is the one due to the reader's resolution. The absolute and relative uncertainty on velocity for an example calibration are shown in Fig. A.1. As can be seen, at low velocity the uncertainty increases, due to the error introduced by the reader's resolution.

At this point, error bars can be added to each calibration point on the velocity axis. In fig. A.2 an example calibration is shown. In order to study the effects on the fitted calibration curve, two 4th order polynomial are fitted through the calibration velocity data points, respectively $U + \Delta U$ and $U - \Delta U$. These 'distorted' calibration curves can then be used to compute the statistics, as shown in Fig. A.3 and A.4 for the lowest and highest flow speed case.

A.2. Statistical uncertainty

During data acquisition, an additional source of uncertainty on the measured statistics is given by the randomness of the process. Acquiring for a finite time period T results in a computed mean and variance value that are not the 'true'

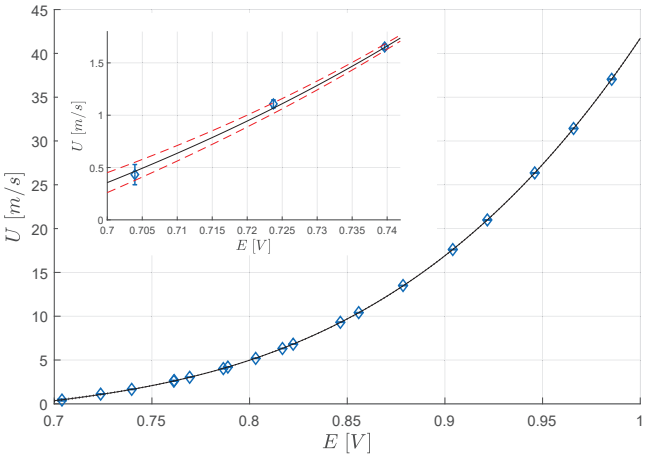

Figure A.2: Example hot wire calibration curve with displayed the uncertanty on velocity. In the insert the error-bars at lower velocities are visible. — ; 4th order polynomial calibration curve. - - ; calibration curves considering $\pm\Delta U$.

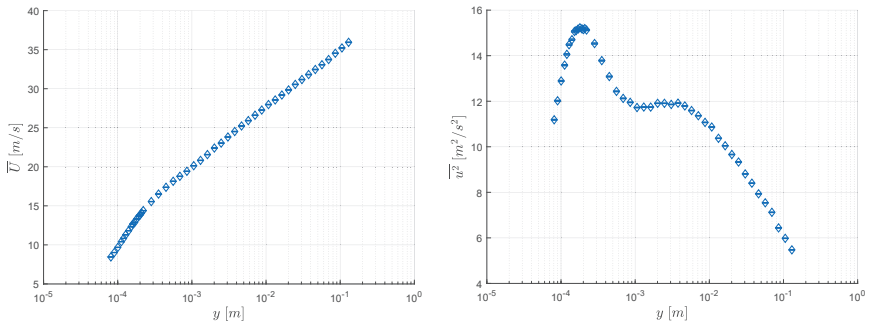

Figure A.3: Effects of calibration uncertainty on the measured velocity mean and variance, for $Re_\tau = 3.8 \times 10^4$.

value of the population, instead they are referred to as the sample mean and sample variance. For a normally-distributed process $U(t)$ the sample mean $\overline{U}$ obtained from N statistically independent samples is within a certain range of the real population mean μ_U:

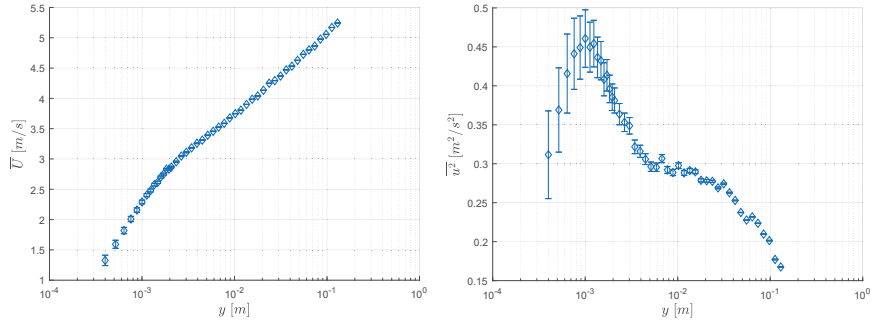

Figure A.4: Effects of calibration uncertainty on the measured velocity mean and variance, for $Re_\tau = 3.8 \times 10^4$.

$$\overline{U} - t_{-\alpha/2}\frac{\sqrt{\overline{u^2}}}{\sqrt{N}} < \mu_U < \overline{U} + t_{\alpha/2}\frac{\sqrt{\overline{u^2}}}{\sqrt{N}} \tag{A.5}$$

where $t_{\alpha/2}$ is the value of the t-distribution for the chosen confidence interval $100(1-\alpha)$ and $N-1$ degrees of freedom. Similarly, the true population variance σ_U^2 is within a certain range of the sample variance $\overline{u^2}$, given by:

$$\frac{(N-1)\overline{u^2}}{\chi^2_{\alpha/2}} < \sigma_U^2 < \frac{(N-1)\overline{u^2}}{\chi^2_{1-\alpha/2}} \tag{A.6}$$

where χ^2_α is the chi-squared distribution, that the sample variance $\overline{u^2}$ of a normally distributed variable $U(t)$ assumes. Selecting a 95% confidence interval, the statistical uncertainty of the mean and variance can be computed, given the number of statistically independent samples N.

A sample is considered to be statistically independent from another only if it is acquired after two integral time lengths, when the process is considered to be uncorrelated with its previous value. Given a total acquisition time T, and an integral time length Λ_t, estimated from the autocorrelation function $\rho_{uu}(\tau)$ as reported in eq. (1.22), the number of independent samples is then given by:

$$N = \frac{T}{2\,\Lambda_t} \tag{A.7}$$

Instead of computing the integral time-scale from the autocorrelation function, an estimate using the local mean velocity can be used:

$$\Lambda_t(y) = R/\overline{U}(y) \tag{A.8}$$

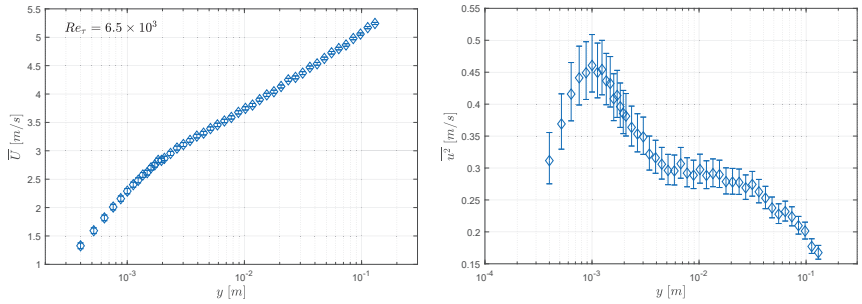

Figure A.5: Statistical uncertainty on the velocity mean and variance for $Re_\tau = 6.4 \times 10^3$. Acquisition time is $T = 160$ s for each point.

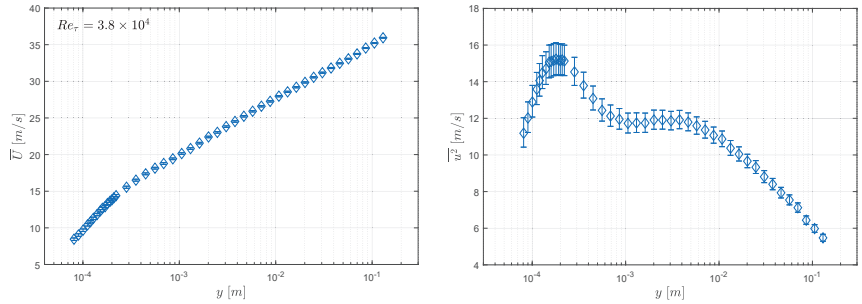

Figure A.6: Statistical uncertainty on the velocity mean and variance for $Re_\tau = 3.8 \times 10^4$. Acquisition time is $T = 80$ s for each point.

where R is the pipe radius. The resulting statistical uncertainties on the velocity mean and variance are shown in figure A.5 - A.6 for the highest and lowest case of Reynolds number investigated in the present measurements. Despite the longer acquisition time employed for the lower Re_τ case (160 seconds against 80) the uncertainty is more noticeable at lower speed.

A.3. Friction velocity uncertainty

Friction velocity is determined through the pressure wall friction which, in turn, is calculated by fitting the static pressure drop along the pipe with the procedure detailed in chapter 3.

$$u_\tau = \sqrt{\frac{\tau_w}{\rho}} \tag{A.9}$$

the fluid density ρ is calculated in the same way as for the hot-wire calibration, with a measure of temperature and ambient pressure:

$$u_\tau = \sqrt{\frac{\tau_w \; R_g \; T}{p_{amb}}} \tag{A.10}$$

hence the total uncertainty on u_τ becomes:

$$\Delta u_\tau = \sqrt{\left(\frac{\partial u_\tau}{\partial \tau_w}\Delta\tau_w\right)^2 + \left(\frac{\partial u_\tau}{\partial T}\Delta T\right)^2 + \left(\frac{\partial u_\tau}{\partial p_{amb}}\Delta p_{amb}\right)^2} \tag{A.11}$$

While ΔT and Δp_{amb} are easily found as the instruments reported accuracy; $\Delta\tau_w$ is less immediate, as the wall friction is found through the static pressure drop along the pipe. The sources of uncertainties affecting the pressure drop measurements are the random errors due to the accuracy of the pressure scanner ($\pm 1.25\ Pa$) and the statistical convergence. Since the pressure drop is acquired during the whole profile acquisition, consisting in over thirty points, the uncertainty is dominated by the pressure scanner accuracy, while the statistical uncertainty is negligible. In Fig. A.7a the static pressure measured along the pipe is shown, with error-bars representing the reported accuracy of the pressure scanner.

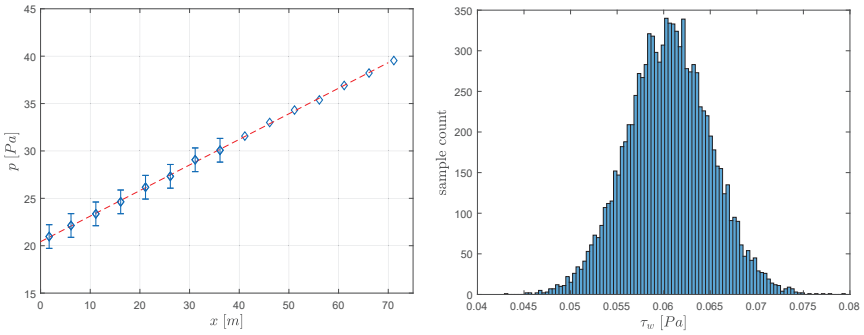

Figure A.7: . Left: Right:

In order to estimate the resulting uncertainty on pressure gradient and τ_w, a normally distributed error of $\pm 1.25\ Pa$ (with a 95 % confidence interval) was added to the measured data in a series of repeated simulations; each time the wall-friction was computed from the 'distorted' data. Obtaining a distribution of sample τ_w with standard deviation σ_{τ_w}, shown in Fig. A.7b, from which $\Delta\tau_w$ can be computed as $1.96\ \sigma_{\tau_w}$.

The total uncertainty on u_τ can be computed with (A.11). The effects of u_τ uncertainty on inner-scaled mean and variance profiles are shown in Fig. A.8 - A.9, for the lowest and highest Reynolds number case.

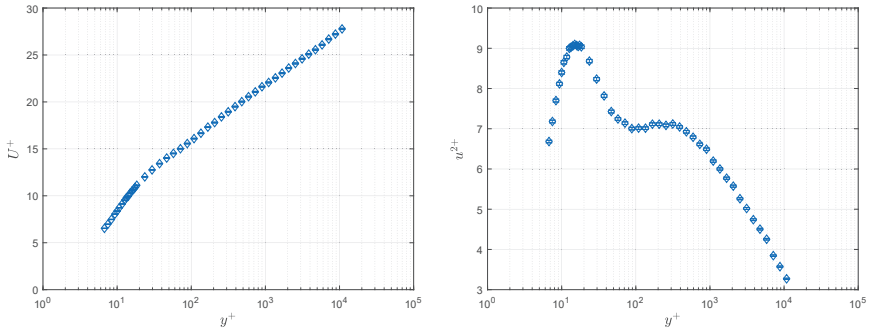

Figure A.8: Effects of u_τ uncertainty on the measured velocity mean and variance, for $Re_\tau = 3.8 \times 10^4$.

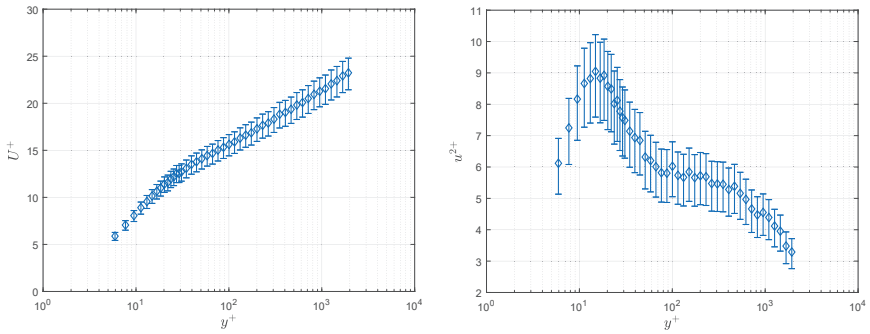

Figure A.9: Effects of u_τ uncertainty on the measured velocity mean and variance, for $Re_\tau = 6.5 \times 10^3$.

As can be seen, the uncertainty on u_τ greatly impacts the low speed case, it is almost absent in the high Reynolds number case, where the $\pm 1.25\ Pa$ uncertainty of the pressure scanner becomes negligible.

A.4. Effect of global uncertainty

Here the combined effects of the uncertainty sources investigated in the previous sections are shown. Given uncertainties on the measured inner-scaled mean

velocity given by calibration, acquisition time and friction velocity, (referred respectively as $\Delta\overline{U}_{cal}$, $\Delta\overline{U}_{stat}$ and $\Delta\overline{U}_{u_\tau}$), the global uncertainty can be found as:

$$\Delta\overline{U} = \sqrt{\Delta\overline{U}_{cal}^2 + \Delta\overline{U}_{stat}^2 + \Delta\overline{U}_{u_\tau}^2} \tag{A.12}$$

One dataset will be used as example, as the global uncertainty is essentially determined by the acquisition time and Reynolds number case, and does not vary between different hot-wire sensors.

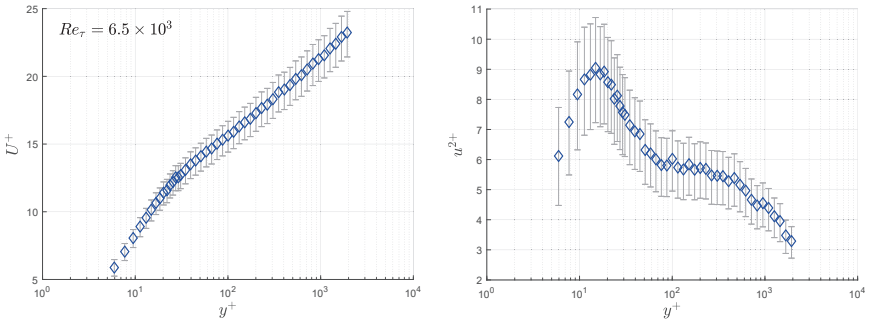

Figure A.10: Effects of global uncertainty uncertainty on the measured inner-scaled velocity mean and variance, for $Re_\tau = 6.5 \times 10^3$.

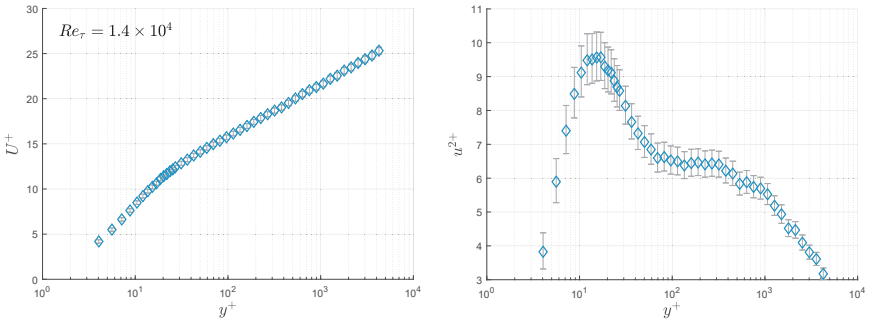

Figure A.11: Effects of global uncertainty uncertainty on the measured inner-scaled velocity mean and variance, for $Re_\tau = 1.4 \times 10^3$.

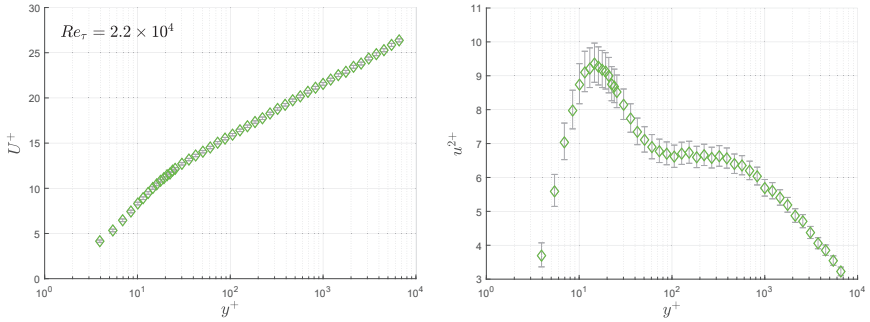

Figure A.12: Effects of global uncertainty uncertainty on the measured inner-scaled velocity mean and variance, for $Re_\tau = 2.2 \times 10^3$.

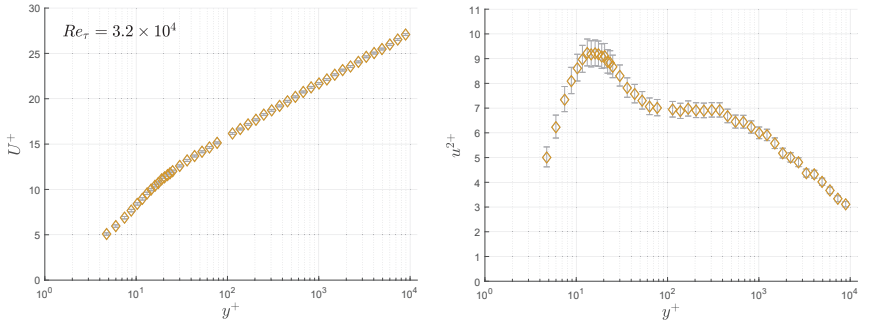

Figure A.13: Effects of global uncertainty uncertainty on the measured inner-scaled velocity mean and variance, for $Re_\tau = 3.1 \times 10^3$.

A.4.1. *Conclusions*

The analysis performed was aimed at giving an estimate of the uncertainty on the measured statistics of the first and second order. Results considering all forms of uncertainty show how for the lowest Re_τ case of present measurements there is a sizeable uncertainty on the inner-normalized mean velocity profile, dominated by uncertainty on u_τ. As Reynolds number is increased (and so does the pressure drop inside the pipe), the uncertainty on U^+ quickly becomes negligible. On the the other hand, for the normalized variance profile, a degree of uncertainty is always present around the peak location, and is mainly related to statistical convergence.

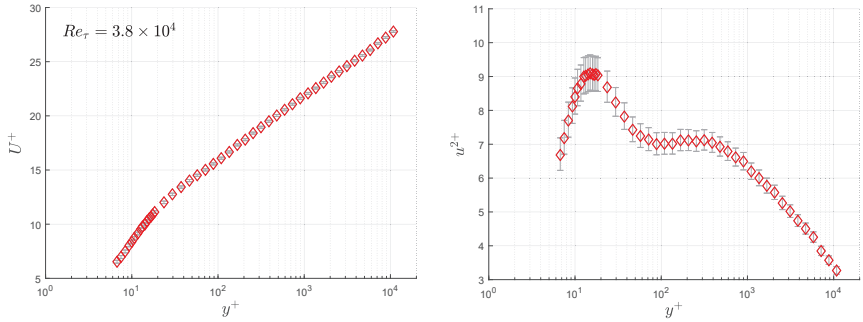

Figure A.14: Effects of global uncertainty uncertainty on the measured inner-scaled velocity mean and variance, for $Re_\tau = 3.8 \times 10^3$.

Acknowledgements

The work presented here would have not been possible without the help and support of many people, and I should apologize in advance in case I forget to mention some of them.

First of all I would like to acknowledge my supervisor Alessandro Talamelli; without him none of this would have been possible. It is mainly thanks to his dedication and hard work that the CICLoPE Laboratory has been established, and I will always be thankful for giving me the opportunity to carry out my Ph.D. in such a unique place, as well as for all his valuable advices and teachings during this time.

Thanks to Gabriele Bellani, for being first of all a good friend and for the scientific support and discussions that stimulated me during these three years; for always being open and proposing new ideas. Thanks also to Alessandro Rossetti and Andrea Cimarelli for their advices and help.

I'd like to acknowledge Antonio Segalini, Ramis Örlü, and Henrik Alfredsson from KTH, whom I collaborated with and carried out a part of the experimental work presented in this thesis. Their feedback has always been extremely helpful.

Thanks to the technical staff at the University workshop: Paolo Proli, Ivano Amadori and Mauro Ricci, for helping me through the manufacturing and troubleshooting of many pieces of the experimental set-up used. A particular thanks goes to Paolo for his friendship and for always coming up with a solution to whatever problem I was encountering.

Lastly but probably most importantly I would like to thank my friends, family and loved ones for supporting me through this time. Their encouragement and patience has been determining in helping me through the harsh times. A special thanks goes to Amina, her unconditional support and love was vital for me in these last three years.

References

Adrian, Ronald J 2007 Hairpin vortex organization in wall turbulence a. *Physics of Fluids* **19** (4), 041301.

Ahn, J., Lee, J.H., Jang, S.J. & Sung, H.J. 2013 Direct numerical simulations of fully developed turbulent pipe flows for $re_\tau = 180, 544$ and 934. *International Journal of Heat and Fluid Flow* **44**, 222–228, cited By 7.

Ahn, Junsun, Lee, Jae Hwa, Lee, Jin, Kang, Ji-hoon & Sung, Hyung Jin 2015 Direct numerical simulation of a 30r long turbulent pipe flow at $re_\tau = 3008$. *Physics of Fluids* **27** (6), 065110.

Alfredsson, P.H., Örlü, R. & Segalini, A. 2012 A new formulation for the streamwise turbulence intensity distribution in wall-bounded turbulent flows. *European Journal of Mechanics, B/Fluids* **36**, 167–175.

Alfredsson, P.H., Segalini, A. & Örlü, R. 2011 A new scaling for the streamwise turbulence intensity in wall-bounded turbulent flows and what it tells us about the "outer" peak. *Phys. Fluids* **23** (4).

Bailey, S.C.C., Kunkel, G.J., Hultmark, M., Vallikivi, M., Hill, J.P., Meyer, K.A., Tsay, C., Arnold, C.B. & Smits, A.J. 2010 Turbulence measurements using a nanoscale thermal anemometry probe. *Journal of Fluid Mechanics* **663**, 160–179.

Bailey, S.C.C., Vallikivi, M., Hultmark, M. & Smits, A.J. 2014 Estimating the value of von kármán's constant in turbulent pipe flow. *Journal of Fluid Mechanics* **749**, 79–98.

Bailey, Sean CC, Hultmark, Marcus, Schumacher, Joerg, Yakhot, Victor & Smits, Alexander J 2009 Measurement of local dissipation scales in turbulent pipe flow. *Physical review letters* **103** (1), 014502.

Barenblatt, GI 1993 Scaling laws for fully developed turbulent shear flows. part 1. basic hypotheses and analysis. *Journal of Fluid Mechanics* **248**, 513–520.

Barenblatt, GI, Chorin, AJ & Prostokishin, VM 1997 Scaling laws for fully developed turbulent flow in pipes. *Applied Mechanics Reviews* **50** (7), 413–429.

Bruun, Hans H 1995 *Hot-wire anemometry - principles and signal analysis*. Oxford science publications.

Buschmann, Matthias H & Gad-el Hak, Mohamed 2010 Normal and cross-flow reynolds stresses: differences between confined and semi-confined flows. *Experiments in Fluids* **49** (1), 213–223.

Carlier, Johan & Stanislas, Michel 2005 Experimental study of eddy structures in a turbulent boundary layer using particle image velocimetry. *Journal of Fluid Mechanics* **535** (36), 143–188.

Chauhan, K.A., Monkewitz, P.A. & Nagib, H.M. 2009 Criteria for assessing experiments in zero pressure gradient boundary layers. *Fluid Dynamics Research* **41** (2).

Chauhan, K.A., Nagib, H.M. & Monkewitz, P.A. 2007 On the composite logarithmic profile in zero pressure gradient turbulent boundary layers. In *Proceedings of 45th AIAA Aerospace Sciences Meeting*, , vol. 9, pp. 6432–6449.

Corino, Edward Robert & Brodkey, Robert S 1969 A visual investigation of the wall region in turbulent flow. *Journal of Fluid Mechanics* **37** (01), 1–30.

De Graaff, David B & Eaton, John K 2000 Reynolds-number scaling of the flat-plate turbulent boundary layer. *Journal of Fluid Mechanics* **422**, 319–346.

Del Álamo, Juan C & Jiménez, Javier 2009 Estimation of turbulent convection velocities and corrections to taylor's approximation. *Journal of Fluid Mechanics* **640**, 5–26.

Doherty, J, Ngan, P, Monty, J & Chong, M 2007 The development of turbulent pipe flow. In *16th Australasian Fluid Mechanics Conference (AFMC)*, pp. 266–270. School of Engineering, The University of Queensland.

Furuichi, N., Terao, Y., Wada, Y. & Tsuji, Y. 2015 Friction factor and mean velocity profile for pipe flow at high reynolds numbers. *Phys. Fluids* **27** (9).

Ganapathisubramani, B, Hutchins, N, Hambleton, WT, Longmire, EK & Marusic, I 2005 Investigation of large-scale coherence in a turbulent boundary layer using two-point correlations. *Journal of Fluid Mechanics* **524**, 57–80.

Ganapathisubramani, Bharathram, Longmire, Ellen K & Marusic, Ivan 2003 Characteristics of vortex packets in turbulent boundary layers. *Journal of Fluid Mechanics* **478**, 35–46.

George, William K & Castillo, Luciano 1997 Zero-pressure-gradient turbulent boundary layer. *Applied Mechanics Reviews* **50** (12), 689–729.

Guala, M, Hommema, SE & Adrian, RJ 2006 Large-scale and very-large-scale motions in turbulent pipe flow. *Journal of Fluid Mechanics* **554**, 521–542.

Head, MR & Bandyopadhyay, P 1981 New aspects of turbulent boundary-layer structure. *Journal of Fluid Mechanics* **107**, 297–338.

Hultmark, M., Bailey, S.C.C. & Smits, A.J. 2010 Scaling of near-wall turbulence in pipe flow. *J. Fluid Mech.* **649**, 103–113.

Hultmark, M., Vallikivi, M., Bailey, S.C.C. & Smits, A.J. 2012 Turbulent pipe flow at extreme reynolds numbers. *Phys. Rev. Lett.* **108** (9).

Hultmark, Marcus, Vallikivi, M, Bailey, SCC & Smits, AJ 2013 Logarithmic scaling of turbulence in smooth-and rough-wall pipe flow. *Journal of Fluid Mechanics* **728**, 376–395.

Hutchins, N & Marusic, Ivan 2007 Evidence of very long meandering features in

the logarithmic region of turbulent boundary layers. *Journal of Fluid Mechanics* **579**, 1–28.

Hutchins, N., Nickels, T.B., Marusic, I. & Chong, M.S. 2009 Hot-wire spatial resolution issues in wall-bounded turbulence. *Journal of Fluid Mechanics* **635**, 103–136.

Jimenez, Juan M, Hultmark, M & Smits, AJ 2010 The intermediate wake of a body of revolution at high reynolds numbers. *Journal of Fluid Mechanics* **659**, 516–539.

Johansson, Arne V & Alfredsson, P Henrik 1983 Effects of imperfect spatial resolution on measurements of wall-bounded turbulent shear flows. *Journal of Fluid Mechanics* **137**, 409–421.

von Kármán, T 1930 Mechanische aehnlichkeit und turbulenz. In *Third international congress on applied mechanics, Stockholm, Sweden*, pp. 85–93.

Kim, J. 2012 Progress in pipe and channel flow turbulence, 1961-2011. *J. Turbul.* **13**, 1–19.

Kim, KC & Adrian, RJ 1999 Very large-scale motion in the outer layer. *Physics of Fluids* **11** (2), 417–422.

King, Louis Vessot 1914 On the convection of heat from small cylinders in a stream of fluid: determination of the convection constants of small platinum wires with applications to hot-wire anemometry. *Philosophical Transactions of the Royal Society of London. Series A, Containing Papers of a Mathematical or Physical Character* **214**, 373–432.

Klewicki, JC 2013 Self-similar mean dynamics in turbulent wall flows. *Journal of Fluid Mechanics* **718**, 596–621.

Kline, SJ, Reynolds, WC, Schraub, FA & Runstadler, PW 1967 The structure of turbulent boundary layers. *Journal of Fluid Mechanics* **30** (04), 741–773.

Kolmogorov, Andrey Nikolaevich 1941 The local structure of turbulence in incompressible viscous fluid for very large reynolds numbers [in russian]. In *Dokl. Akad. Nauk SSSR*, , vol. 30, pp. 299–303.

König, F., Zanoun, E.-S., Öngüner, E. & Egbers, C. 2014 The colapipe - the new cottbus large pipe test facility at brandenburg university of technology cottbus-senftenberg. *Rev. Sci. Instrum.* **85** (7).

Kunkel, Gary J & Marusic, Ivan 2006 Study of the near-wall-turbulent region of the high-reynolds-number boundary layer using an atmospheric flow. *Journal of Fluid Mechanics* **548**, 375–402.

Ligrani, P.M. & Bradshaw, P. 1987 Spatial resolution and measurement of turbulence in the viscous sublayer using subminiature hot-wire probes. *Experiments in Fluids* **5** (6), 407–417.

Lu, SS & Willmarth, WW 1973 Measurements of the structure of the reynolds stress in a turbulent boundary layer. *Journal of Fluid Mechanics* **60** (03), 481–511.

Marusic, Ivan 2001 On the role of large-scale structures in wall turbulence. *Physics of Fluids* **13** (3), 735–743.

Marusic, Ivan, Mathis, Romain & Hutchins, Nicholas 2010*a* High reynolds number effects in wall turbulence. *International Journal of Heat and Fluid Flow* **31** (3), 418–428.

Marusic, I., McKeon, B.J., Monkewitz, P.A., Nagib, H.M., Smits, A.J. & Sreenivasan, K.R. 2010*b* Wall-bounded turbulent flows at high reynolds numbers: Recent advances and key issues. *Physics of Fluids* **22** (6), 1–24.

Marusic, Ivan, Monty, Jason P, Hultmark, Marcus & Smits, Alexander J 2013 On the logarithmic region in wall turbulence. *Journal of Fluid Mechanics* **716**, R3.

Mathis, Romain, Hutchins, Nicholas & Marusic, Ivan 2009 Large-scale amplitude modulation of the small-scale structures in turbulent boundary layers. *Journal of Fluid Mechanics* **628**, 311–337.

McKeon, B.J., Zagarola, M.V. & Smits, A.J. 2005 A new friction factor relationship for fully developed pipe flow. *Physics of Fluids* **538**, 429–443.

Mckeon, Beverley J, Li, J, Jiang, W, Morrison, Jonathan F & Smits, Alexander J 2004 Further observations on the mean velocity distribution in fully developed pipe flow. *Journal of Fluid Mechanics* **501**, 135–147.

Meneveau, Charles & Marusic, Ivan 2013 Generalized logarithmic law for high-order moments in turbulent boundary layers. *Journal of Fluid Mechanics* **719**, R1.

Metzger, MM & Klewicki, JC 2001 A comparative study of near-wall turbulence in high and low reynolds number boundary layers. *Physics of Fluids (1994-present)* **13** (3), 692–701.

Metzger, M, McKeon, BJ & Holmes, H 2007 The near-neutral atmospheric surface layer: turbulence and non-stationarity. *Philosophical Transactions of the Royal Society of London A* **365** (1852), 859–876.

Millikan, Clark B 1938 A critical discussion of turbulent flows in channels and circular tubes. In *Proc. 5th Int. Cong. Appl. Mech*, pp. 386–392. Wiley/Chapman and Hall, New York-London.

Mochizuki, S & Nieuwstadt, FTM 1996 Reynolds-number-dependence of the maximum in the streamwise velocity fluctuations in wall turbulence. *Experiments in Fluids* **21** (3), 218–226.

Monkewitz, PA, Duncan, RD & Nagib, HM 2010 Correcting hot-wire measurements of stream-wise turbulence intensity in boundary layers. *Physics of Fluids* **22** (9), 091701.

Monkewitz, Peter A & Nagib, Hassan M 2015 Large-reynolds-number asymptotics of the streamwise normal stress in zero-pressure-gradient turbulent boundary layers. *Journal of Fluid Mechanics* **783**, 474–503.

Monty, JP, Hutchins, N, Ng, HCH, Marusic, I & Chong, MS 2009 A comparison of turbulent pipe, channel and boundary layer flows. *Journal of Fluid Mechanics* **632**, 431–442.

Monty, JP, Stewart, JA, Williams, RC & Chong, MS 2007 Large-scale features in turbulent pipe and channel flows. *Journal of Fluid Mechanics* **589**, 147–156.

Monty, Jason Patrick 2005 *Developments in smooth wall turbulent duct flows*. University of Melbourne, Department of Mechanical and Manufacturing Engineering.

Morrill-Winter, C, Klewicki, J, Baidya, R & Marusic, I 2015 Temporally optimized spanwise vorticity sensor measurements in turbulent boundary layers. *Experiments in Fluids* **56** (12), 216.

Morrison, J.F., McKeon, B.J., Jiang, W. & Smits, A.J. 2004 Scaling of the streamwise velocity component in turbulent pipe flow. *J. Fluid Mech.* **508** (508), 99–131.

Nagib, H.M. & Chauhan, K.A. 2008 Variations of von krmn coefficient in canonical flows. *Physics of Fluids* **20** (10).

Nagib, Hassan M, Chauhan, Kapil A & Monkewitz, Peter A 2007 Approach to an asymptotic state for zero pressure gradient turbulent boundary layers. *Philosophical Transactions of the Royal Society of London A: Mathematical, Physical and Engineering Sciences* **365** (1852), 755–770.

Nagib, Hassan M, Christophorou, Chris & Monkewitz, Peter A 2006 High reynolds number turbulent boundary layers subjected to various pressure-gradient conditions. In *IUTAM symposium on one hundred Years of boundary layer research*, pp. 383–394. Springer.

Ng, HCH, Monty, JP, Hutchins, N, Chong, MS & Marusic, I 2011 Comparison of turbulent channel and pipe flows with varying reynolds number. *Experiments in fluids* **51** (5), 1261–1281.

Nickels, TB, Marusic, I, Hafez, S & Chong, MS 2005 Evidence of the k 1- 1 law in a high-reynolds-number turbulent boundary layer. *Physical review letters* **95** (7), 074501.

Nickels, TB, Marusic, I, Hafez, S, Hutchins, N & Chong, MS 2007 Some predictions of the attached eddy model for a high reynolds number boundary layer. *Philosophical Transactions of the Royal Society of London A: Mathematical, Physical and Engineering Sciences* **365** (1852), 807–822.

Nikuradse, Johann 1933 Laws of flow in rough pipes. In *VDI Forschungsheft*. Citeseer.

Örlü, R. & Alfredsson, P.H. 2013 Comment on the scaling of the near-wall streamwise variance peak in turbulent pipe flows. *Experiments in Fluids* **54** (1).

Örlü, R, Fiorini, T, Segalini, A, Bellani, G, Talamelli, A & Alfredsson, PH 2017 Reynolds stress scaling in pipe flow turbulencefirst results from ciclope. *Phil. Trans. R. Soc. A* **375** (2089), 20160187.

Örlü, Ramis, Fransson, Jens HM & Alfredsson, P Henrik 2010 On near wall measurements of wall bounded flows - the necessity of an accurate determination of the wall position. *Progress in Aerospace Sciences* **46** (8), 353–387.

Österlund, Jens M, Johansson, Arne V, Nagib, Hassan M & Hites, Michael H 2000 A note on the overlap region in turbulent boundary layers. *Physics of Fluids (1994-present)* **12** (1), 1–4.

Panton, Ronald Lee 1997 *Self-sustaining mechanisms of wall turbulence*, , vol. 15. Computational Mechanics.

Perry, AE & Abell, CJ 1977 Asymptotic similarity of turbulence structures in smooth-and rough-walled pipes. *Journal of Fluid Mechanics* **79** (04), 785–799.

Perry, AE & Chong, MS 1982 On the mechanism of wall turbulence. *Journal of Fluid Mechanics* **119**, 173–217.

Perry, AE, Henbest, S & Chong, MS 1986 A theoretical and experimental study of wall turbulence. *Journal of Fluid Mechanics* **165**, 163–199.

Pope, Stephen B 2001 Turbulent flows.

Prandtl, Ludwig 1926 Application of the" magnus effect" to the wind propulsion of ships .

Pullin, DI, Inoue, M & Saito, N 2013 On the asymptotic state of high reynolds number, smooth-wall turbulent flows. *Physics of Fluids* **25** (1), 015116.

Reynolds, Osborne 1883 An experimental investigation of the circumstances which determine whether the motion of water shall be direct or sinuous, and of the law of resistance in parallel channels. *Proceedings of the royal society of London* **35** (224-226), 84–99.

Richardson, LEWIS F 1922 Weather prediction by numerical process cambridge university press. *CambridgeRichardsonWeather prediction by numerical process1922* .

Romano, G P 1995 Analysis of two-point velocity measurements in near-wall flows. *Experiments in Fluids* **20** (2), 68–83.

Ruedi, JD, Nagib, H, Österlund, J & Monkewitz, PA 2003 Evaluation of three techniques for wall-shear measurements in three-dimensional flows. *Experiments in Fluids* **35** (5), 389–396.

Schlatter, Philipp, Örlü, Ramis, Li, Qiang, Brethouwer, Geert, Fransson, Jens HM, Johansson, Arne V, Alfredsson, P Henrik & Henningson, Dan S 2009 Turbulent boundary layers up to re θ= 2500 studied through simulation and experiment. *Physics of fluids* **21** (5), 051702.

Segalini, A., Örlü, R., Schlatter, P., Alfredsson, P.H., Redi, J.-D. & Talamelli, A. 2011 A method to estimate turbulence intensity and transverse taylor microscale in turbulent flows from spatially averaged hot-wire data. *Experiments in Fluids* **51** (3), 693–700.

Smits, A.J., McKeon, B.J. & Marusic, I. 2011*a* High-reynolds number wall turbulence. *Annu. Rev. Fluid Mech.* **43**, 353–375, cited By 171.

Smits, A.J., Monty, J., Hultmark, M., Bailey, S.C.C., Hutchins, N. & Marusic, I. 2011*b* Spatial resolution correction for wall-bounded turbulence measurements. *J. Fluid Mech.* **676**, 41–53.

Talamelli, A., Persiani, F., Fransson, J.H.M., Alfredsson, P.H., Johansson, A.V., M Nagib, H., Rüedi, J.-D., Sreenivasan, K.R. & Monkewitz, P.A. 2009 Ciclope - a response to the need for high reynolds number experiments. *Fluid Dynamics Research* **41** (2).

Taylor, Geoffrey Ingram 1938 The spectrum of turbulence. In *Proceedings of the Royal Society of London A: Mathematical, Physical and Engineering Sciences*, , vol. 164, pp. 476–490. The Royal Society.

Tomkins, Christopher D & Adrian, Ronald J 2003 Spanwise structure and scale growth in turbulent boundary layers. *Journal of Fluid Mechanics* **490**, 37–74.

Townsend, Albert A 1976 *The structure of turbulent shear flow*. Cambridge university press.

Tropea, Cameron, Yarin, Alexander L & Foss, John F 2007 *Springer handbook of experimental fluid mechanics*, , vol. 1. Springer Science & Business Media.

Vallikivi, M., Ganapathisubramani, B. & Smits, A.J. 2015*a* Spectral scaling in boundary layers and pipes at very high reynolds numbers. *Journal of Fluid Mechanics* **771**, 303–326.

Vallikivi, M., Hultmark, M., Bailey, S.C.C. & Smits, A.J. 2011 Turbulence measurements in pipe flow using a nano-scale thermal anemometry probe. *Exp. Fluids* **51** (6), 1521–1527.

Vallikivi, M., Hultmark, M. & Smits, A.J. 2015*b* Turbulent boundary layer statistics at very high reynolds number. *Journal of Fluid Mechanics* **779**, 371–389.

Vincenti, P, Klewicki, J, Morrill-Winter, C, White, CM & Wosnik, M 2013 Streamwise velocity statistics in turbulent boundary layers that spatially develop to high reynolds number. *Experiments in fluids* **54** (12), 1629.

Wallace, James M 2016 Quadrant analysis in turbulence research: history and evolution. *Annual Review of Fluid Mechanics* **48**, 131–158.

Wallace, James M, Eckelmann, Helmut & Brodkey, Robert S 1972 The wall region in turbulent shear flow. *Journal of Fluid Mechanics* **54** (01), 39–48.

Wei, T, Fife, P, Klewicki, J & McMurtry, P 2005 Properties of the mean momentum balance in turbulent boundary layer, pipe and channel flows. *Journal of Fluid Mechanics* **522**, 303–327.

Welch, Peter 1967 The use of fast fourier transform for the estimation of power spectra: a method based on time averaging over short, modified periodograms. *IEEE Transactions on audio and electroacoustics* **15** (2), 70–73.

Willmarth, WW & Lu, SS 1972 Structure of the reynolds stress near the wall. *Journal of Fluid Mechanics* **55** (01), 65–92.

Wosnik, Martin, Castillo, Luciano & George, William K 2000 A theory for turbulent pipe and channel flows. *Journal of Fluid Mechanics* **421**, 115–145.

Wu, Xiaohua & Moin, Parviz 2009 Direct numerical simulation of turbulence in a nominally zero-pressure-gradient flat-plate boundary layer. *Journal of Fluid Mechanics* **630**, 5–41.

Wyngaard, JC 1968 Measurement of small-scale turbulence structure with hot wires. *Journal of Physics E: Scientific Instruments* **1** (11), 1105.

Yavuzkurt, Savas 1984 A guide to uncertainty analysis of hot-wire data. *ASME, Transactions, Journal of Fluids Engineering* **106**, 181–186.

Zagarola, MV, Perry, AE & Smits, AJ 1997 Log laws or power laws: The scaling in the overlap region. *Physics of Fluids (1994-present)* **9** (7), 2094–2100.

Zagarola, Mark V & Smits, Alexander J 1998 Mean-flow scaling of turbulent pipe flow. *Journal of Fluid Mechanics* **373**, 33–79.

Zhao, Rongrong & Smits, Alexander J 2007 Scaling of the wall-normal turbulence component in high-reynolds-number pipe flow. *Journal of Fluid Mechanics* **576**, 457–473.

Zhou, Ang & Klewicki, Joe 2015 Properties of the streamwise velocity fluctuations in the inertial layer of turbulent boundary layers and their connection to self-similar mean dynamics. *International Journal of Heat and Fluid Flow* **51**, 372–382.

Zimmer, Franziska, Zanoun, E-S & Egbers, Christoph 2011 A study on the influence of triggering pipe flow regarding mean and higher order statistics. In *Journal of Physics: Conference Series*, , vol. 318, p. 032039. IOP Publishing.